

AD-A064 976

GEORGIA TECH RESEARCH INST ATLANTA
EFFECTS OF VARIOUS EXHAUST PLUME MODELS ON MISSILE SKIN CURRENT--ETC(U)
JAN 79 T K WU, D R WILTON, L L TSAI

F/G 20/3

F30602-75-C-0118

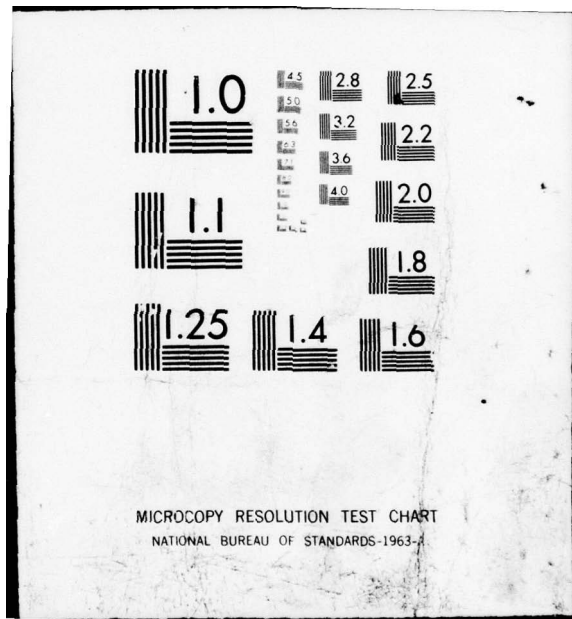
RADC-TR-78-261

NL

UNCLASSIFIED

1 OF 2
AD A064 976





ADA 064976

12
44
LEVEL II



RADC-TR-78-261

Phase Report

January 1979

EFFECTS OF VARIOUS EXHAUST PLUME MODELS ON MISSILE SKIN CURRENTS

University of Mississippi

T. K. Wu
D. R. Wilton
L. L. Tsai

DDC FILE COPY:

APPROVED FOR PUBLIC RELEASE; DISTRIBUTION UNLIMITED

ROME AIR DEVELOPMENT CENTER
Air Force Systems Command
Griffiss Air Force Base, New York 13441

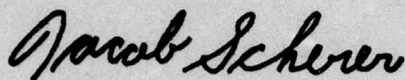
DDC
REF ID: A
FEB 27 1979
A

79 02 23 056

This report has been reviewed by the RADC Information Office (OI) and is releasable to the National Technical Information Service (NTIS). At NTIS it will be releasable to the general public, including foreign nations.

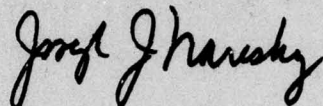
RADC-TR-78-261 has been reviewed and is approved for publication.

APPROVED:



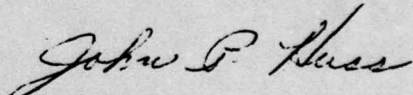
JACOB SCHERER
Project Engineer

APPROVED:



JOSEPH J. NARESKY
Chief, Reliability & Compatibility Division

FOR THE COMMANDER:



JOHN P. HUSS
Acting Chief, Plans Office

If your address has changed or if you wish to be removed from the RADC mailing list, or if the addressee is no longer employed by your organization, please notify RADC (RBC) Griffiss AFB NY 13441. This will assist us in maintaining a current mailing list.

Do not return this copy. Retain or destroy.

MISSION
of
Rome Air Development Center

RADC plans and conducts research, exploratory and advanced development programs in command, control, and communications (C³) activities, and in the C³ areas of information sciences and intelligence. The principal technical mission areas are communications, electromagnetic guidance and control, surveillance of ground and aerospace objects, intelligence data collection and handling, information system technology, ionospheric propagation, solid state sciences, microwave physics and electronic reliability, maintainability and compatibility.



UNCLASSIFIED

SECURITY CLASSIFICATION OF THIS PAGE (When Data Entered)

19 REPORT DOCUMENTATION PAGE		READ INSTRUCTIONS BEFORE COMPLETING FORM
1. REPORT NUMBER RADC-TR-78-261	2. GOVT ACCESSION NO.	3. RECIPIENT'S CATALOG NUMBER
4. TITLE (and Subtitle) EFFECTS OF VARIOUS EXHAUST PLUME MODELS ON MISSILE SKIN CURRENTS		5. TYPE OF REPORT & PERIOD COVERED Phase Report
6. AUTHOR(s) T. K. Wu D. R. Wilton L. L. Tsai		7. PERFORMING ORG. REPORT NUMBER N/A
8. CONTRACT OR GRANT NUMBER(s) F30602-75-C-0118		9. PROGRAM ELEMENT, PROJECT, TASK AREA & WORK UNIT NUMBERS 206403P3 (17) 03
10. CONTROLLING OFFICE NAME AND ADDRESS Rome Air Development Center (RBC) Griffiss AFB NY 13441		11. REPORT DATE January 1979
12. MONITORING AGENCY NAME & ADDRESS (if different from Controlling Office) Same		13. NUMBER OF PAGES 106
14. DISTRIBUTION STATEMENT (of this Report) Approved for public release; distribution unlimited.		15. SECURITY CLASS. (of this report) UNCLASSIFIED
16. DISTRIBUTION STATEMENT (of the abstract entered in Block 20, if different from Report) Same		15a. DECLASSIFICATION/DOWNGRADING SCHEDULE N/A
17. SUPPLEMENTARY NOTES RADC Project Engineer: Jacob Scherer (RBC)		
18. KEY WORDS (Continue on reverse side if necessary and identify by block number) Electromagnetic theory Antennas Mathematical modeling		
19. ABSTRACT (Continue on reverse side if necessary and identify by block number) The effects on the missile skin current due to the presence of an exhaust plume are studied via analyzing thin-wire and body-of-revolution models of the missile/plume configuration. In the wire model, the simple and efficient thin wire theory and numerical methods are used to estimate order of magnitude effects by treating the missile as a thin cylinder and the plume as an attached lossy cylinder. Several body-of-revolution models are also described, compared and used to analyze large radius plumes modeled both as homogeneous and inhomogeneous.		

DD FORM 1 JAN 73 1473 EDITION OF 1 NOV 65 IS OBSOLETE

UNCLASSIFIED
SECURITY CLASSIFICATION OF THIS PAGE (When Data Entered)

388 700

Gra

UNCLASSIFIED

SECURITY CLASSIFICATION OF THIS PAGE(When Data Entered)

geneous bodies-of-revolution. Extensive results are presented for all models to permit one to compare the differences in currents induced on the missile with and without the plume as functions of frequency, incidence angle of the plane wave source, plume conductivity, and plume shape.

ACCESSION for	
NTIS	White Section
DDC	DDF Section <input checked="" type="checkbox"/>
UNARMED	<input type="checkbox"/>
JUS	<input type="checkbox"/>
BY	
DISTRIBUTION/AVAILABILITY CODES	
Dist.	REG / OR SPECIAL
A	

UNCLASSIFIED

SECURITY CLASSIFICATION OF THIS PAGE(When Data Entered)

PREFACE

This effort was conducted by the University of Mississippi under the sponsorship of the Rome Air Development Center Post-Doctoral Program for Rome Air Development Center. Mr. Jack Edwards RADC/RBCA was the task project engineer and provided overall technical direction and guidance.

The RADC Post-Doctoral Program is a cooperative venture between RADC and some sixty-five universities eligible to participate in the program. Syracuse University (Department of Electrical Engineering), Purdue University (School of Electrical Engineering), Georgia Institute of Technology (School of Electrical Engineering), and State University of New York at Buffalo (Department of Electrical Engineering) act as prime contractor schools with other schools participating via sub-contracts with the prime schools. The U.S. Air Force Academy (Department of Electrical Engineering), Air Force Institute of Technology (Department of Electrical Engineering), and the Naval Post-Graduate School (Department of Electrical Engineering) also participate in the program.

The Post-Doctoral Program provides an opportunity for faculty at participating universities to spend up to one year full time on exploratory development and problem-solving efforts with the post-doctorals splitting their time between the customer location and their educational institutions. The program is totally customer-funded with current projects being undertaken for Rome Air Development Center (RADC), Space and Missile Systems Organization (SAMSO), Aeronautical System Division (ASD), Electronics Systems Division (ESD), Air Force Avionics Laboratory (AFAL),

Foreign Technology Division (FTD), Air Force Weapons Laboratory (AFWL),
Armament Development and Test Center (ADTC), Air Force Communications
Service (AFCS), Aerospace Defense Command (ADC), HQ USAF, Defense Commu-
niques Service (AFCS), Aerospace Defense Command (ADC), HQ USAF, Defense
Communications Agency (DCA), Navy, Army, Aerospace Medical Division (AMD),
and Federal Aviation Administration (FAA).

Further information about the RADC Post-Doctoral Program can be
obtained from Mr. Jacob Scherer, RADC/RBC, Griffiss AFB, NY, 13441,
telephone Autovon 587-2543, Commercial (315) 330-2543.

TABLE OF CONTENTS

1. INTRODUCTION	1
2. THIN WIRE MODEL	4
2.1 Theory	4
2.2 Numerical Results	8
3. BODY OF REVOLUTION MODEL	60
3.1 Surface Integral Equation (SIE) Method.	61
3.2 Approximate Integral Equation (AIE) Method	66
3.3 Numerical Results	68
4. CONCLUSIONS	102
ACKNOWLEDGMENT	104
REFERENCES	105

LIST OF FIGURES

Figure #	Caption	Page
1.	Thin wire modeling of a missile with plume.	5
2.	Current magnitude on 10' missile (radius $a = 2.5"$) with and without presence of 8" crossed-wire simulating fins illuminated by a broadside incident plane wave ($f = 100$ MHz)	6
3.	Comparison between wire code and Taylor's solution for the current on a missile with plume ($h = l = 1.11\lambda$, $a = 0.02\lambda$, $\sigma = 0.1$ mho/m) illuminated by a broadside incident plane wave ($f = 19.6$ MHz).	9
4.	Contour plot of current magnitude as functions of the length along the missile-plume axis and the plume conductivity σ (Broadside incidence, $f = 20$ MHz).	11
5.	Contour plot of $ I $, $\theta_i = 90^\circ$, $f = 35$ MHz.	12

Captions for Figures 6-42 are same as for Figure 5 with the following change in θ and frequency.

	θ°	Freq. (MHz)	
6.	90	50	13
7.	90	60	14
8.	90	70	15
9.	90	80	16
10.	90	90	17
11.	90	100	18
12.	90	120	19
13.	120	20	20
14.	120	50	21
15.	120	100	22
16.	150	35	23
17.	150	50	24
18.	150	100	25

LIST OF FIGURES (cont.)

Figure #	Caption	Page	
Captions for Figures 6-42 are same as for Figure 5 with the following change in θ and frequency.			
	$\theta(^{\circ})$	Freq. (MHz)	
19.	150	120	26
20.	165	20	27
21.	165	35	28
22.	165	50	29
23.	165	100	30
24.	165	120	31
25.	60	20	32
26.	60	35	33
27	60	50	34
28.	60	80	35
29.	60	100	36
30.	60	120	37
31.	30	20	38
32.	30	35	39
33.	30	50	40
34.	30	80	41
35.	30	100	42
36.	30	120	43
37.	15	20	44
38.	15	35	45
39.	15	50	46

LIST OF FIGURES (cont.)

Figure #	Caption	Page	
Captions for Figures 6-42 are same as for Figure 5 with the following change in θ and frequency.			
	$\theta(^{\circ})$	Freq. (MHz)	
40	15	80	47
41	15	100	48
42	15	120	49
43.	Current magnitude $ I $ at middle on a missile ($h = 10'$, $a = 2.5''$) with and without plume ($\ell = 20'$, $\sigma = 0.01, 0.2$, and 1 V/m) as a function of incident angle θ_i ($f = 50$ MHz).	50	
44.	$ I $ at middle on the missile ($f = 100$ MHz).	51	
45.	$ I $ at middle on the missile ($f = 120$ MHz).	52	
46.	$ I $ at $3'$ from nose of the missile ($f = 50$ MHz).	54	
47.	$ I $ at $3'$ from nose of the missile ($f = 100$ MHz).	55	
48.	$ I $ at $3'$ from nose of the missile ($f = 120$ MHz).	56	
49.	Inhomogeneous plume conductivity profile along the plume axis.	57	
50.	Current amplitude $ I $ on a missile ($h = 10'$, $a = 2.5''$) with and without the inhomogeneous plume of Fig. 49 (broadside incidence, $f = 100$ MHz).	58	
51.	$ I $ on a missile with and without the inhomogeneous plume of Fig. 49 ($\theta_i = 165^{\circ}$, $f = 100$ MHz).	59	
52.	Composite body of revolution models of missile with homogeneous plume.	62	
53.	Current magnitude on a homogeneous dielectric cylinder ($\epsilon_r = 50$, $\sigma = 20.37 \text{ V/m}$, $h = 0.737\lambda$, $a = 0.025\lambda$, $f = 9.45$ GHz).	69	
54.	Current magnitude on missile (length $h = 10'$, radius $a = 2.5''$) with and without homogeneous plume (length $\ell = 10'$, radius $a = 2.5''$, $\sigma = 0.2 \text{ V/m}$), broadside incidence ($f = 50$ MHz).	70	

LIST OF FIGURES (cont.)

Figure #	Caption	Page
55.	Current magnitudes on the same missile as Figure 54 but for angle of incidence $\theta_i = 30^\circ$.	71
56.	Current magnitudes on missile ($h = 10'$, $a = 2.5''$) with plumes of various shapes ($b = 3a$, $\ell = 10'$ and $20'$, $\sigma = 0.2 \text{ V/m}$) broadside incidence, $f = 50 \text{ MHz}$.	72
57.	Current magnitudes on the same missile plume configurations as Figure 56 but for angle of incidence $\theta_i = 30^\circ$.	73
58.	Current magnitudes on missile ($h = \ell = 10'$, $a = 2.5''$) with homogeneous plume via the SIE and AIE approaches for (a) $\sigma = 0.1 \text{ V/m}$, (b) $\sigma = 1 \text{ V/m}$, $f = 50 \text{ MHz}$, broadside incidence.	75
59.	Current magnitude on the same missile as Figure 58 but at a frequency $f = 100 \text{ MHz}$.	76
60.	Three-dimensional view of inhomogeneous plume conductivity profiles computed for a Redeye missile at 5000 ft. altitude.	77
61.	Maximum radius profile of the inhomogeneous plume of Figure 60.	78
62.	Current magnitude on a Chaparral missile ($h=3\text{m}$, $a=6.35\text{cm}$) with homogeneous plume compared to the Redeye plume model of Figures 60 and 61, $f=100 \text{ MHz}$, broadside incidence.	79
63.	Current magnitude on the same configurations as Figure 62 but with angle of incidence $\theta_i = 30^\circ$.	80
64.	Three-dimensional view of inhomogeneous plume conductivity profiles computed for a Chaparral missile at 5000 ft. altitude.	82
65.	Maximum conductivity profile of the inhomogeneous plume of Figure 64.	83
66.	Current magnitude on a Chaparral missile ($h = 3\text{m}$, $a = 6.35 \text{ cm}$) with and without the two inhomogeneous plume models, $\theta_i = 90^\circ$, $f = 50 \text{ MHz}$.	84
67.	Current magnitude on a Chaparral missile with and without the two inhomogeneous plume models, $\theta_i = 30^\circ$, $f = 50 \text{ MHz}$.	85

LIST OF FIGURES (cont.)

Figure #	Caption	Page
68.	Current on a Chaparral missile ($h = 3$ m, $l = 7.2$ m, $a = 6.35$ cm) as a function of frequency, no plume, $\theta_i = 30^\circ$.	87
69.	Current magnitude on a Chaparral missile ($h = 3$ m, $l = 7.2$ m, $a = 6.35$ cm), as a function of frequency, long plume model, $\theta_i = 30^\circ$.	88
70.	Current on a Chaparral missile, ($h = 3$ m, $l = 6.4$ m, $a = 6.35$ cm) as a function of frequency, short plume model, $\theta_i = 30^\circ$.	89
71.	Current on a Chaparral missile as a function of frequency, no plume, $\theta_i = 60^\circ$.	90

Captions for Figures 72-82 are same as for Figure 71 with following change in plume model and angle of incidence.

	Plume Model	Angle of Incidence	
72.	long plume	60	91
73.	short plume	60	92
74.	no plume	90	93
75.	long plume	90	94
76.	short plume	90	95
77.	no plume	120	96
78.	long plume	120	97
79	short plume	120	98
80	no plume	150	99
81	long plume	150	100
82	short plume	150	101

CHAPTER I

INTRODUCTION

A manifestation of the rocket exhaust of a missile in flight is the presence of a trailing plume. And whereas the missile skin is made of conducting metal, the rocket exhaust plume consists of partially ionized gases or plasma which electrically gives the plume region a finite conductivity. When this composite conducting/partially-conducting object is immersed in an electromagnetic environment, it is necessary to estimate the skin current on the missile with plume in order to determine how on board subsystems may respond [1, 2, 3, 4]. In a laboratory situation (e.g., in an anechoic chamber), however, it is difficult to accommodate the presence of the plume because of the attendant hazards and expenses. Thus testing is often done without accounting for the plume. The problem we address in this report is to estimate what differences one might expect in subsystem response, under electromagnetic compatibility (EMC) testing, with and without a trailing plume present. The consideration of the actual internal coupling mechanism is an extremely difficult problem whose consideration would take us far afield. However, if the coupling is primarily through electrically small apertures in the missile skin, then it is known that the coupling to the interior is proportional to a linear combination of the current and charge that exist at the aperture when it is covered over by a metallic conductor. Thus, computation of this so-called "short circuit current" on the missile with and without the plume present should be sufficient to determine what differences in the coupling might be attributable to the presence of the plume. The "short-circuit charge," of course, can be found from the current using the equation

of continuity.

In the past, thin wire theory has been used to estimate the current induced on a missile with plume [1-4]. There the missile is viewed as a thin conducting wire of radius 'a' and length 'h', as shown in Fig. 1, and the plume is modeled as an attached lossy wire of the same radius as the missile. The radius a is assumed to be small compared to the wavelength λ and to the axial length of the missile and plume, thus permitting the use of thin wire theory. The conductivity σ of the plume may be constant or axially varying depending on whether a homogeneous or axially inhomogeneous model is assumed, respectively. Recent calculations using the Aero Chem low altitude plume program (LAPP) [5] indicate, however, that the plume conductivity σ is rather strongly inhomogeneous both axially and radially, and that the plume radius is considerably different from that of the missile and varies along the plume axis. In addition, these effects are also strongly influenced by the missile altitude. Therefore, more sophisticated models and methods seem to be necessary to study the current induced on the missile with and without the plume.

In this report, the thin wire model and body of revolution models are used to assess the currents induced on a missile with and without a trailing plume present. Chapter II summarizes the simple and efficient thin wire theory which is useful for estimating order of magnitude effects. Although the plume radius is fixed in this model it is capable of modeling either a homogeneous plume or an axially inhomogeneous plume. In Chapter III, several body of revolution models are described, compared, and used to analyze large radius and inhomogeneous plume models. Extensive results are given in both

chapters to permit one to compare the differences in currents induced on the missile with and without the plume as functions of frequency, incident angle of the plane wave source, plume conductivity, and plume shape. In the body of revolution models, only the circumferentially uniform Fourier component of the current has been computed. For reasonably thin missiles the non-symmetric current modes are only weakly coupled to the plume. Hence, these modes of missile current, although sometimes significant in themselves, are not expected to change much with or without the plume present.

CHAPTER II
THIN WIRE MODEL

In this chapter, a numerical determination of the induced currents on a missile with a trailing plume is made using simple wire models. In the analysis, the missile with plume is viewed as a thin conducting wire of radius $a \ll \lambda$, as shown in Fig. 1, with a resistively loaded section, thus permitting the use of thin wire theory [6,7,8]. Both homogeneous and axially inhomogeneous plumes are considered. Numerical results for the induced currents are given as a function of frequency, incidence angle of the plane wave source, and the plume conductivity. The main objective is to examine the differences in currents induced on a missile with or without the plume. The presence of canards and fins might be accounted for by introducing attached cross-wires into the model. However, a typical result for a 10' missile with 8" crossed wires is as shown in Fig. 2, where, as can be seen, other than the expected discontinuity in current at the junction, the current distribution and peak currents are not significantly changed. Thus the effects of body appendages are considered to be minor, and will not be included throughout the remainder of these studies.

2.1. Theory

Consider the thin wire model as depicted in Fig. 1. The missile (with radius "a" and length "h") is regarded as a conducting wire and the plume (with radius "a", length "l", and conductivity "σ") is regarded as an impedance (or resistively) loaded section. Assuming the current flows only in the axial or z direction, one may obtain the following integro-differential

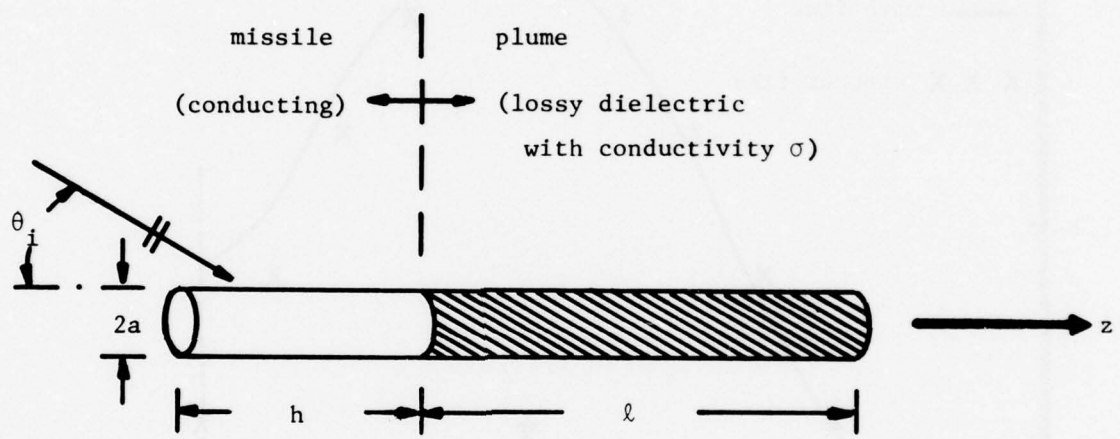


Fig. 1. Thin wire modeling of a missile with plume.

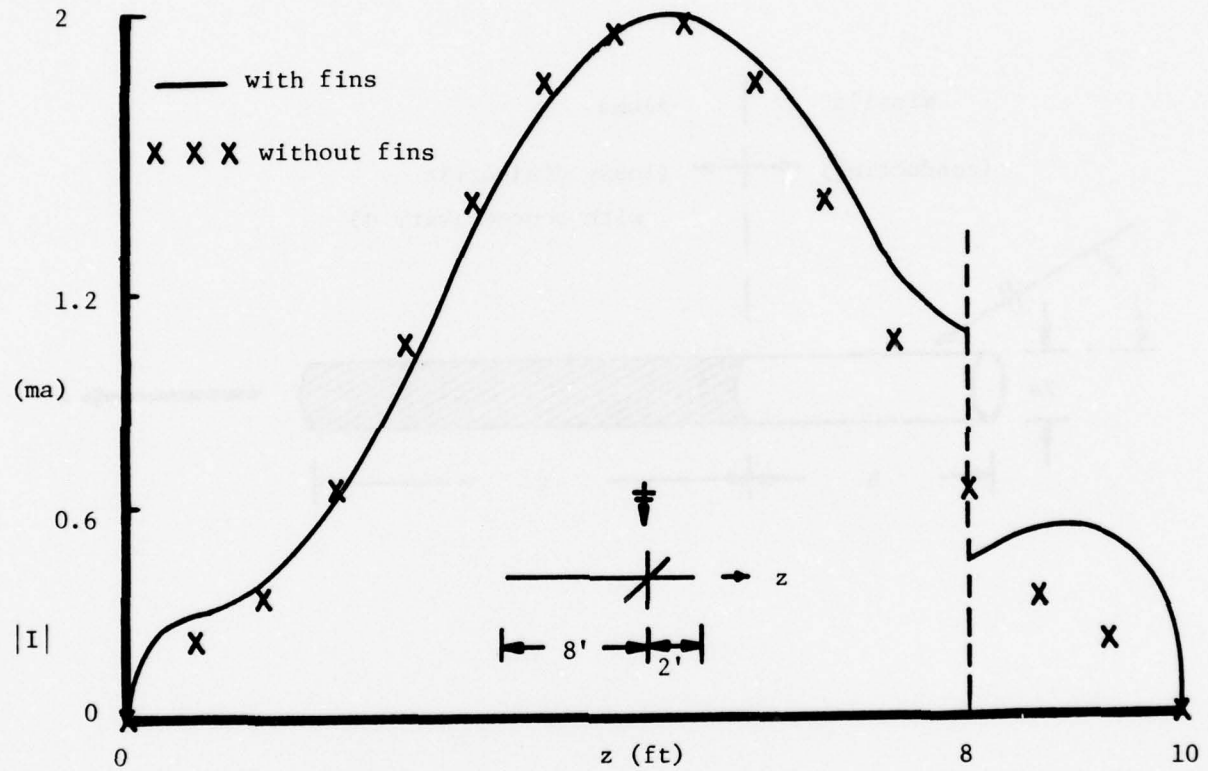


Fig. 2. Current magnitude on 10' missile (radius $a = 2.5''$) with and without presence of 8" crossed-wire simulating fins illuminated by a broadside incident plane wave ($f = 100$ MHz).

equation [6,7] via enforcing the boundary conditions on the wire:

$$-\frac{j\omega}{k_o^2} \left(\frac{d^2}{dz^2} + k_o^2 \right) A_z(z) + E_z^i(z) = E_z^{\text{total}} = Z(z)I(z) \quad (1)$$

where $Z(z)$ is the equivalent impedance along the wire and is given by

$$Z(z) = \begin{cases} 0 & , \dots \text{ for the conducting region,} \\ \frac{1}{\pi a^2 \sigma(z)} \left(\frac{\tau a}{2} \right) \frac{J_o(\tau a)}{J_1(\tau a)} & , \dots \text{ for the lossy region,} \end{cases} \quad (2)$$

and

$$\tau = (1-j) \sqrt{\omega \mu_o \sigma(z) / 2} = \frac{(1-j)}{\delta} \quad (3)$$

where δ is the skin depth of the material. The magnetic vector potential

$A_z(z)$ is given by

$$A_z(z) = \frac{\mu_o}{4\pi} \int_{\text{wire}} I(z') K(z-z') dz' , \quad (4)$$

$$K(\xi) = \exp(-jk_o R) / R \quad (5)$$

$$R = (\xi^2 + a^2)^{\frac{1}{2}} \quad (6)$$

$I(z)$ is the unknown axial current to be determined, and $E_z^i(z)$ is the known incident electric field. To solve Eq. (1) the method of moments is employed. First, Eq. (1) is tested with a set of triangle functions, then the unknown current $I(z)$ is expanded in a set of flat pulses with unknown coefficients

$I_n, n = 1, 2, \dots, N$. This results in a set of N independent algebraic equations. The unknown current coefficients I_n are then found using standard matrix inversion methods. The details are given in references [7,8] and will not be repeated here.

2.2. Numerical Results

Based on the analysis in the previous section, an efficient FORTRAN IV computer program was developed to find the unknown axial current on the missile and plume. Fig. 3 shows the wire code results for the real and imaginary part of the currents on a missile (radius $a = 0.02\lambda$, length $h = 1.11\lambda$) with plume (of same radius and length as the missile, $\epsilon_r = 1$, $\sigma = 0.1 \text{ S/m}$) illuminated by a broadside incident plane wave (freq. = 19.6 MHz). Here the wire code results agree very well with the numerical results computed by Taylor [1]. Once the validity of this wire code has been established, one may readily study the effects on the missile currents due to the presence of the plume when the frequency, plume conductivity, and incident angle of the plane wave sources are varied.

A three-dimensional view of the current amplitude on a missile ($h = 10'$, $a = 2.5''$) and plume ($\ell = 20'$) is plotted in Fig. 6 as functions of the plume conductivity ($\sigma = 0, 0.01, 0.05, 0.2, 0.5, 1$ and 2 S/m) and the distance along the axis of the missile-plume configuration with a broadside incident plane wave (freq. = 50 MHz). The case of zero plume conductivity represents a missile with no plume present. One may notice that when σ is 0.01 S/m there is little effect caused by the presence of the plume. When σ is increased to 1 or 2 S/m , however, then rather significant differences in currents take place. Plots for other frequencies (e.g., 20, 35, 60, 70, 90, 100

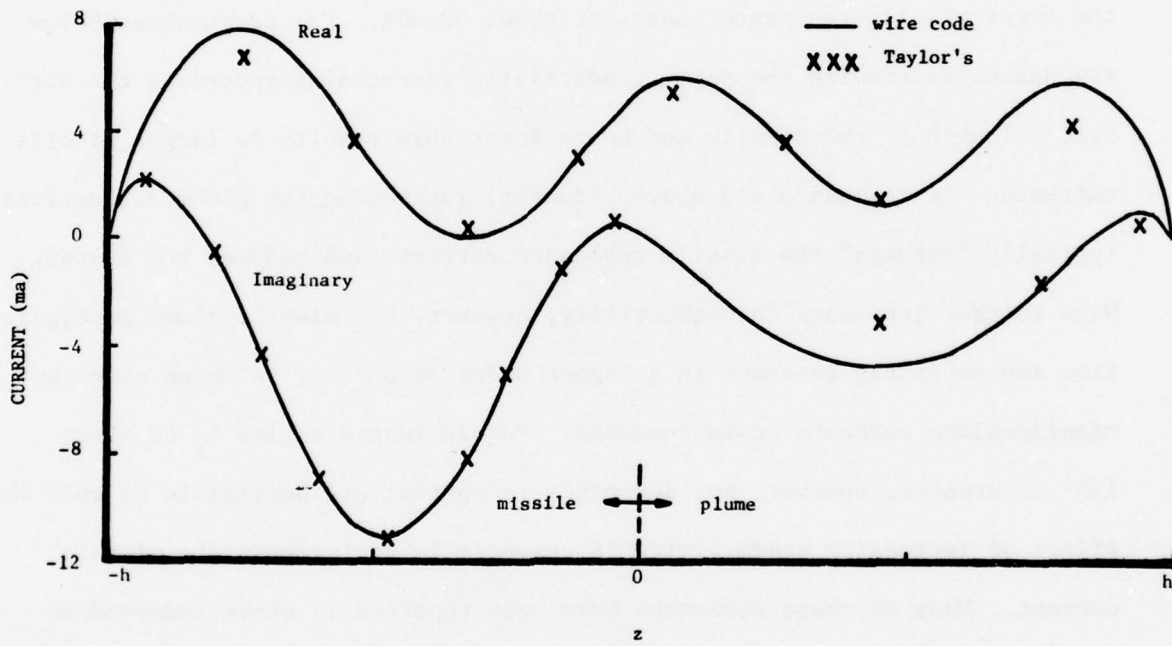


Fig. 3. Comparison between wire code and Taylor's solution for the current on a missile with plume ($h = \ell = 1.11\lambda$, $a = 0.02\lambda$, $\sigma = 0.1 \text{ mho/m}$) illuminated by a broadside incident plane wave ($f = 19.6 \text{ MHz}$).

and 120 MHz) are shown in Figs. 4-5 and 7-12, for a broadside incidence plane wave. For an incidence angle (θ_i) of 120° , Figs. 13-15 show the current amplitudes at 20, 50, and 100 MHz, respectively, as functions of the plume conductivity and positions along the axis of the missile and plume. Figs. 16-19 present current data for the case of 150° incidence angle at 35, 50, 100, and 120 MHz. Figs. 20-42 show current plots for other angles of incidence at 20, 35, 50, 100, and 120 MHz.

The frequencies considered may be divided into two categories; those below the first missile resonance and those above the first resonance, where the first missile resonance occurs at about 50 MHz. For frequencies below resonance, increasing the plume conductivity essentially increases the electrical length of the missile and hence invariably results in larger missile currents. At resonance and above, however, increasing the plume conductivity typically "detunes" the missile resonance currents and reduces the current. With further increases in conductivity, however, the missile-plume configuration may be nearly resonant in a higher order resonance, in which case the missile-plume currents again increase. For incidence angles θ_i of about 150° or greater, however, any decreases in current are negligible so that the effect of increasing conductivity is essentially to increase the missile current. Many of these phenomena have been reported in other independent studies [4].

The effect of the incident angle θ_i on the missile current distribution may also be plotted in a polar diagram. Figs. 43-45 show the current magnitude at the middle of the missile with and without plume for frequencies of 50, 100, and 120 MHz, respectively. The current magnitudes at 3' from the

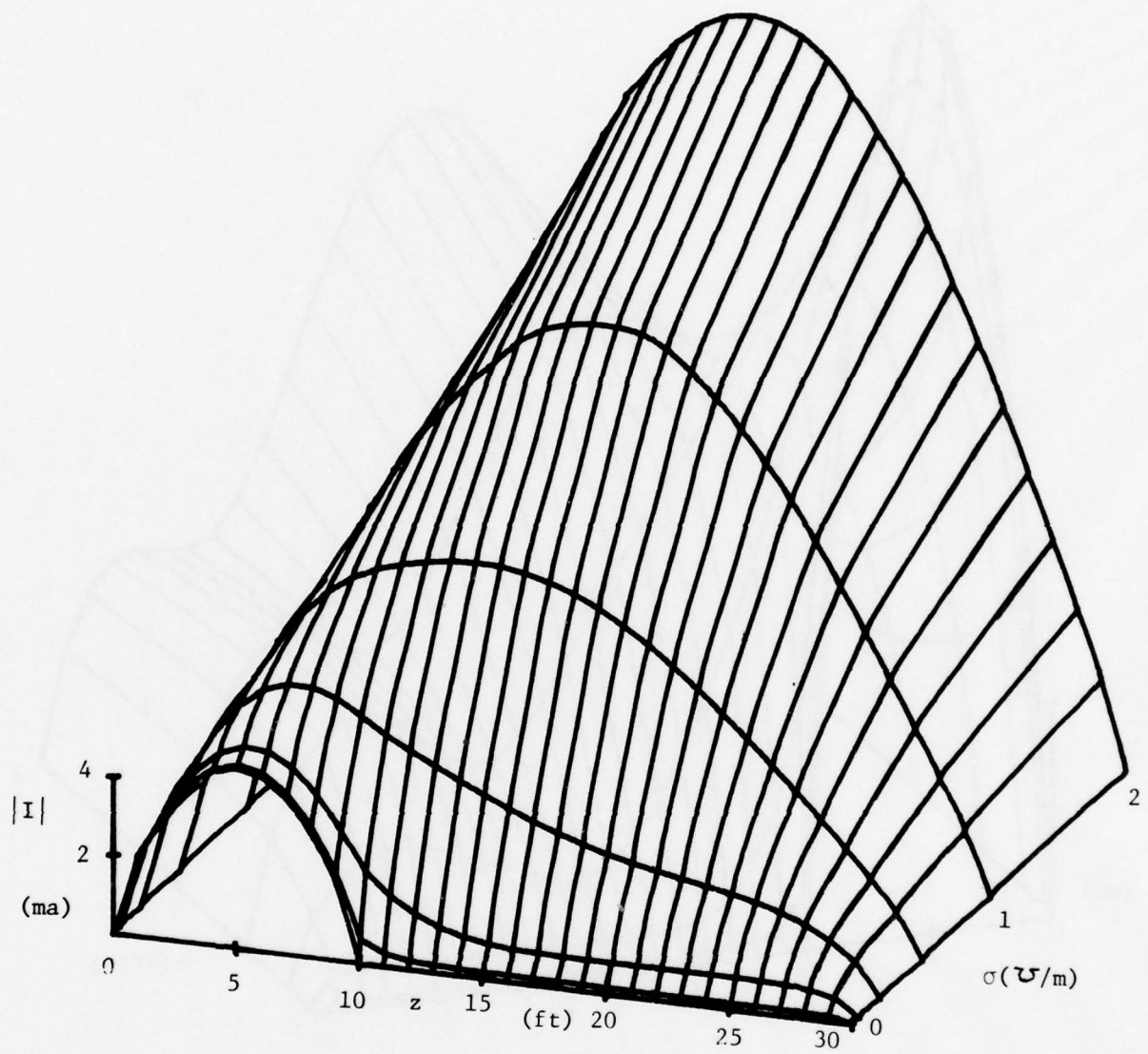


Fig. 4. Contour plot of current magnitude as functions of the length along the missile-plume axis and the plume conductivity σ (Broadside incidence, $f = 20$ MHz).

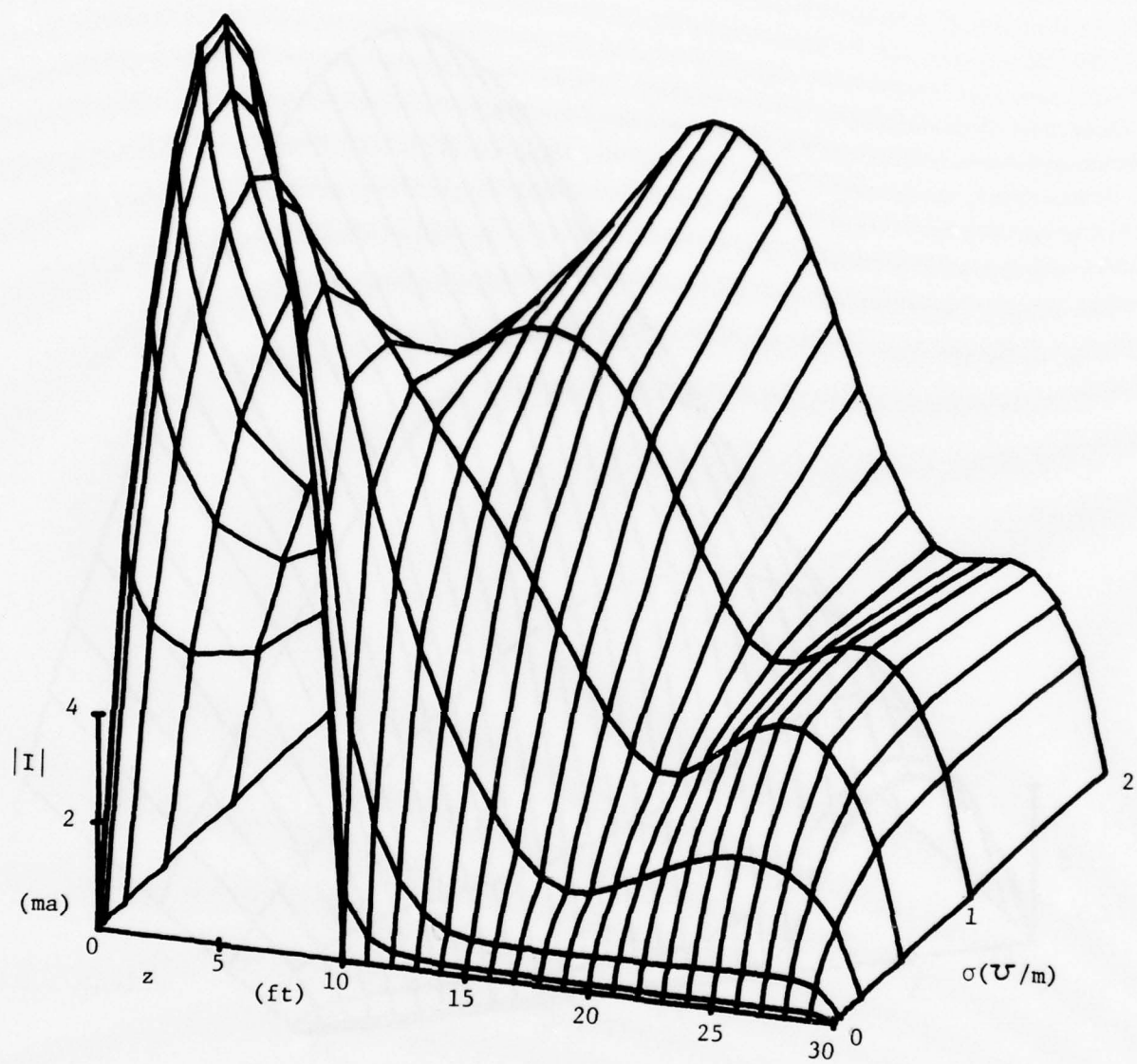


Fig. 5. Contour plot of $|I|$, $\theta_i = 90^\circ$, $f = 35$ MHz.

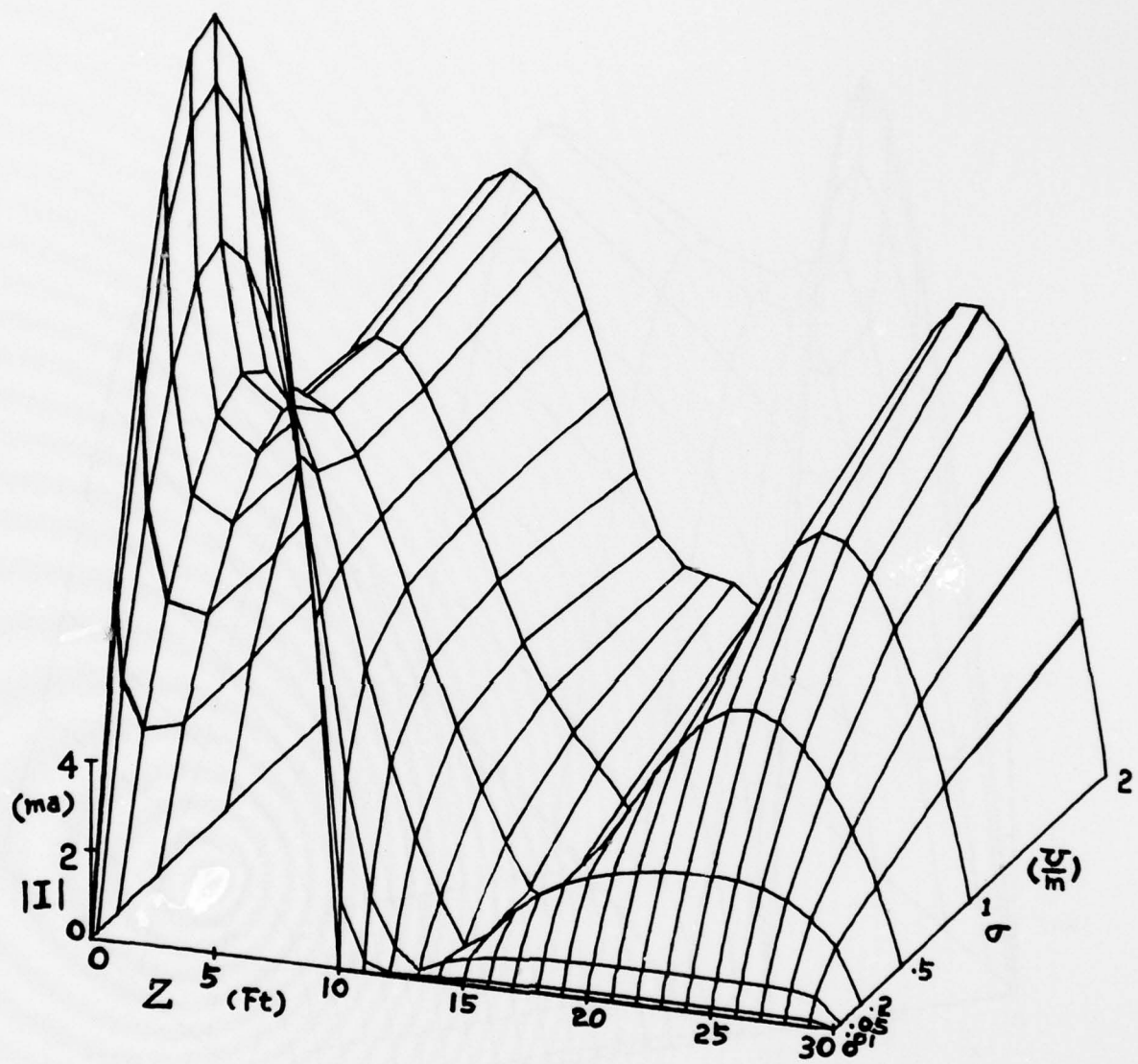


Fig. 6. Contour plot of $|I|$, $\theta_i = 90^\circ$, $f = 50$ MHz.

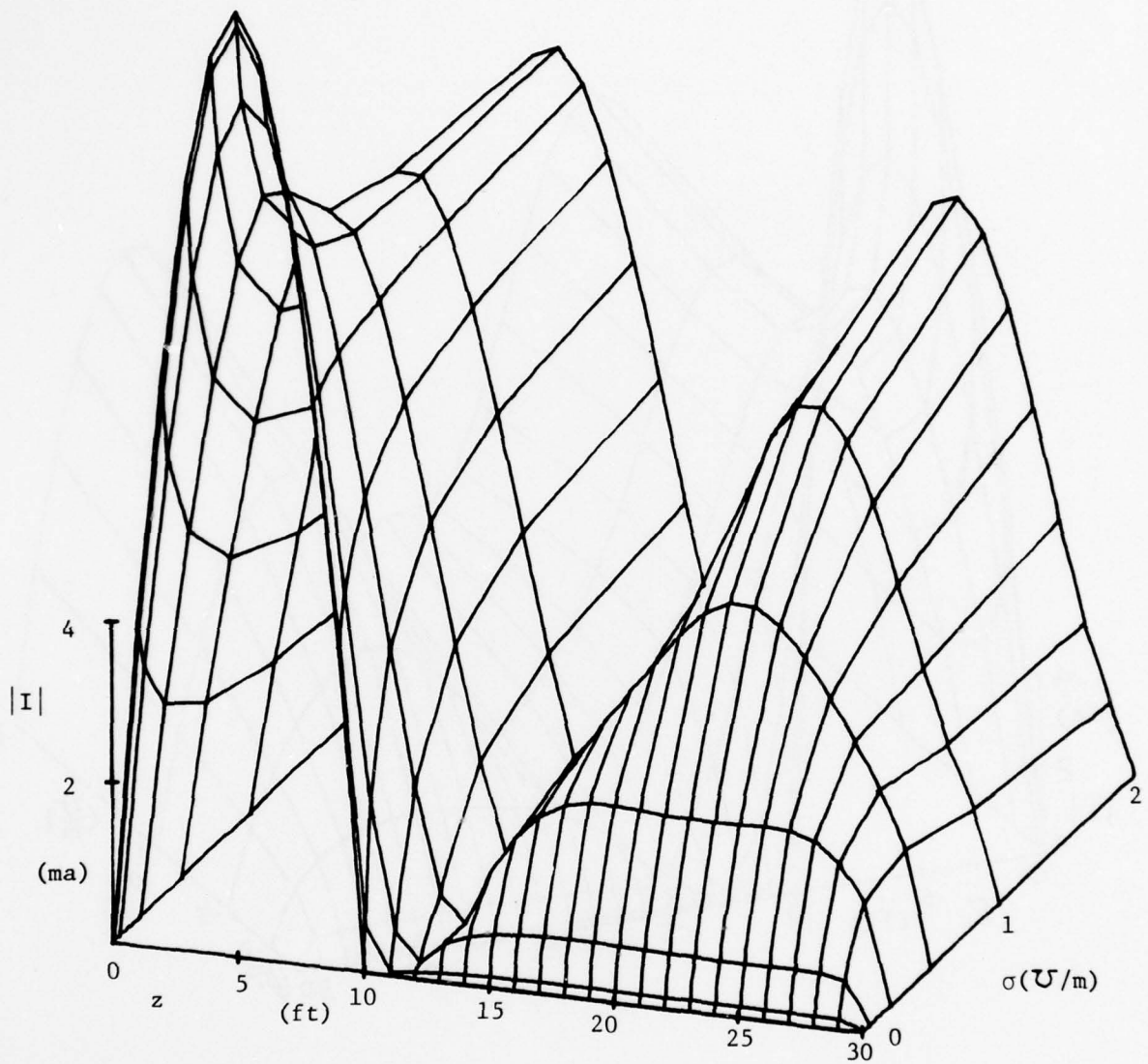


Fig. 7. Contour plot of $|I|$, $\theta_i = 90^\circ$, $f = 60$ MHz.

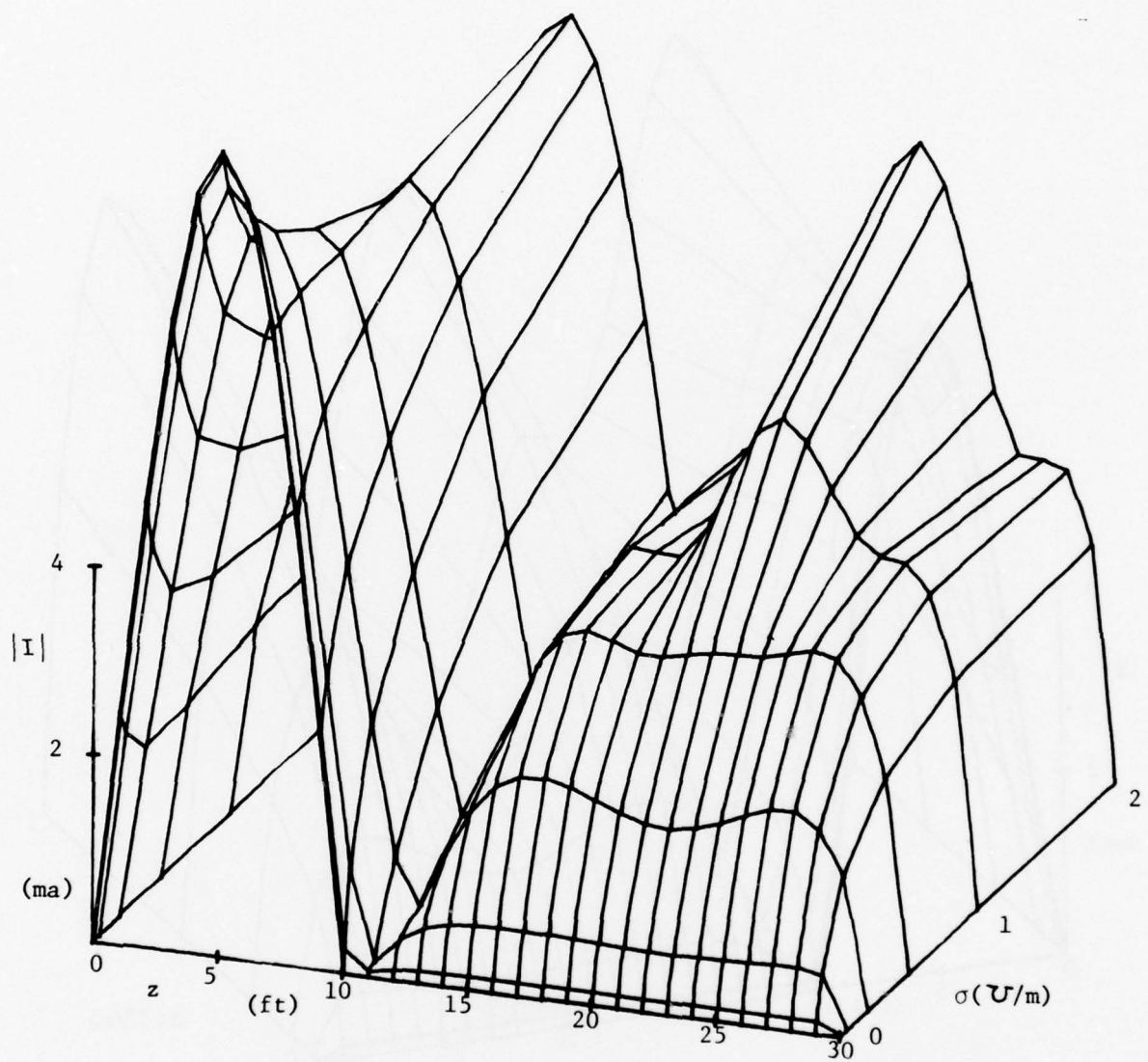


Fig. 8. Contour plot of $|I|$, $\theta_i = 90^\circ$, $f = 70$ MHz.

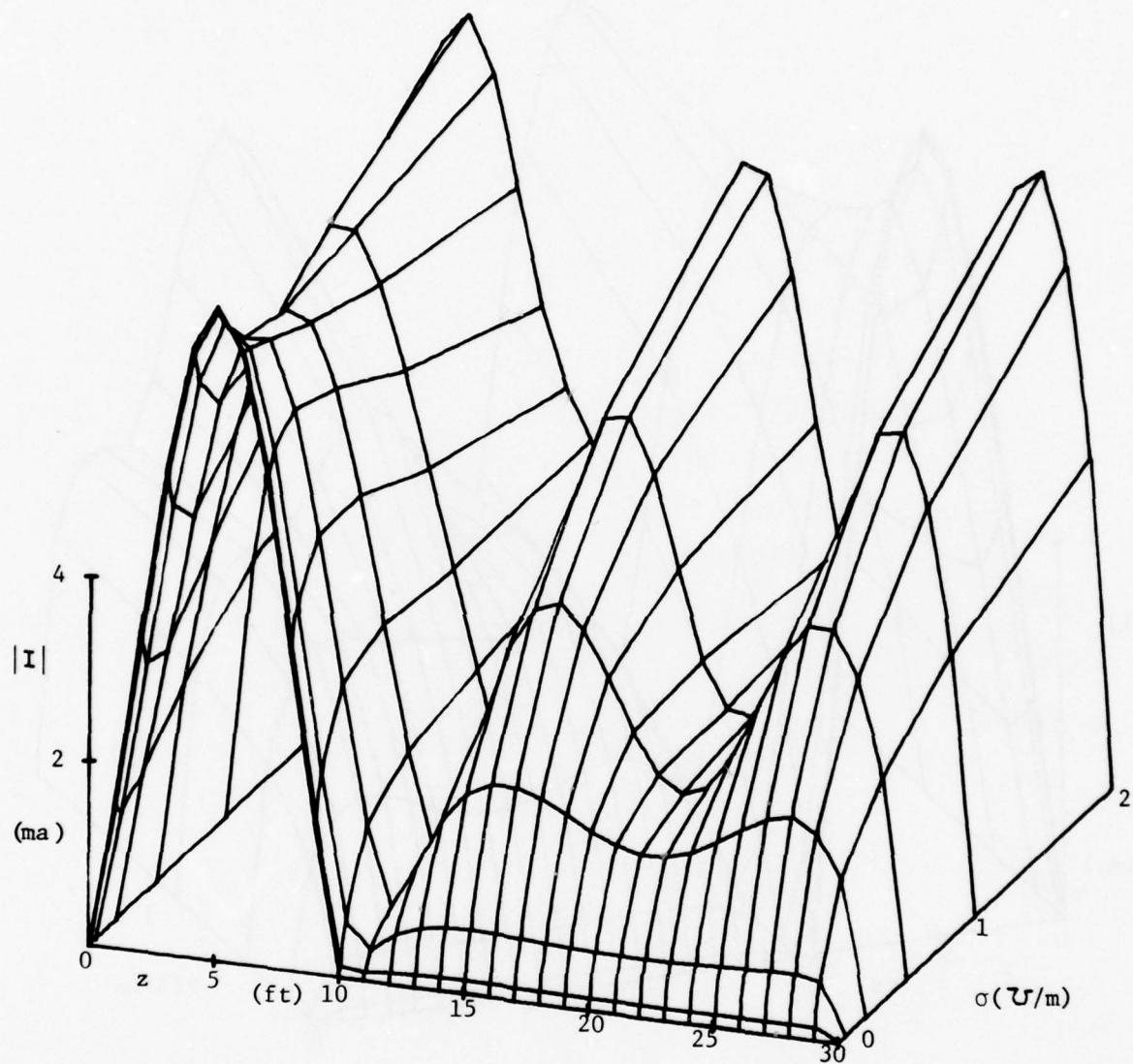


Fig. 9. Contour plot of $|I|$, $\theta_i = 90^\circ$, $f = 80$ MHz.

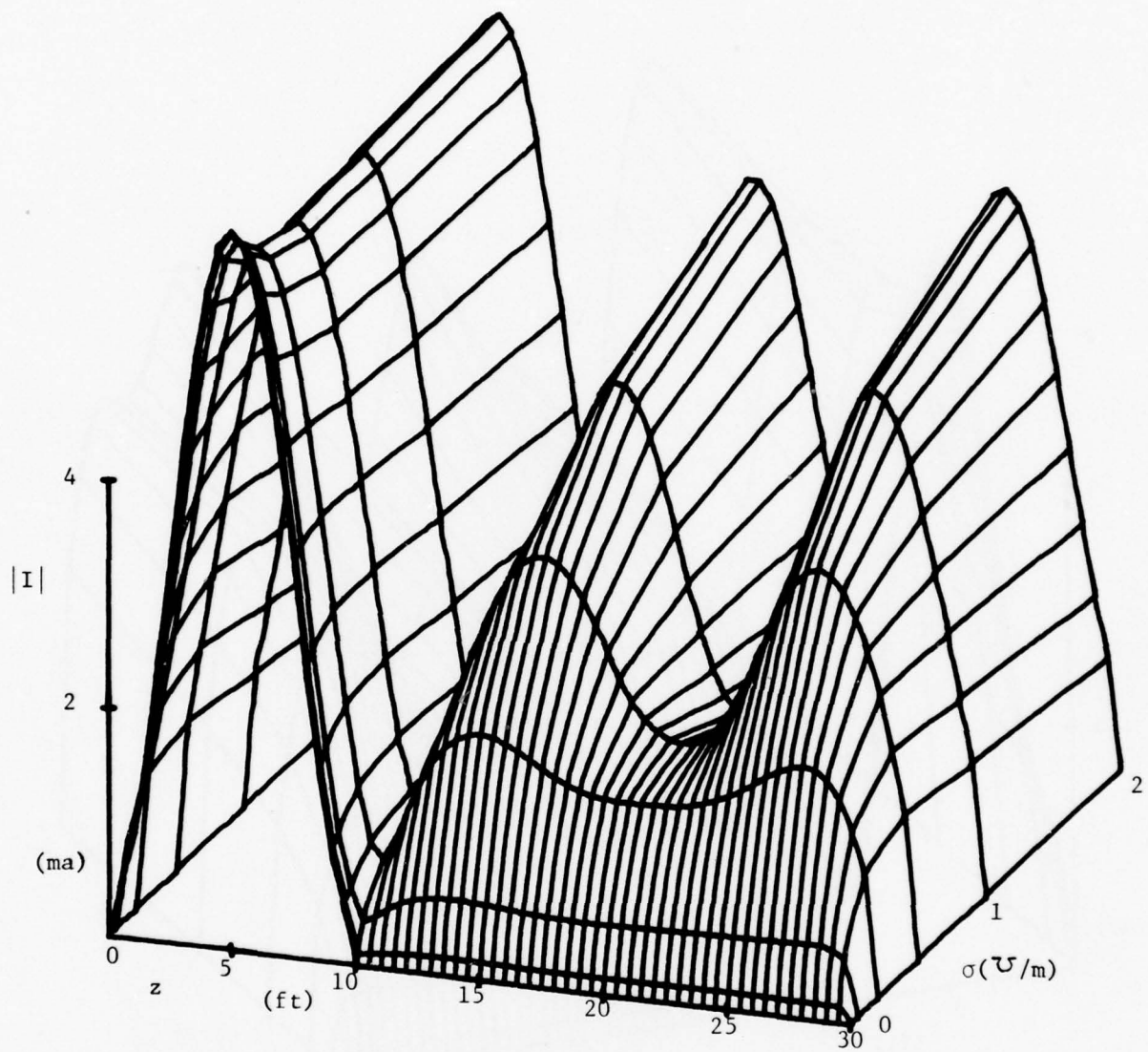


Fig. 10. Contour plot of $|I|$, $\theta_i = 90^\circ$, $f = 90$ MHz.

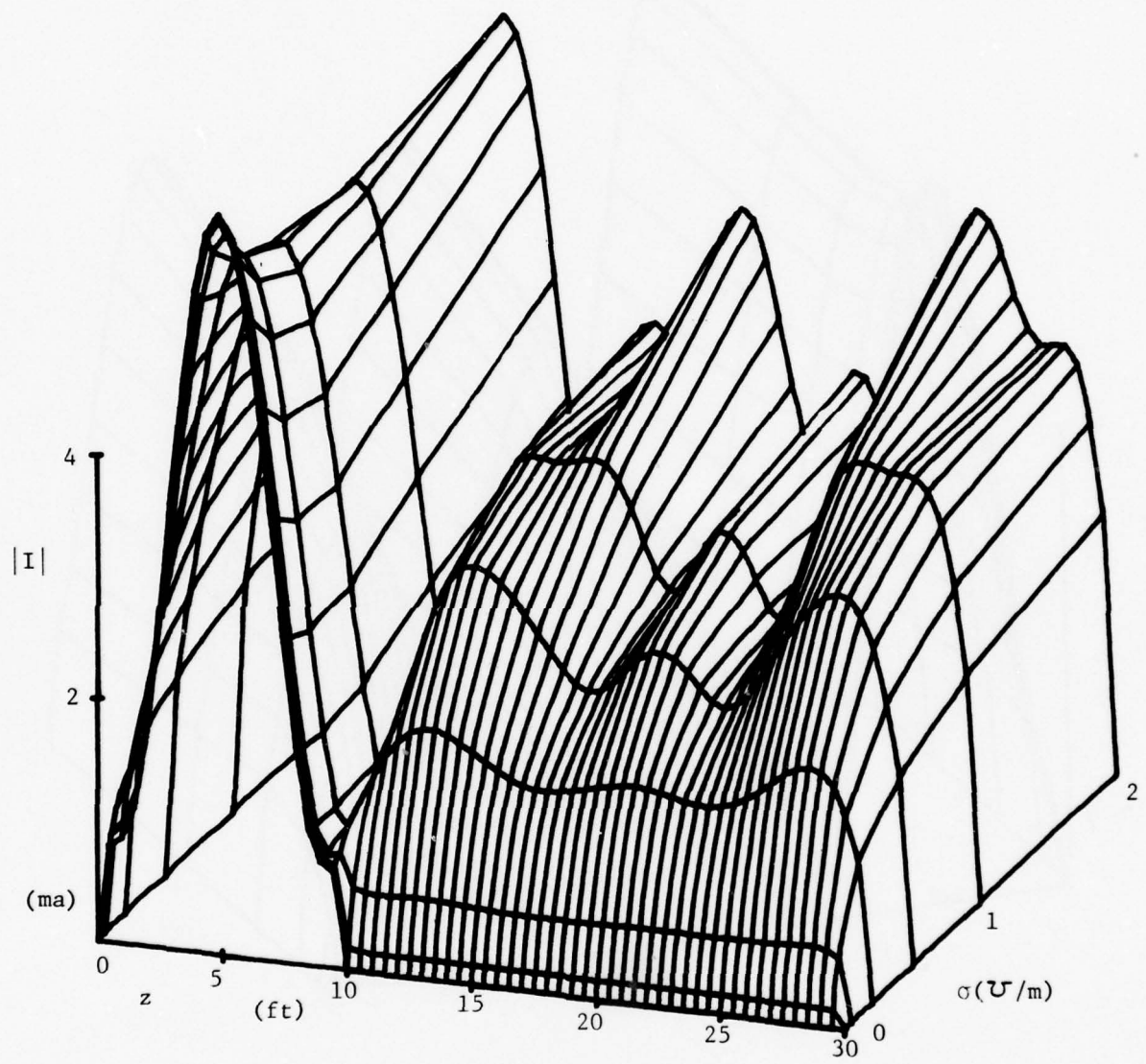


Fig. 11. Contour plot of $|I|$, $\theta_i = 90^\circ$, $f = 100$ MHz.

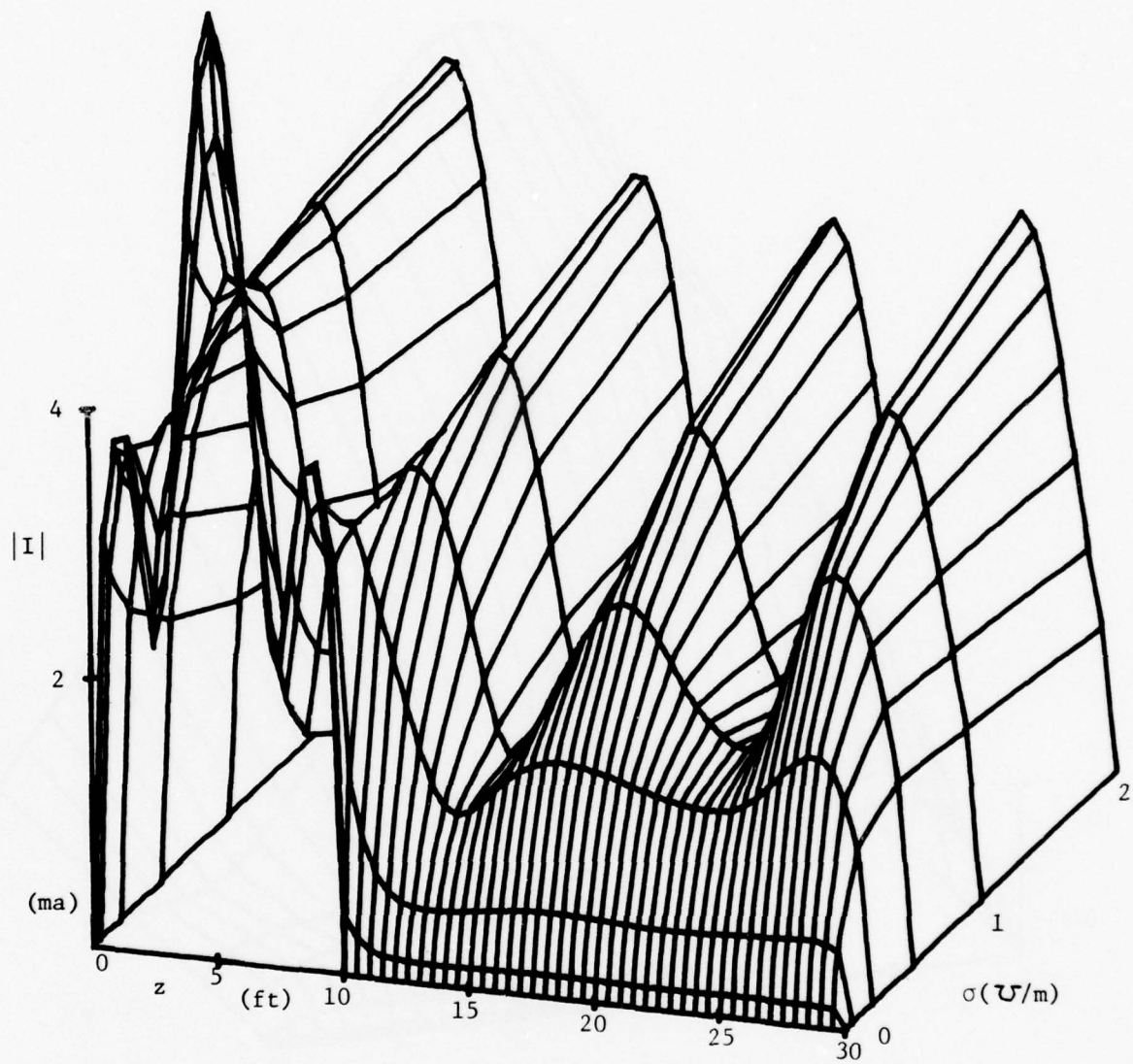


Fig. 12. Contour plot of $|I|$, $\theta_i = 90^\circ$, $f = 120$ MHz.

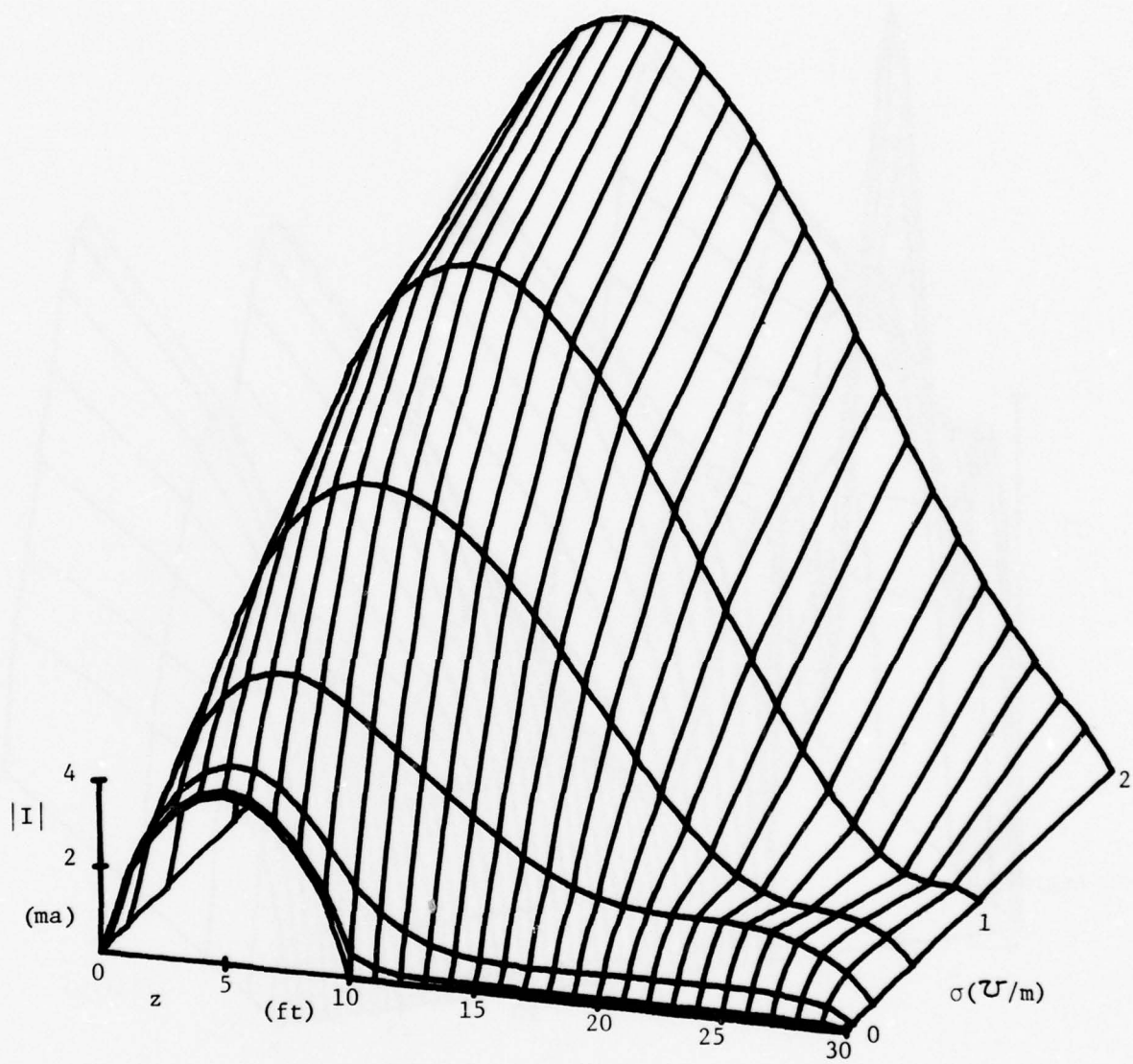


Fig. 13. Contour plot of $|I|$, $\theta_i = 120^\circ$, $f = 20 \text{ MHz}$.

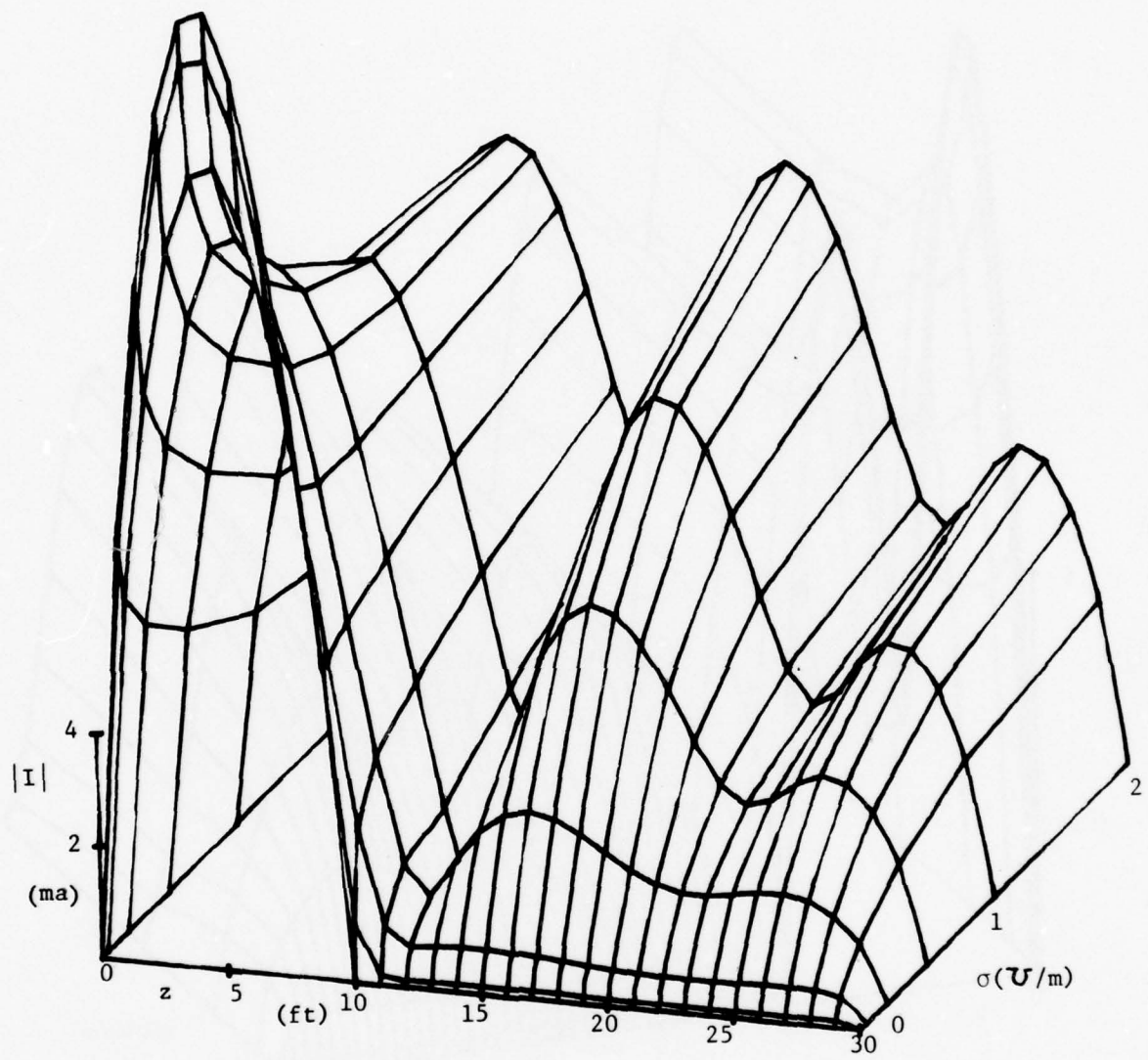


Fig. 14. Contour plot of $|I|$, $\theta_i = 120^\circ$, $f = 50$ MHz.

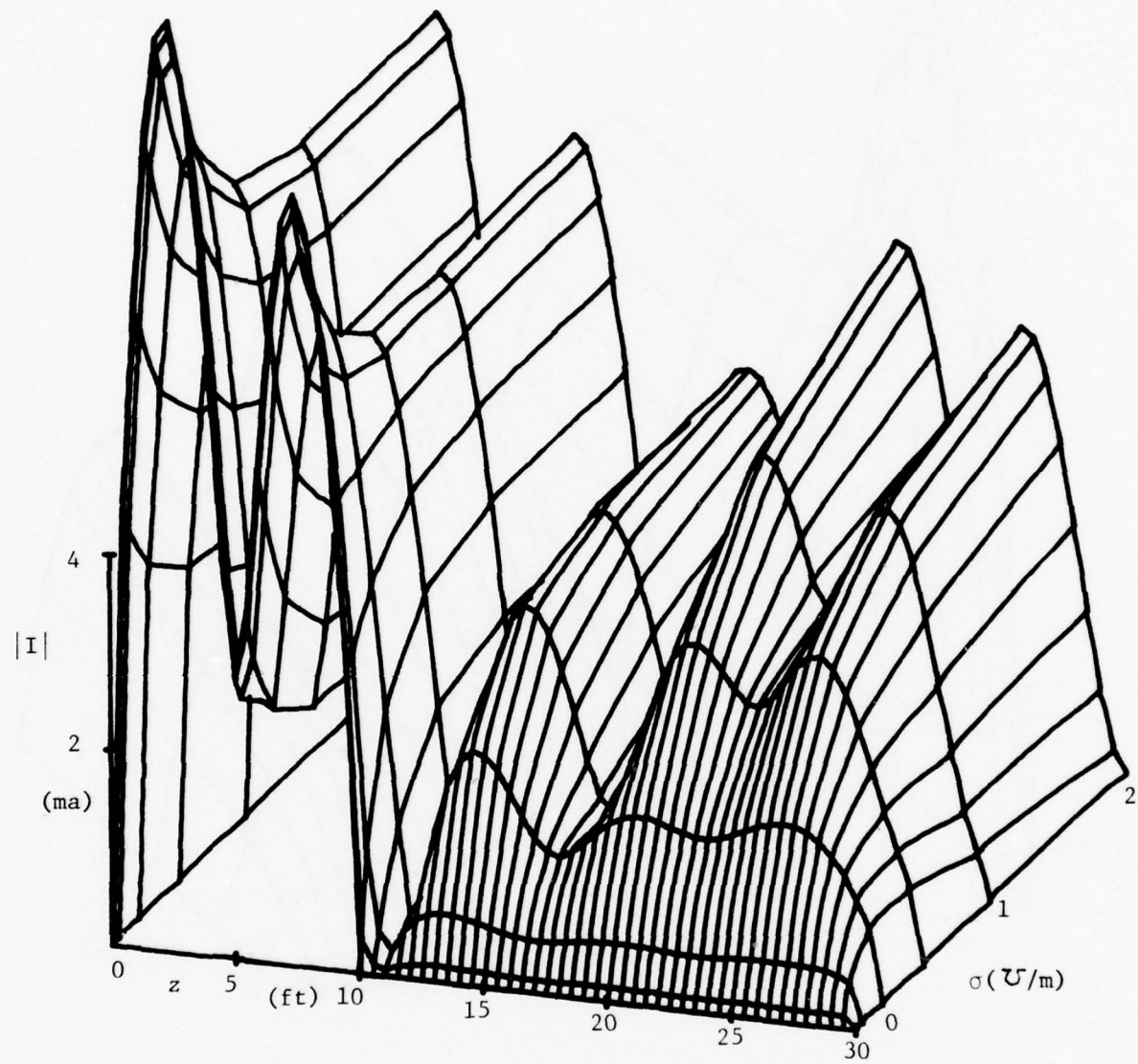


Fig. 15. Contour plot of $|I|$, $\theta_i = 120^\circ$, $f = 100$ MHz.

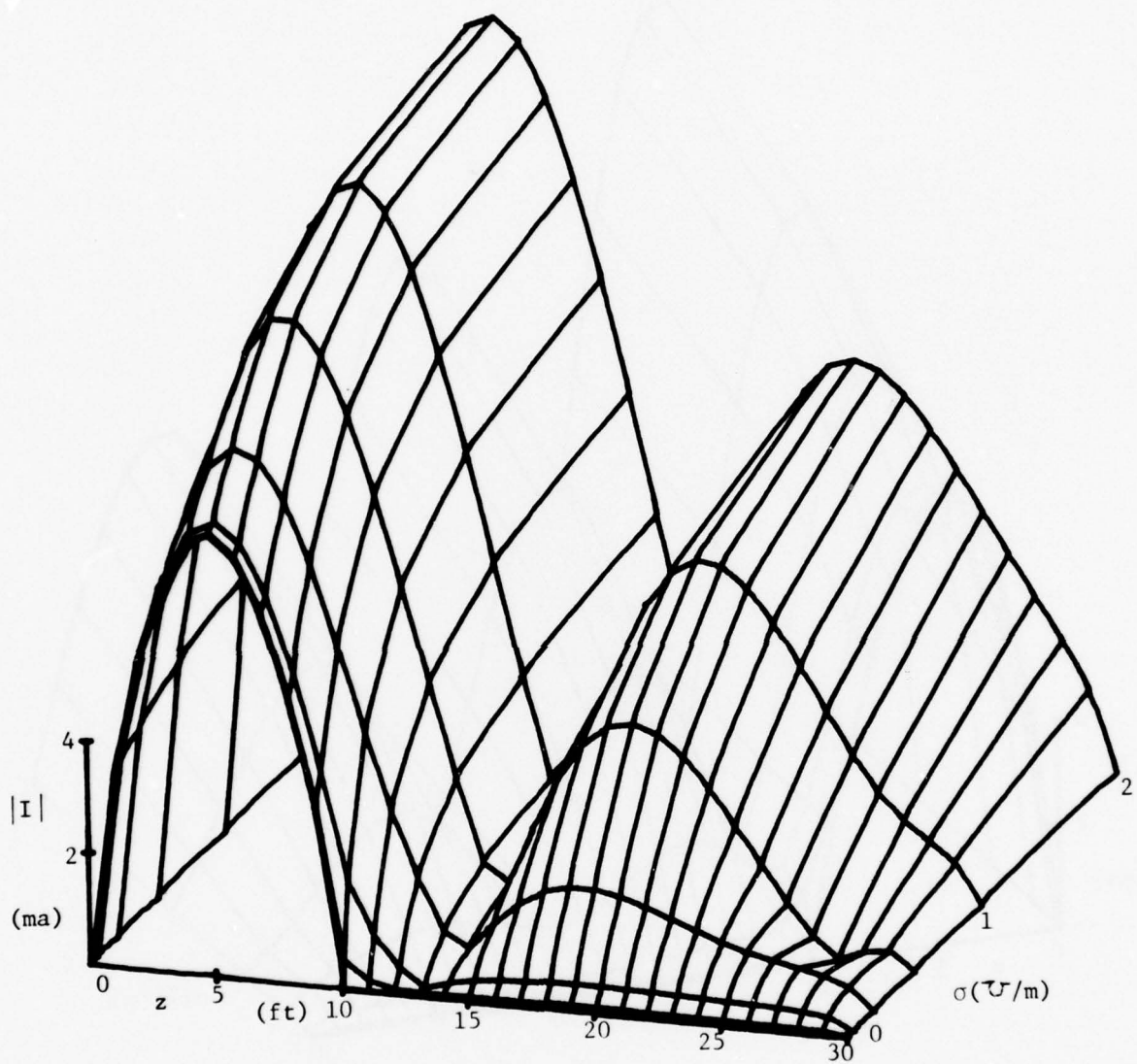


Fig. 16. Contour plot of $|I|$, $\theta_i = 150^\circ$, $f = 35$ MHz.

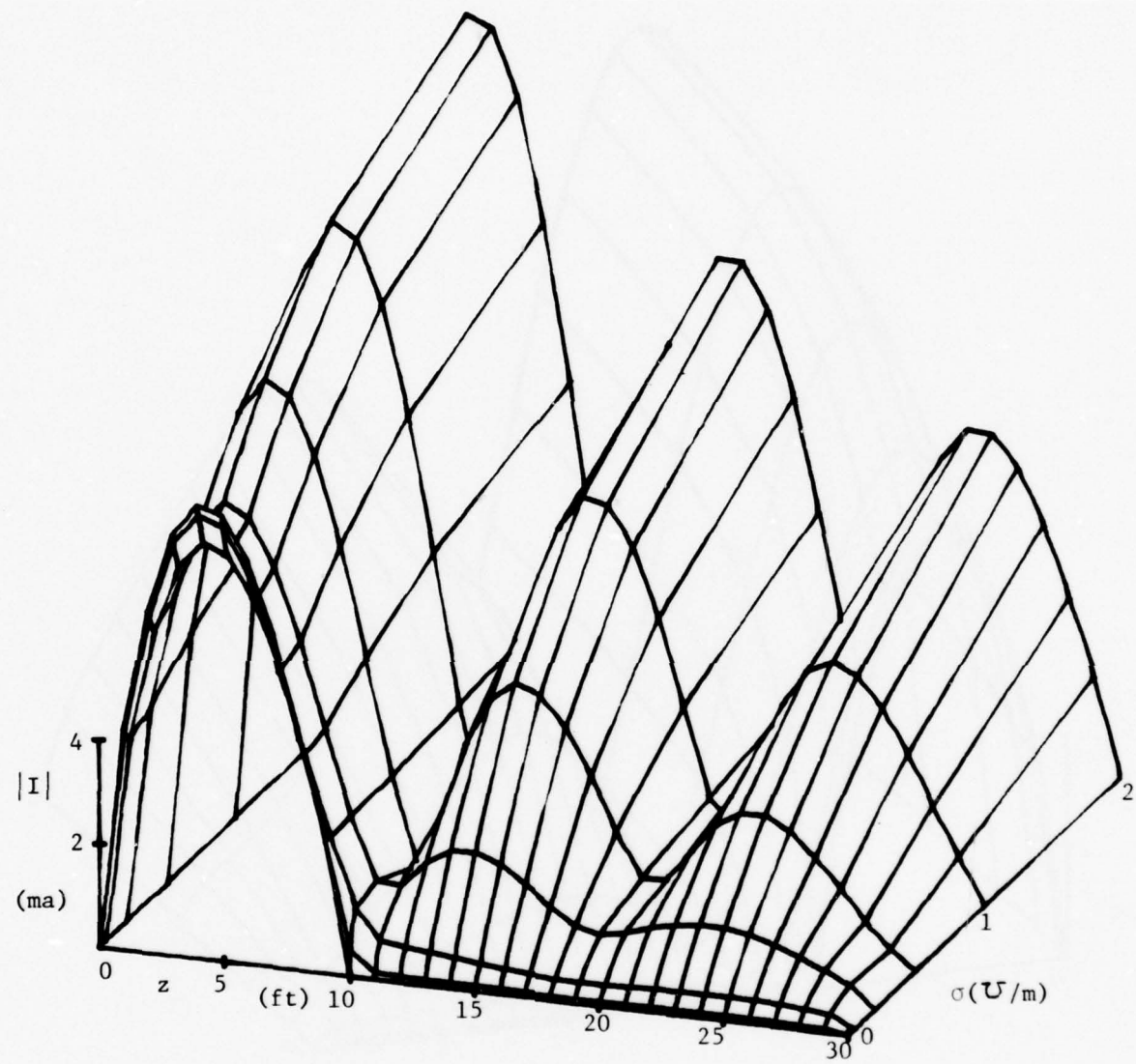


Fig. 17. Contour plot of $|I|$, $\theta_i = 150^\circ$, $f = 50$ MHz.

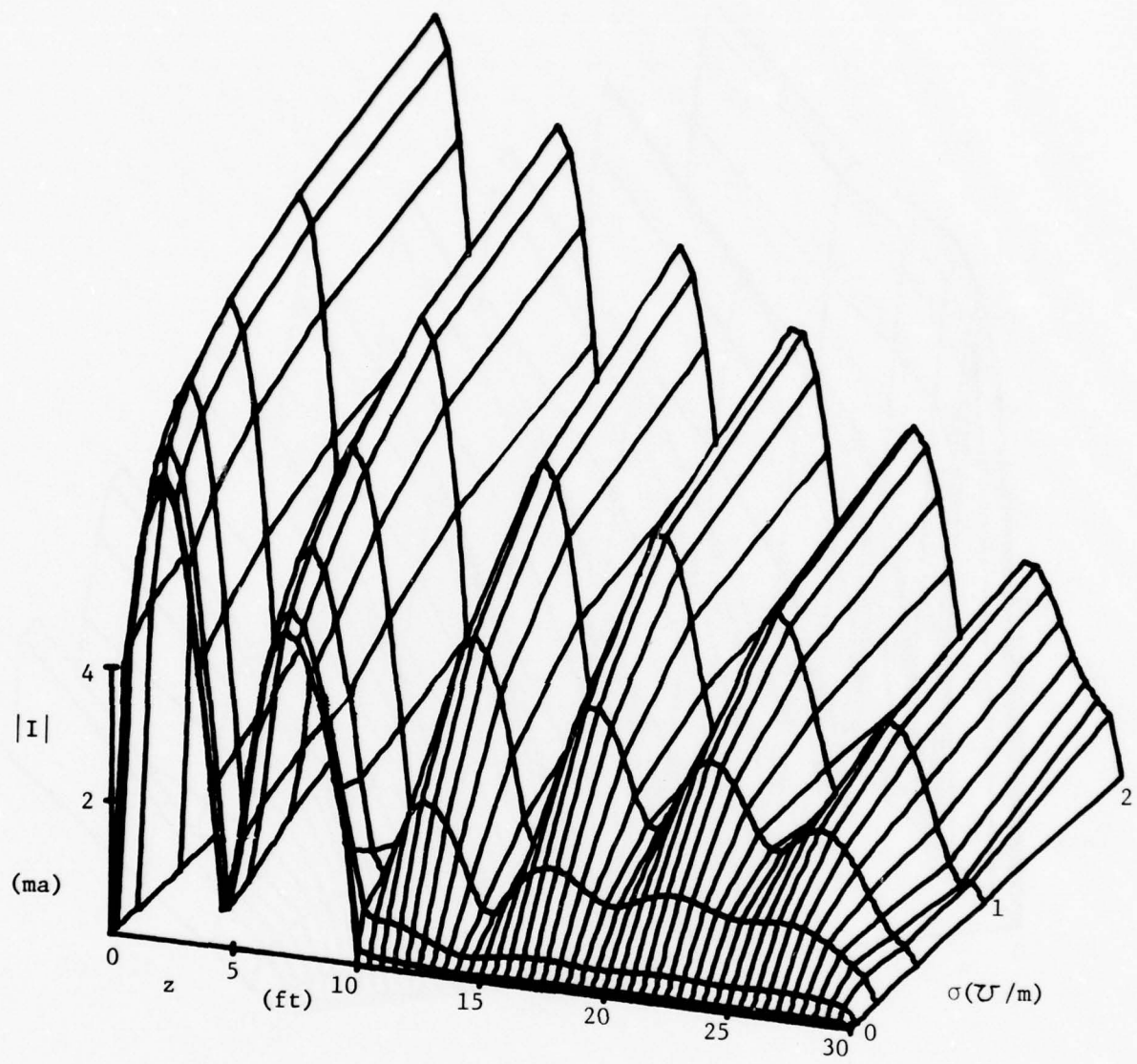


Fig. 18. Contour plot of $|I|$, $\theta_i = 150^\circ$, $f = 100$ MHz.

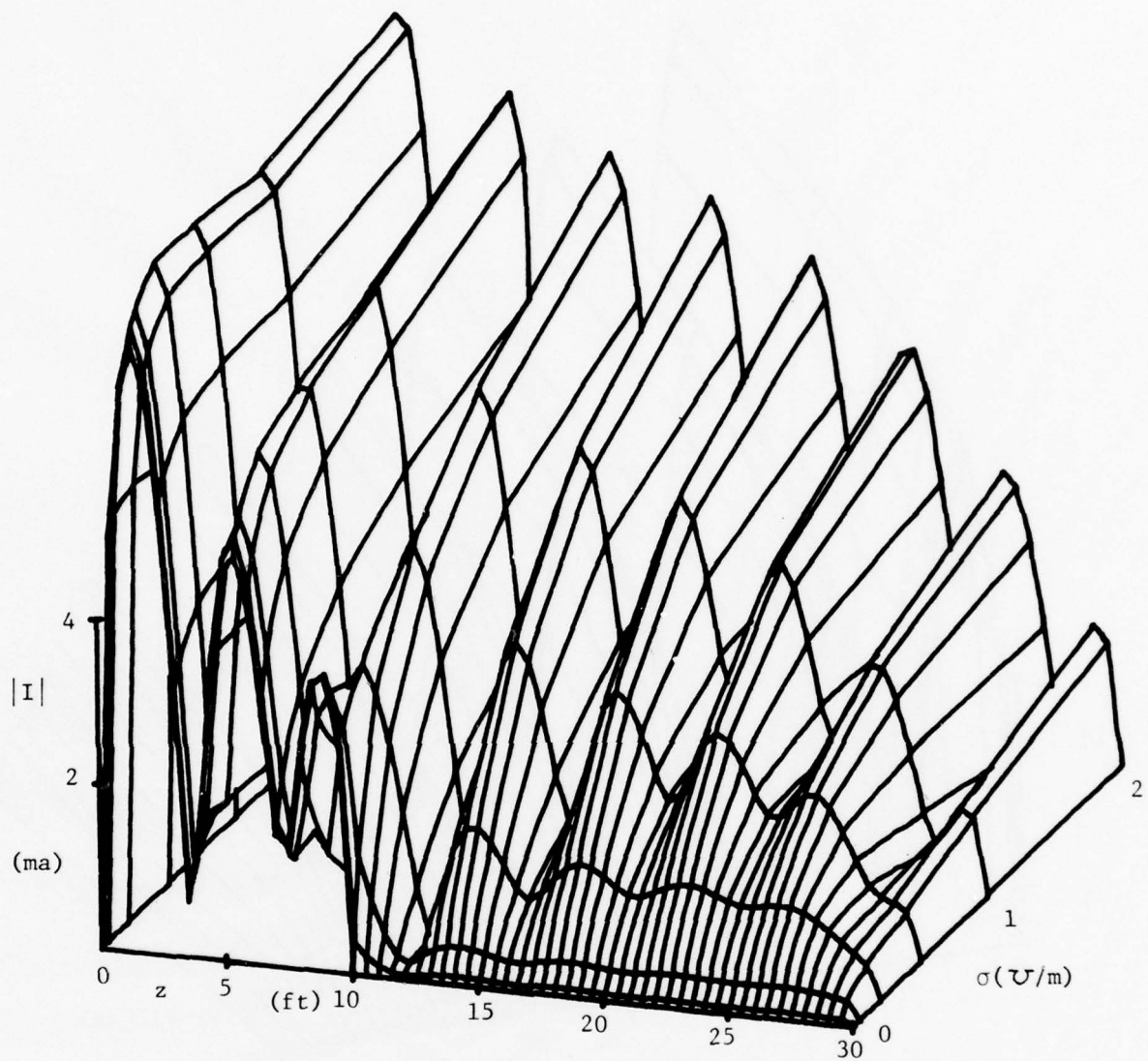


Fig. 19. Contour plot of $|I|$, $\theta_i = 150^\circ$, $f = 120 \text{ MHz}$.

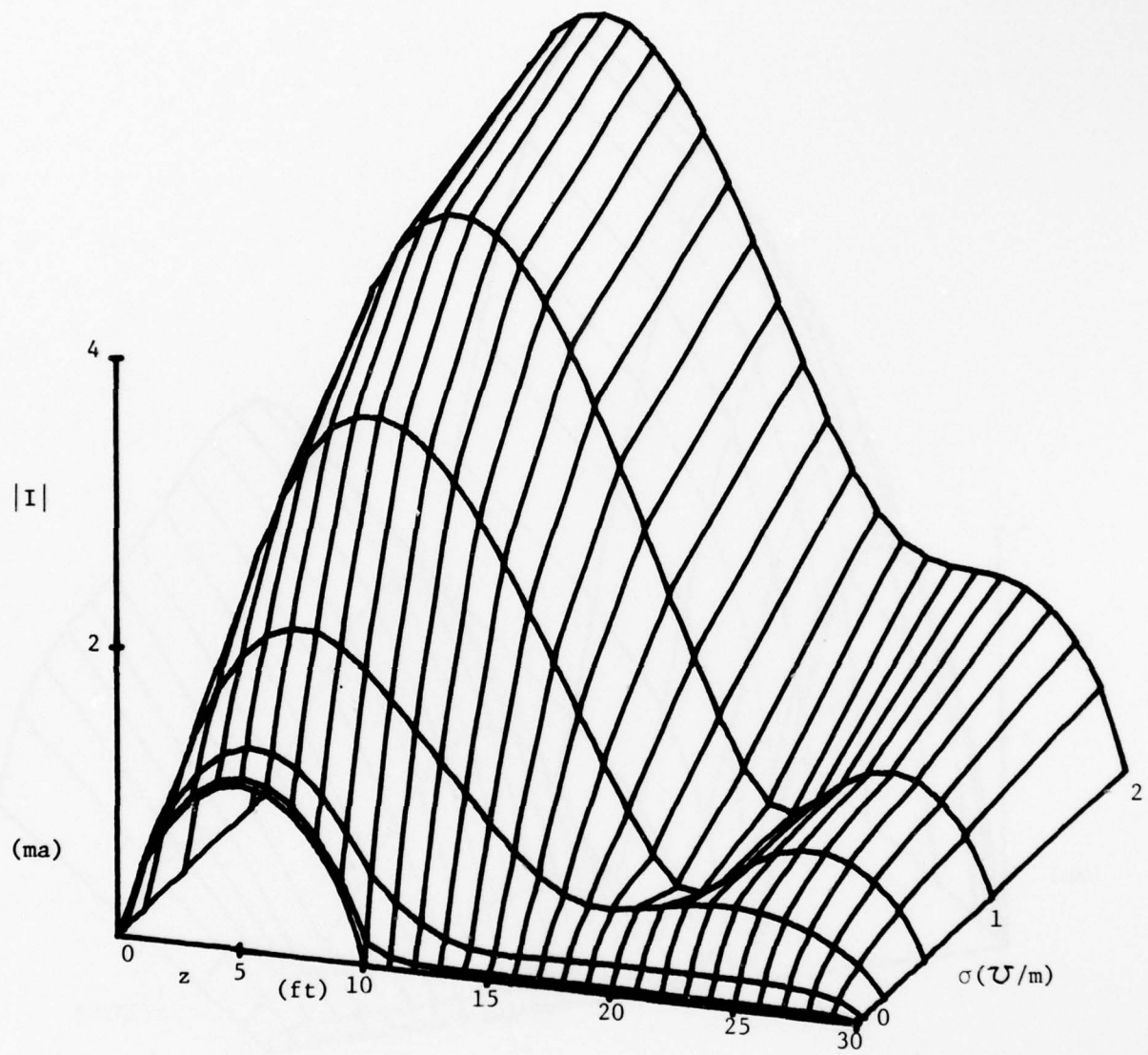


Fig. 20. Contour plot of $|I|$, $\theta_i = 165^\circ$, $f = 20$ MHz.

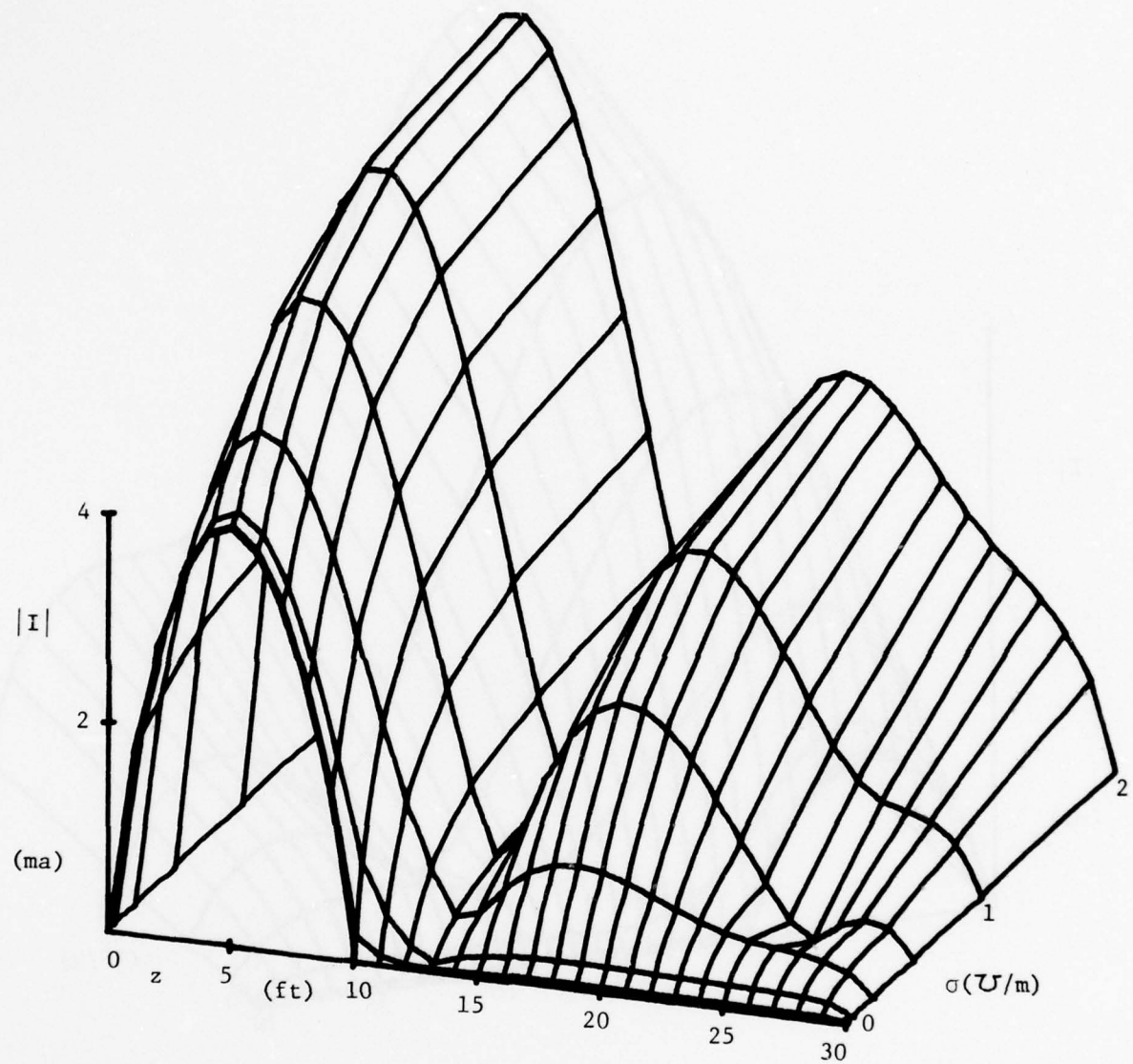


Fig. 21. Contour plot of $|I|$, $\theta_i = 165^\circ$, $f = 35$ MHz.

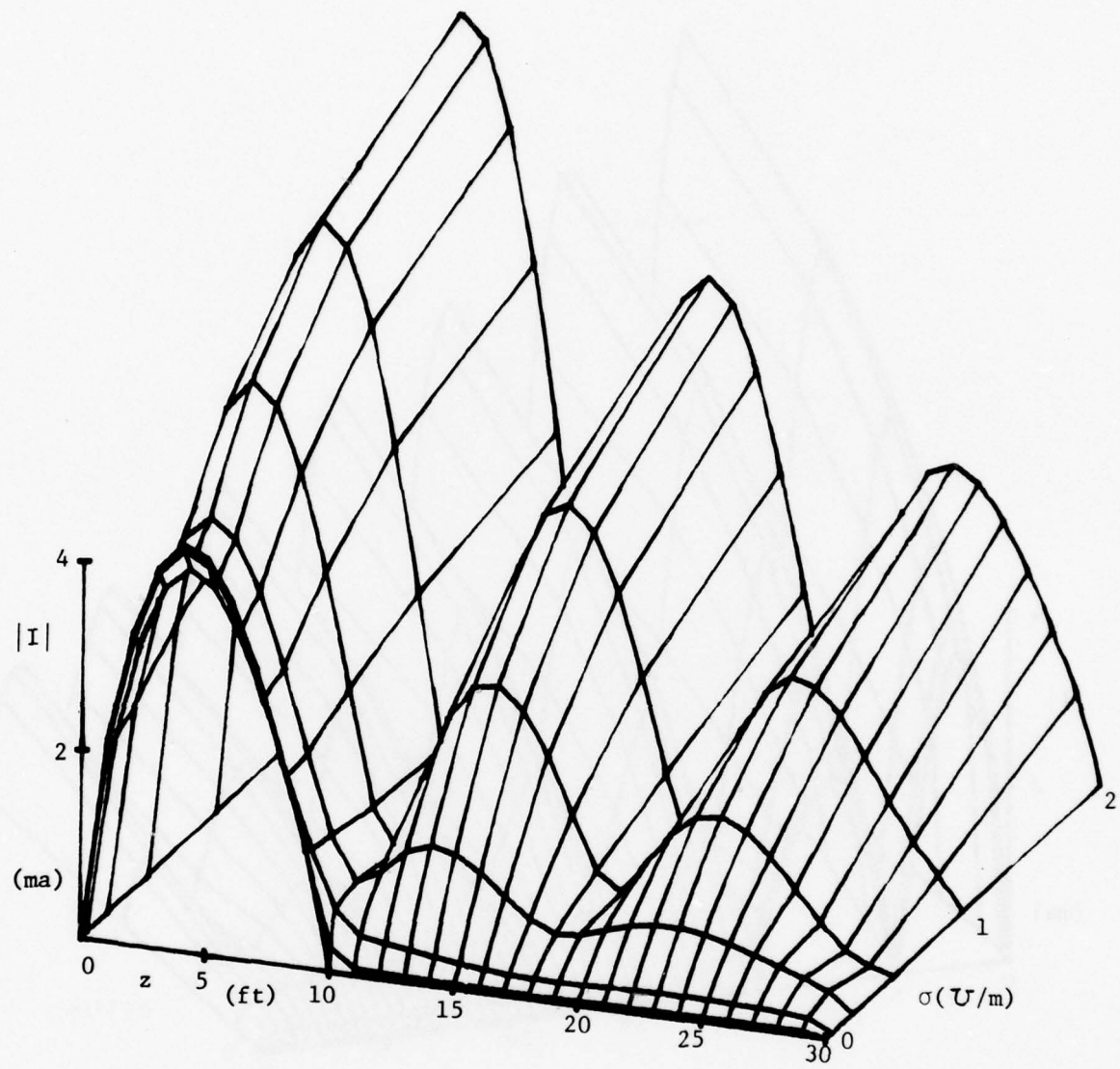


Fig. 22. Contour plot of $|I|$, $\theta_i = 165^\circ$, $f = 50$ MHz.

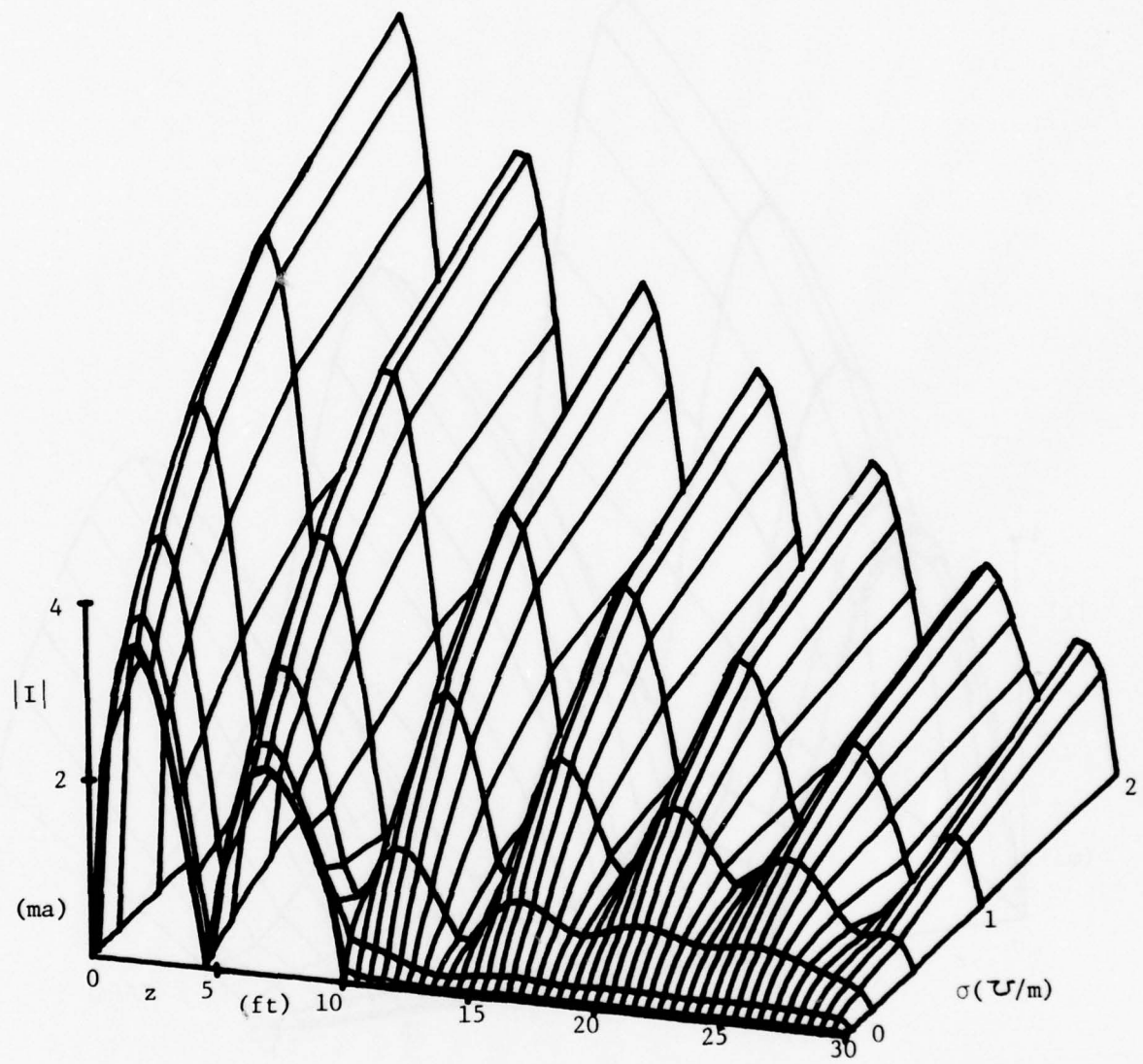


Fig. 23. Contour plot of $|I|$, $\theta_i = 165^\circ$, $f = 100$ MHz.

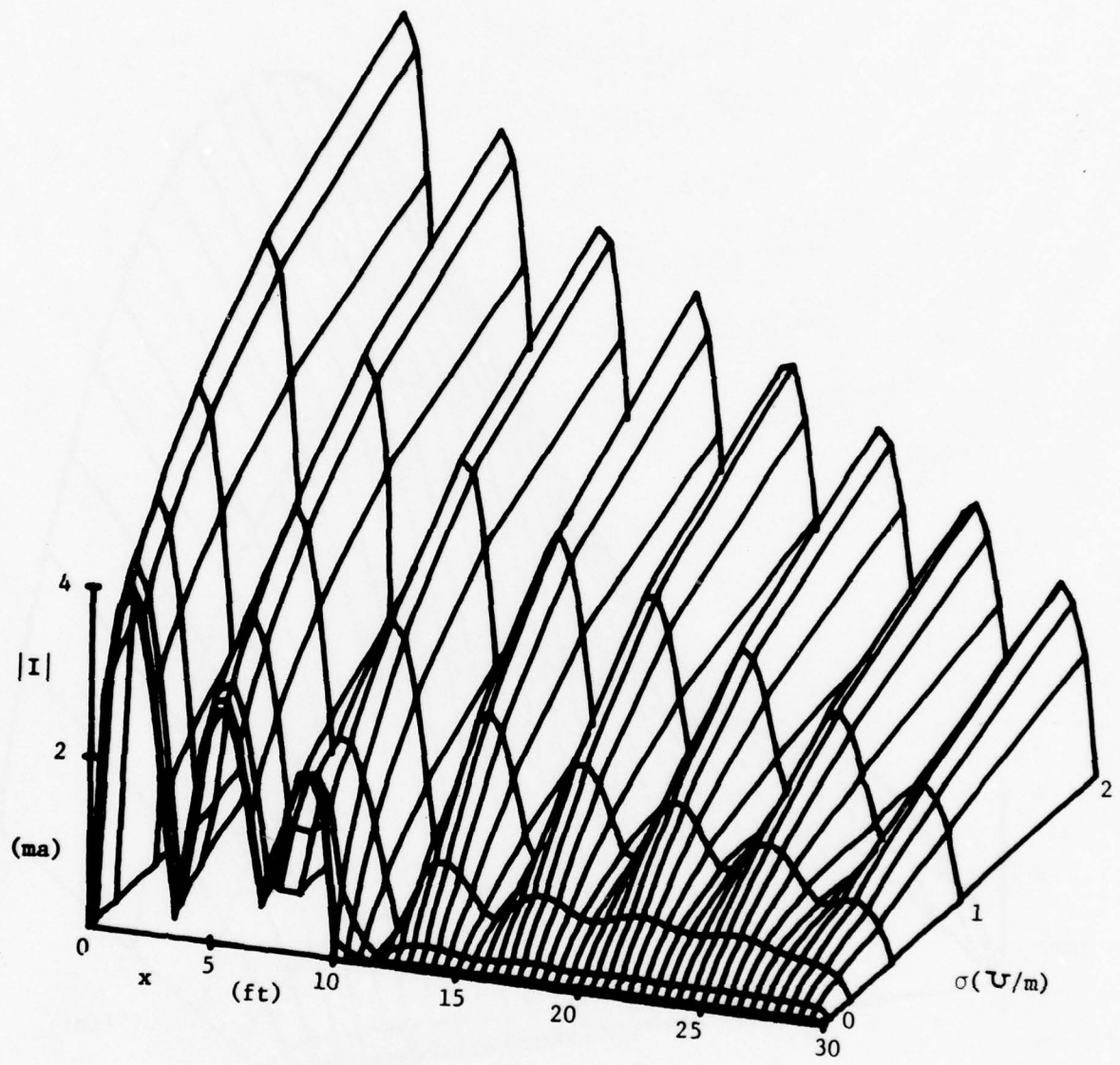


Fig. 24. Contour plot of $|I|$, $\theta_1 = 165^\circ$, $f = 120$ MHz.

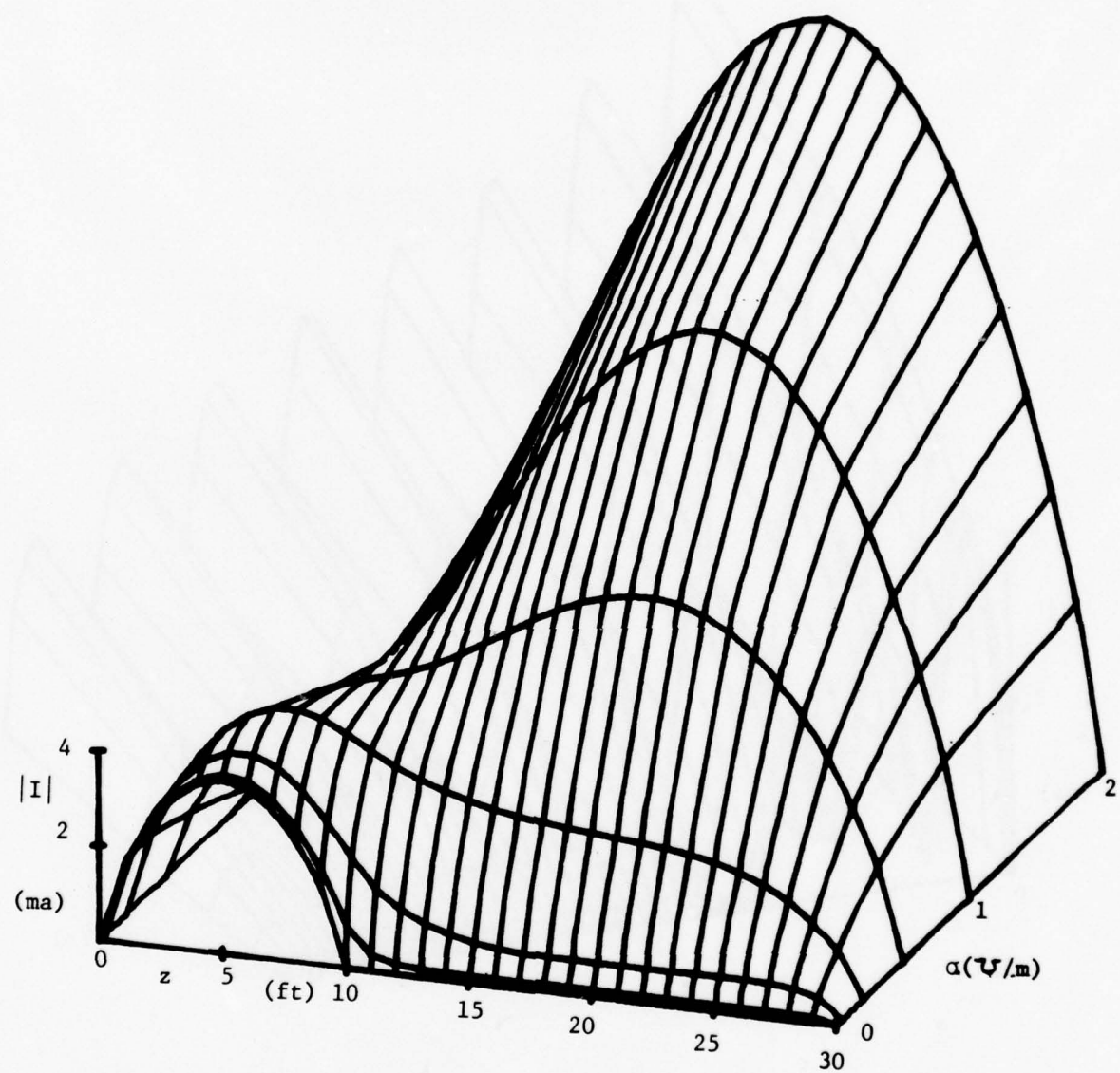


Fig. 25. Contour plot of $|I|$, $\theta_1 = 60^\circ$, $f = 20 \text{ MHz}$.

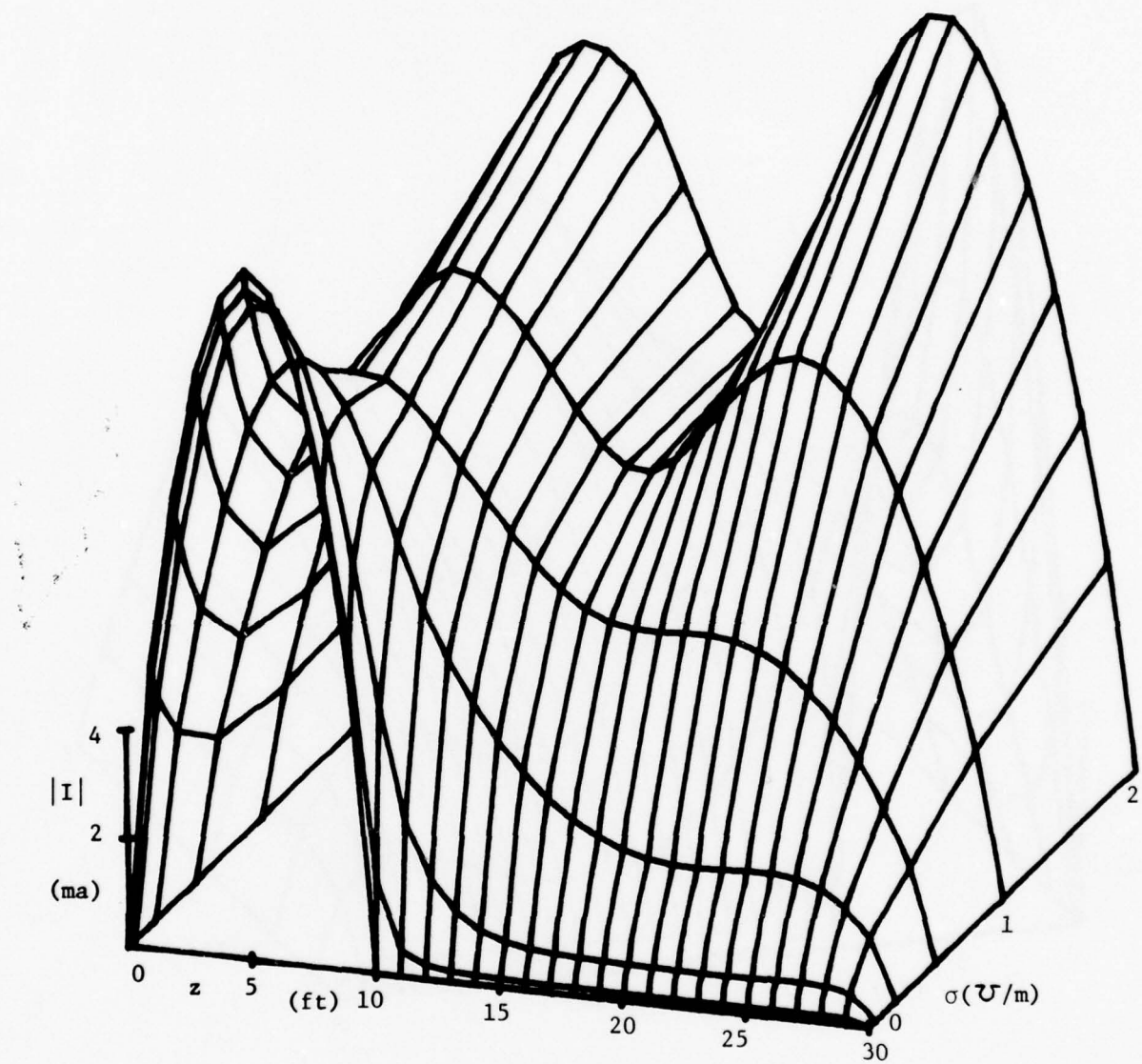


Fig. 26. Contour plot of $|I|$, $\theta_i = 60^\circ$, $f = 35$ MHz.

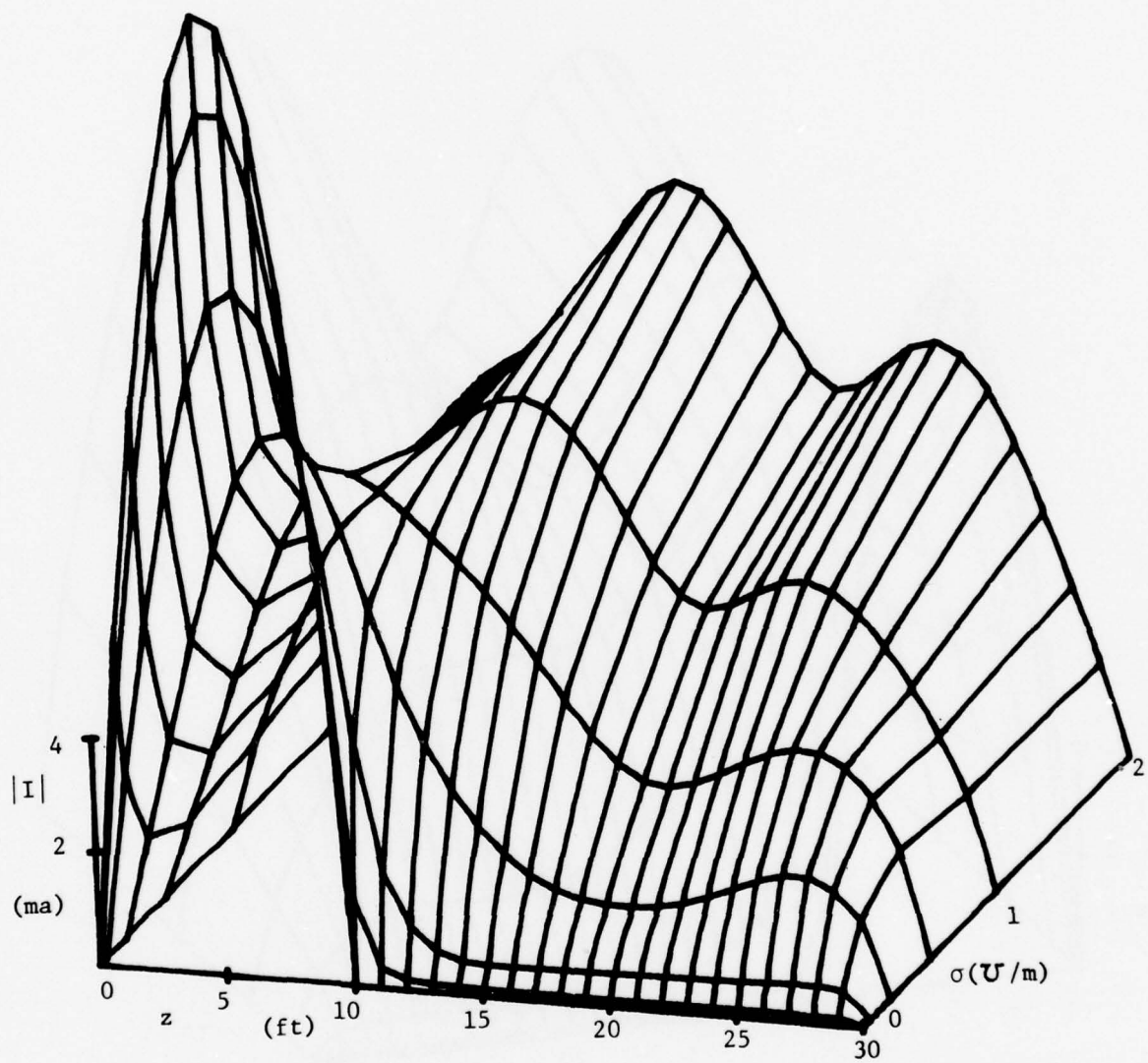


Fig. 27. Contour plot of $|I|$, $\theta_i = 60^\circ$, $f = 50$ MHz.

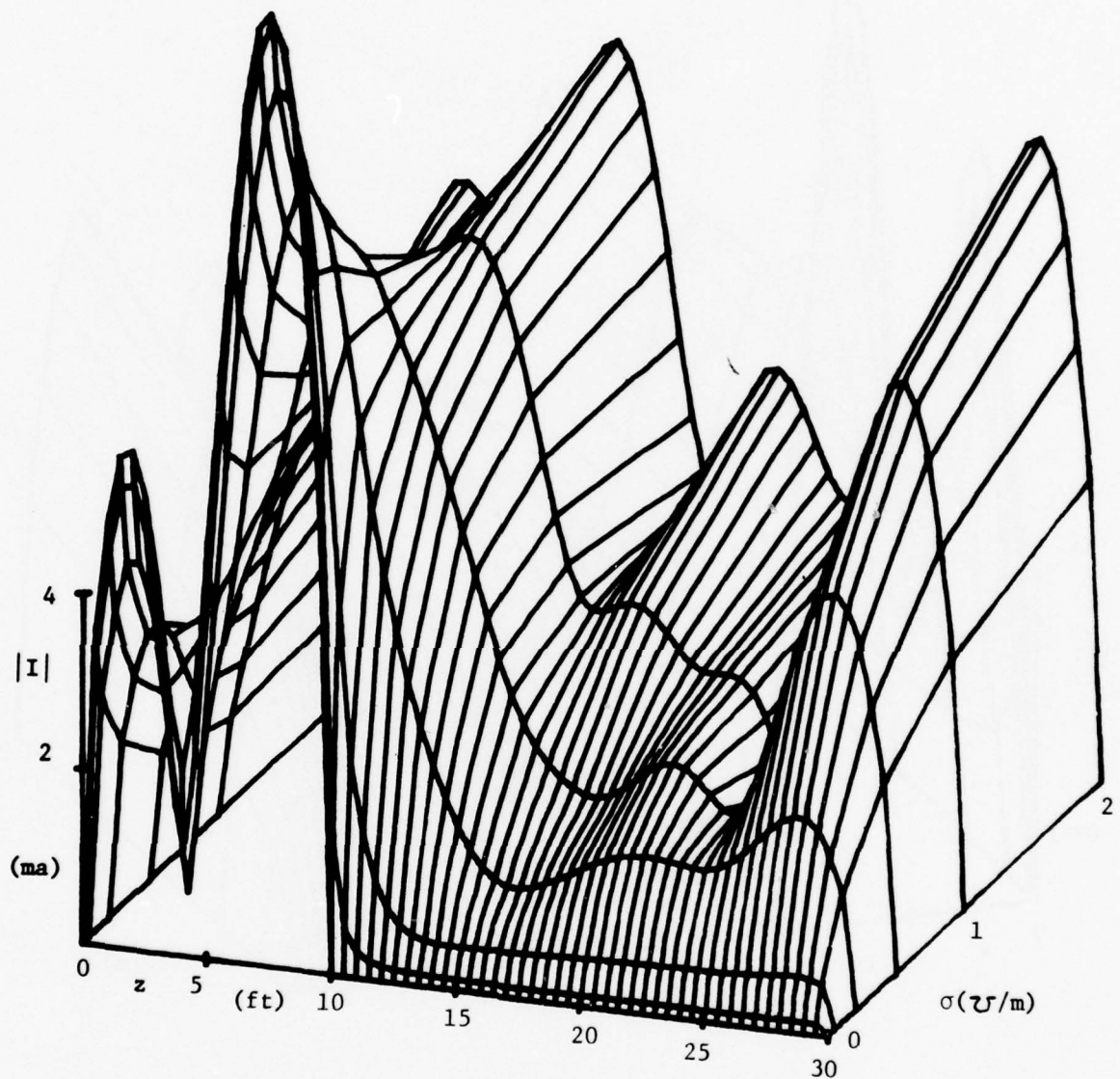


Fig. 28. Contour plot of $|I|$, $\theta_i = 60^\circ$, $f = 80$ MHz.

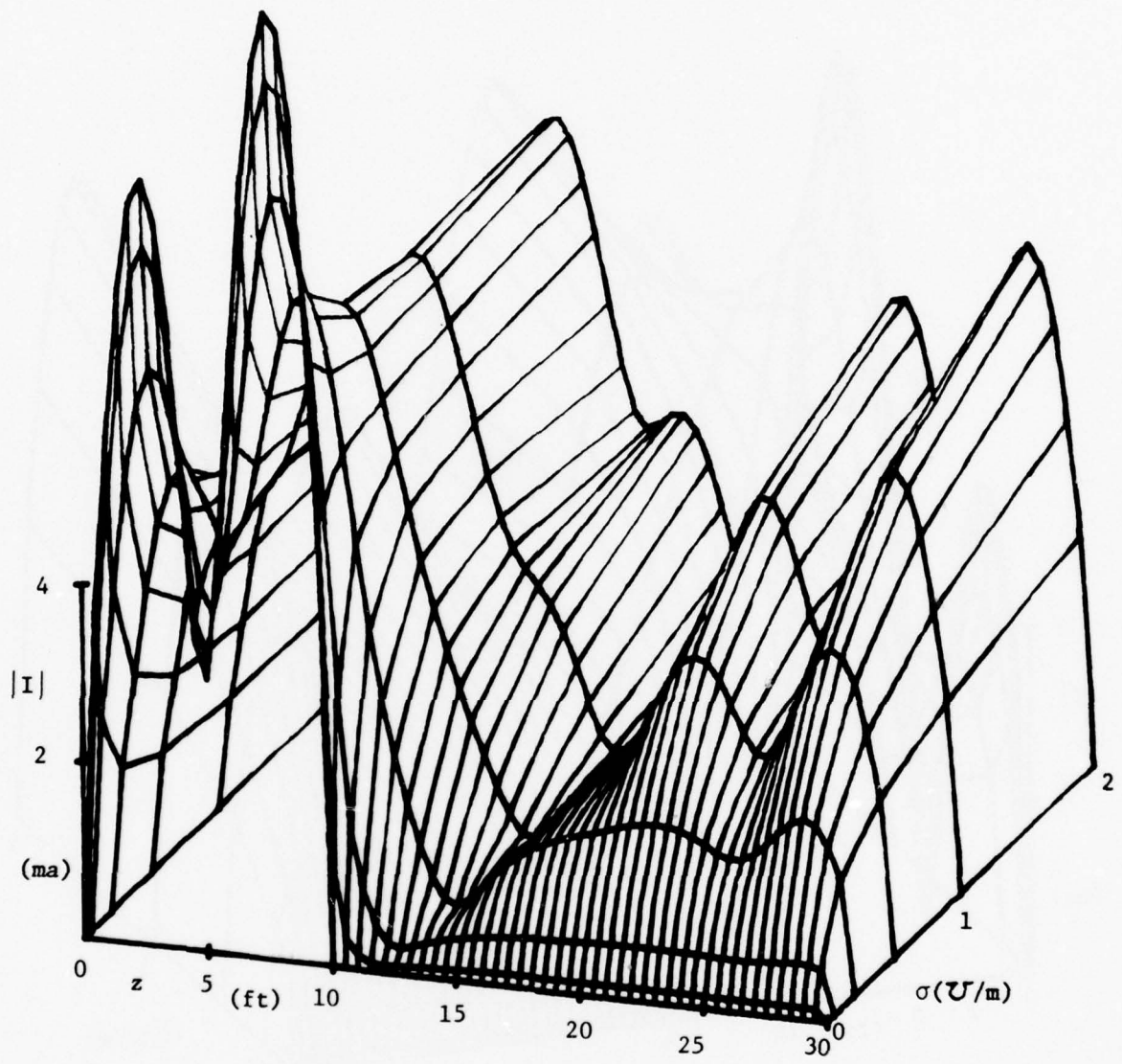


Fig. 29. Contour plot of $|I|$, $\theta_1 = 60^\circ$, $f = 100 \text{ MHz}$.

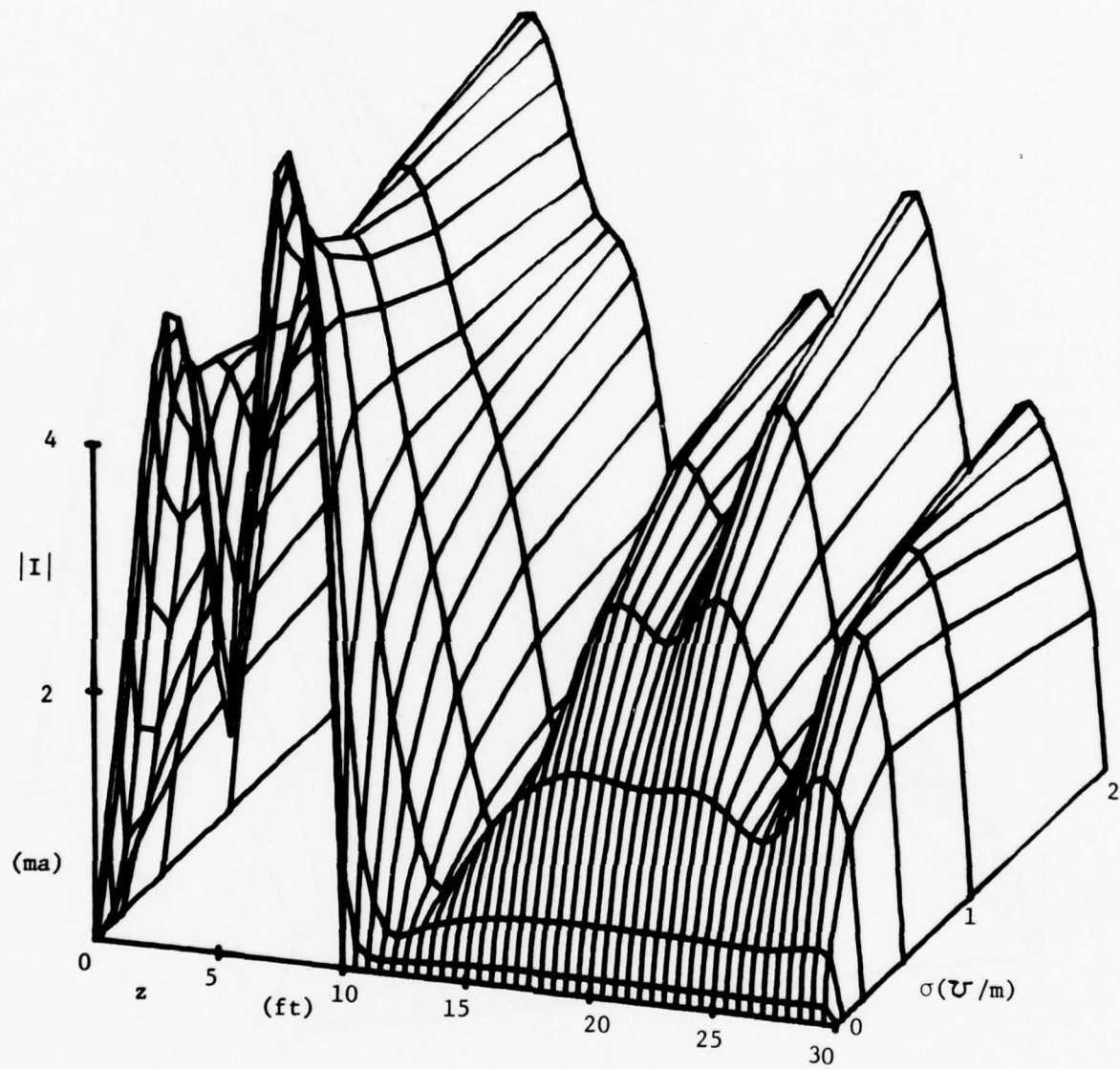


Fig. 30. Contour plot of $|I|$, $\theta_i = 60^\circ$, $f = 120$ MHz.

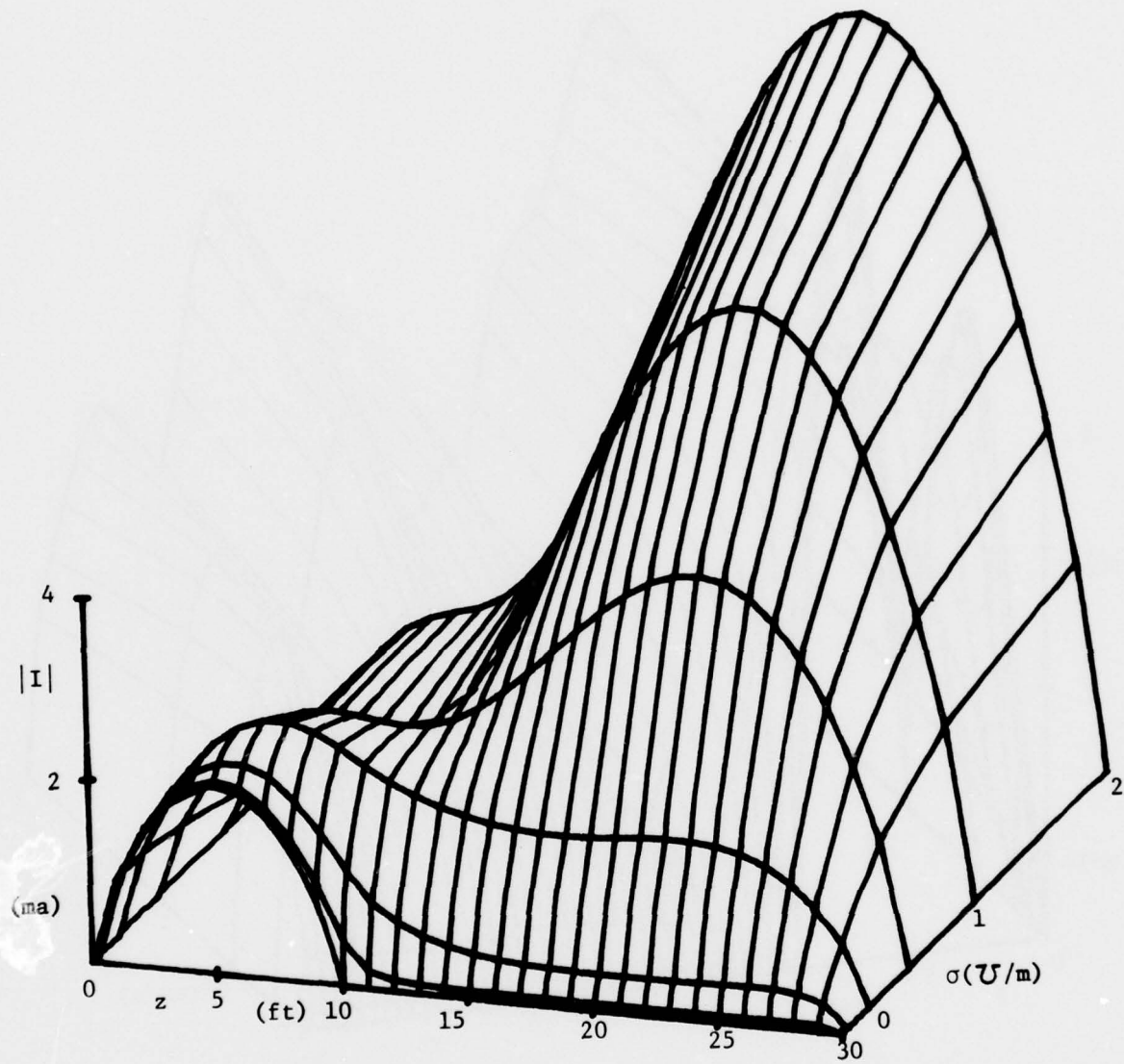


Fig. 31. Contour plot of $|I|$, $\theta_i = 30^\circ$, $f = 20$ MHz.

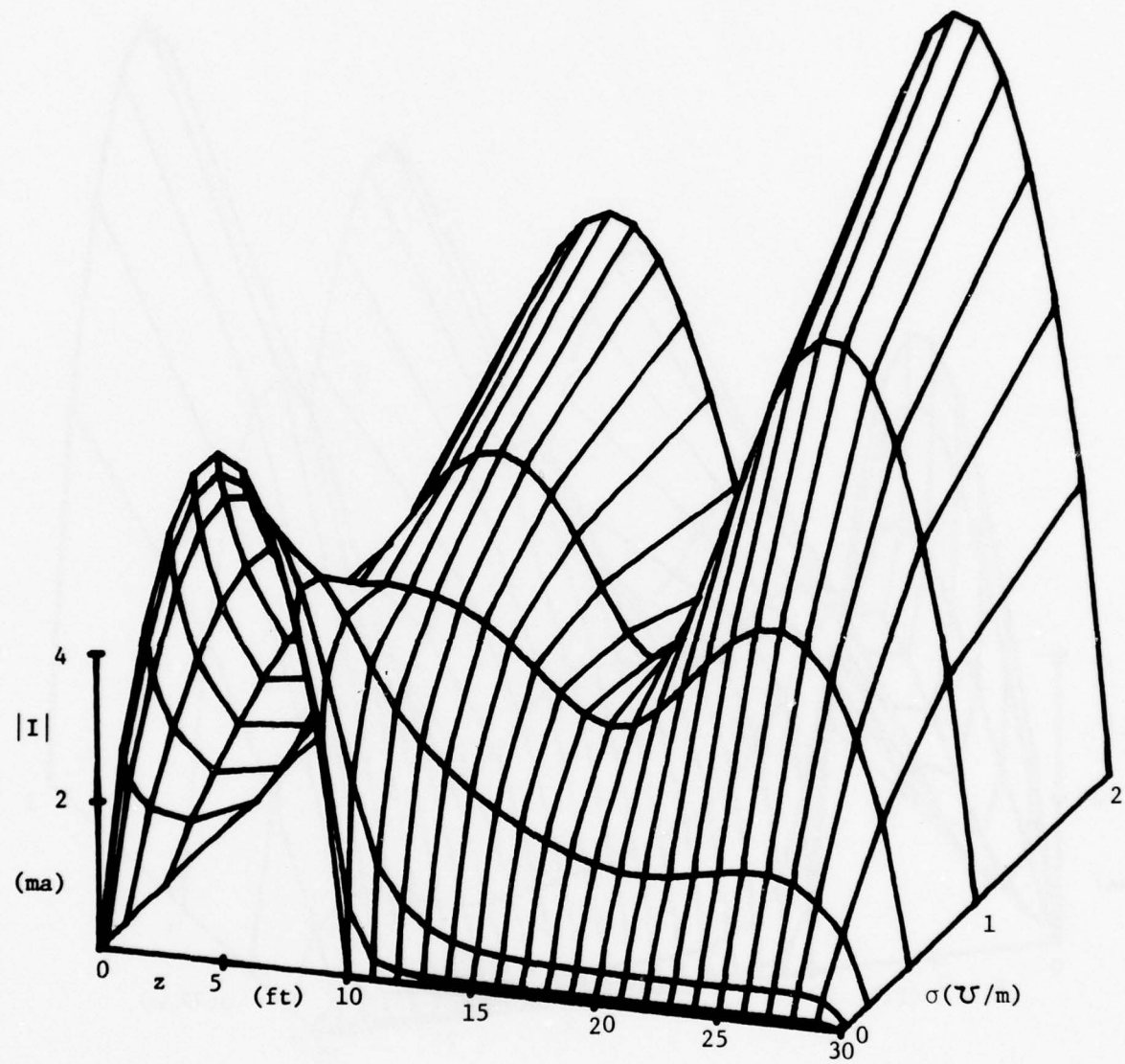


Fig. 32. Contour plot of $|I|$, $\theta_1 = 30^\circ$, $f = 35$ MHz.

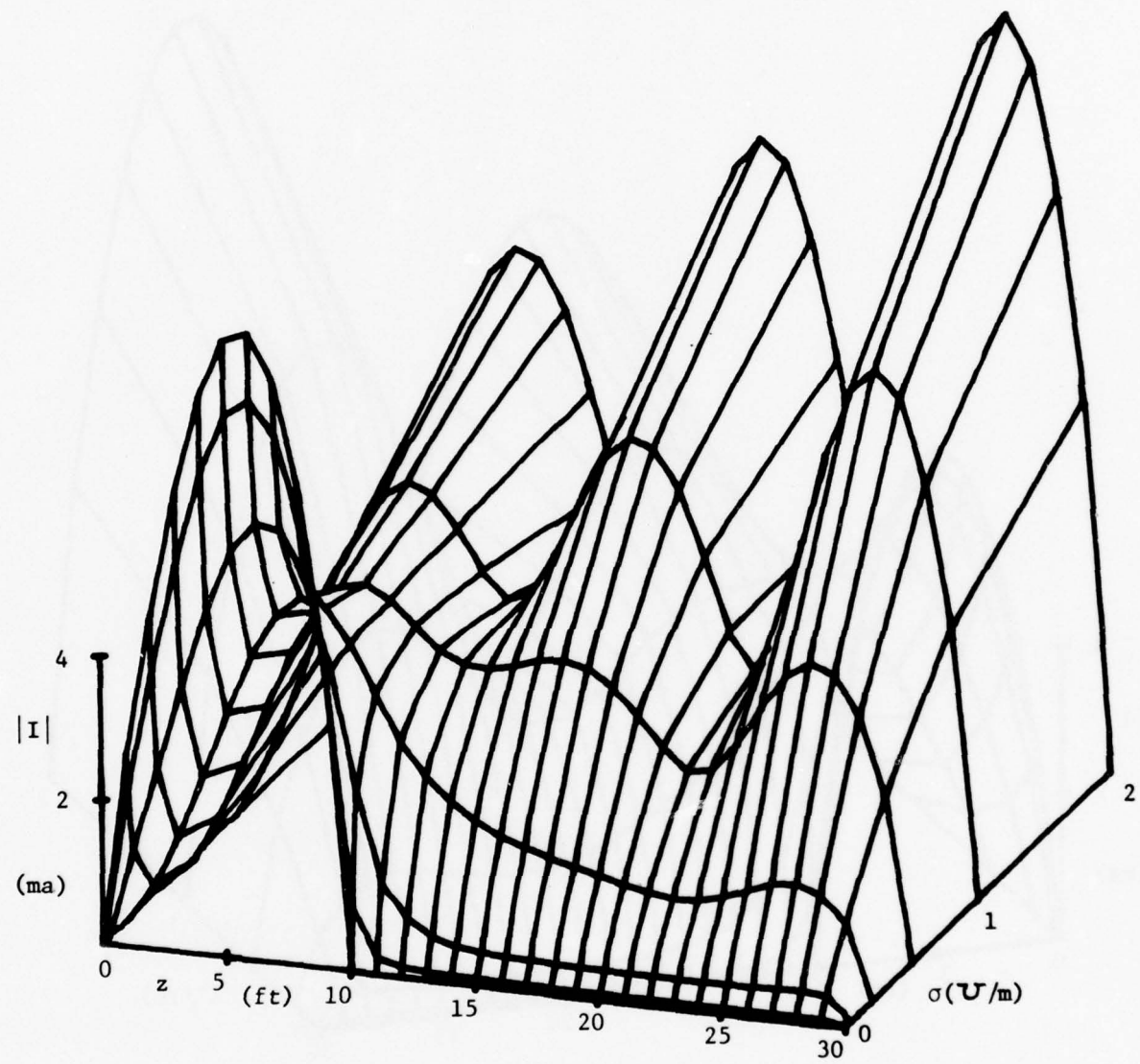


Fig. 33. Contour plot of $|I|$, $\theta_i = 30^\circ$, $f = 50 \text{ MHz}$.

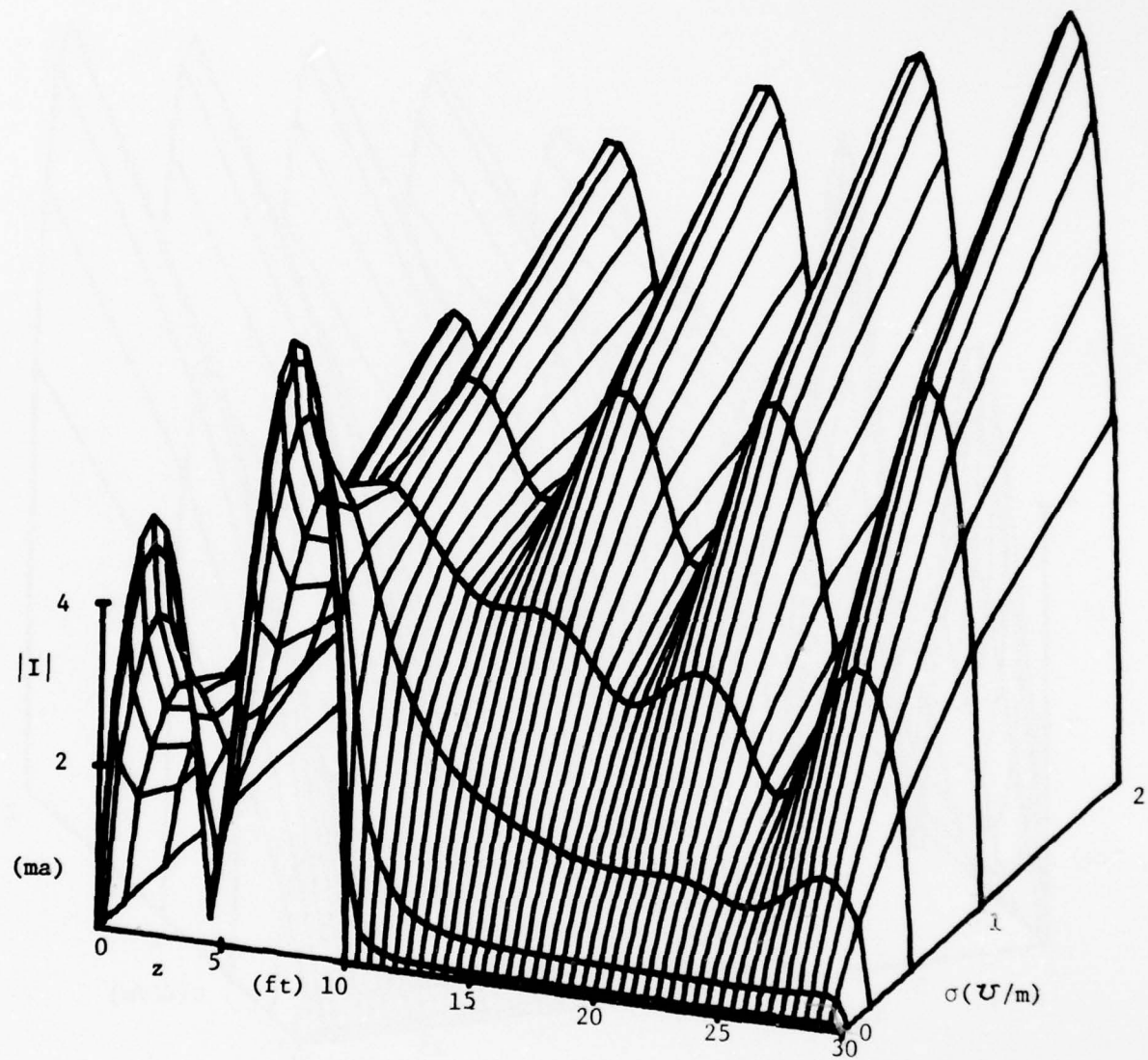


Fig. 34. Contour plot of $|I|$, $\theta_1 = 30^\circ$, $f = 80$ MHz.

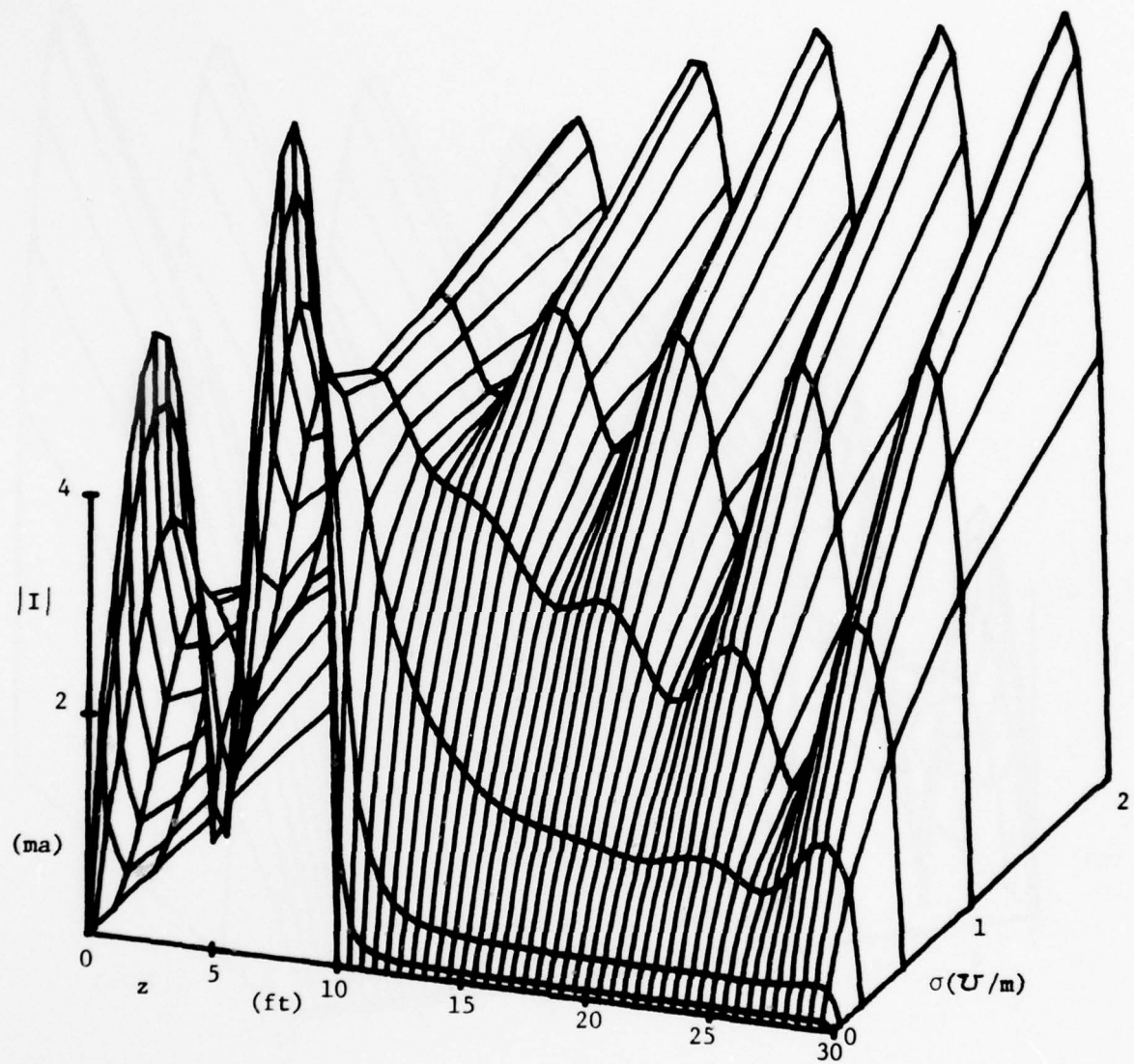


Fig. 35. Contour plot of $|I|$, $\theta_i = 30^\circ$, $f = 100$ MHz.

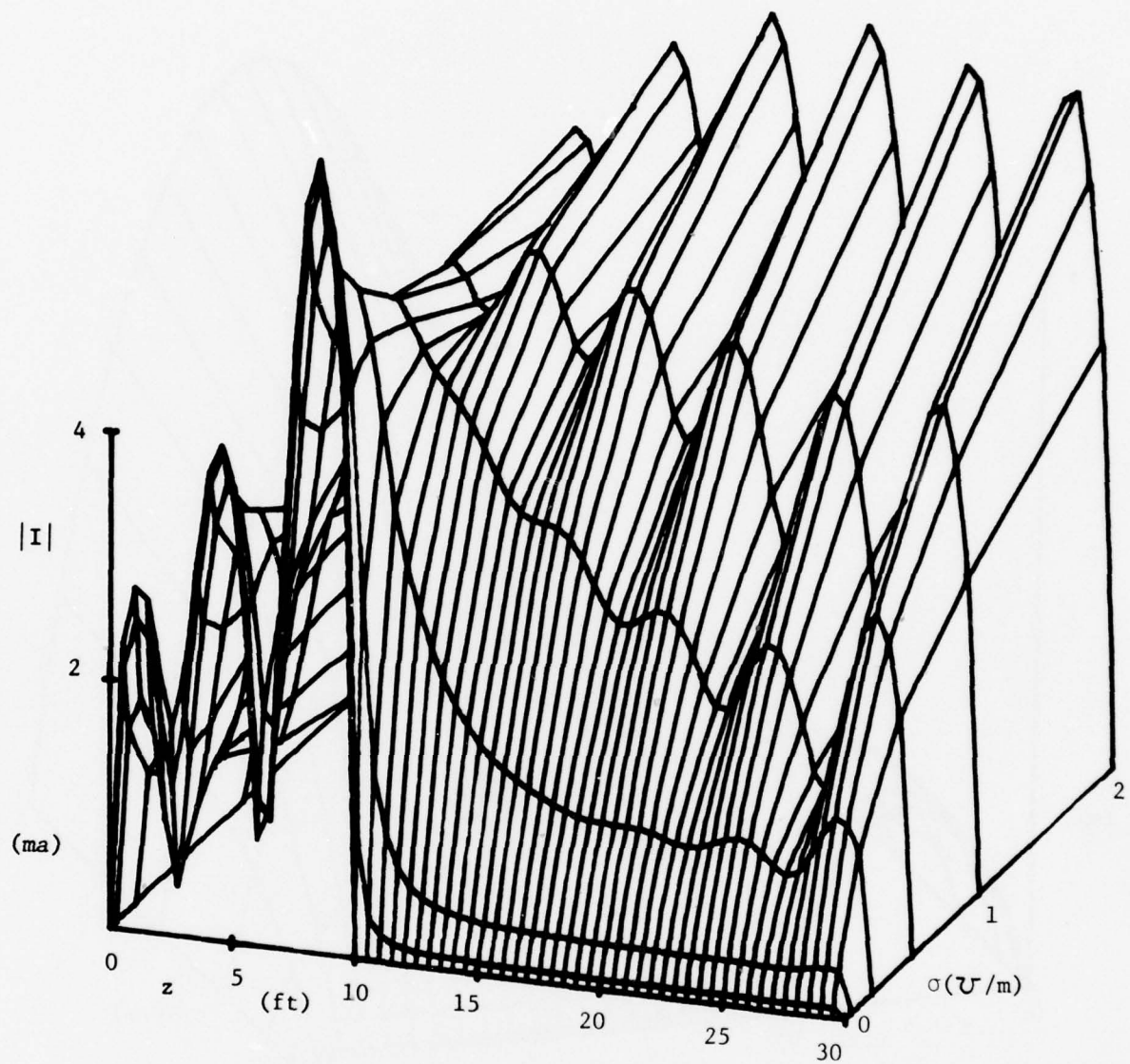


Fig. 36. Contour plot of $|I|$, $\theta_i = 30^\circ$, $f = 120$ MHz.

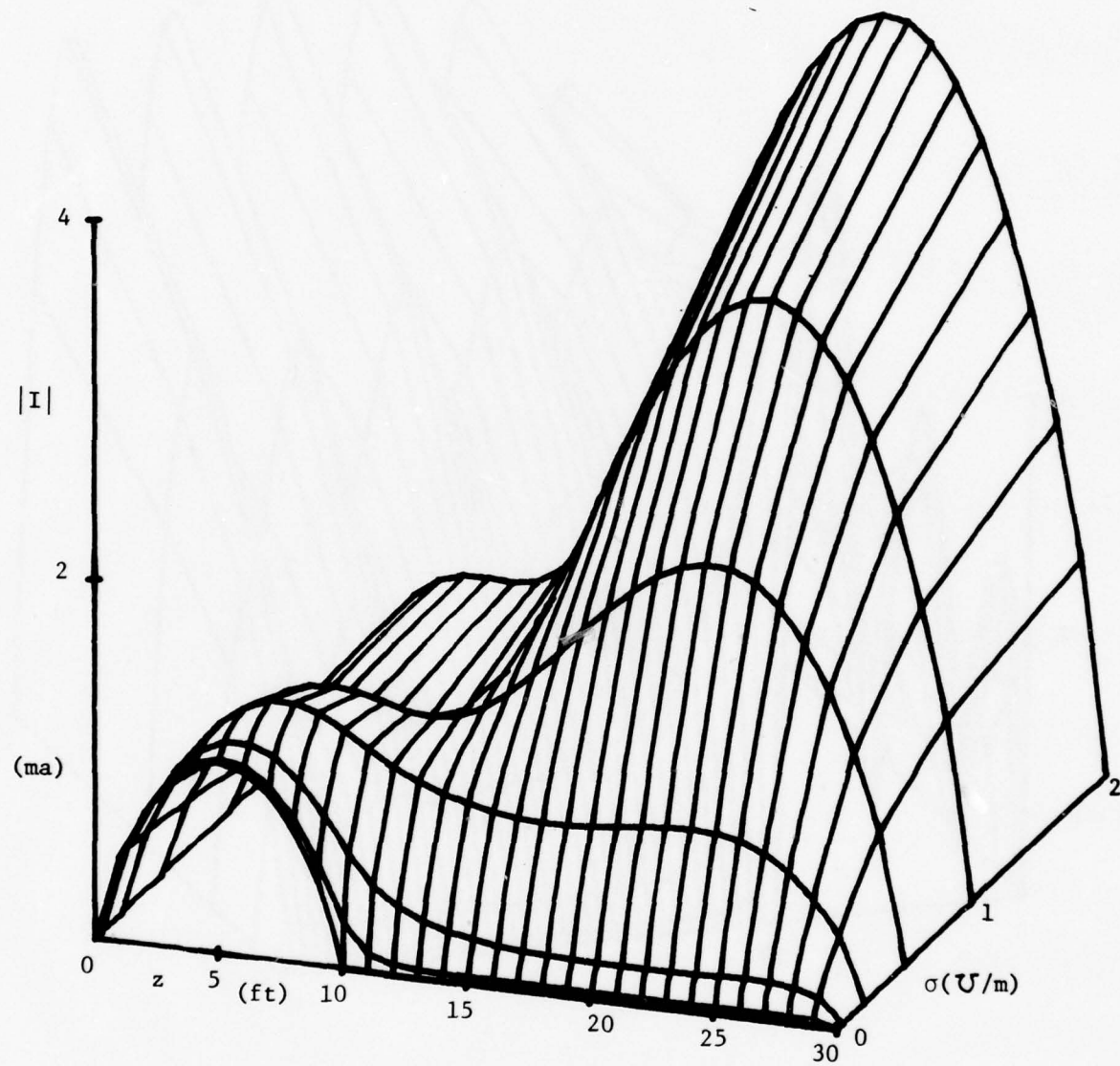


Fig. 37. Contour plot of $|I|$, $\theta_i = 15^\circ$, $f = 20$ MHz.

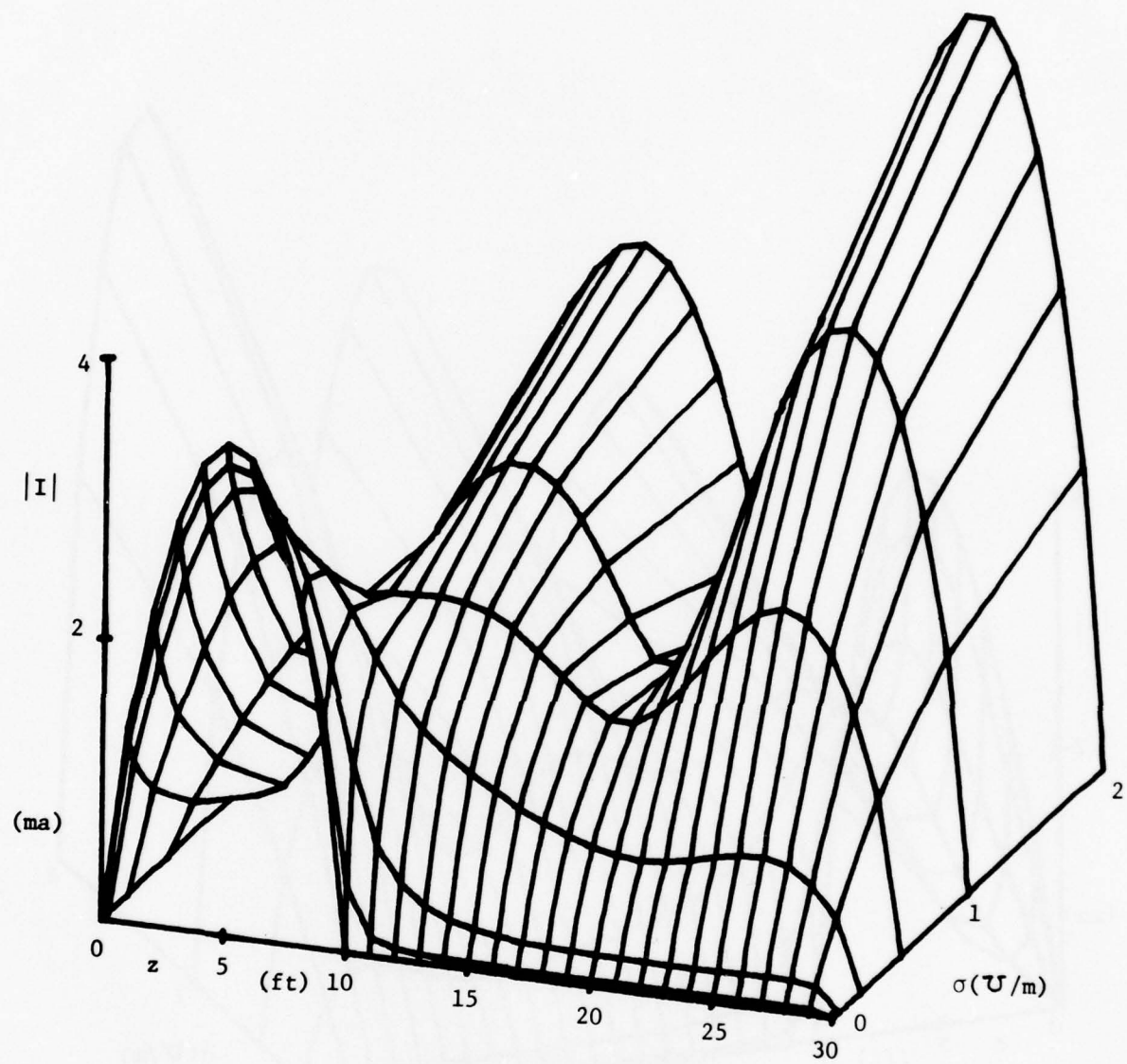


Fig. 38. Contour plot of $|I|$, $\theta_i = 15^\circ$, $f = 35 \text{ MHz}$.

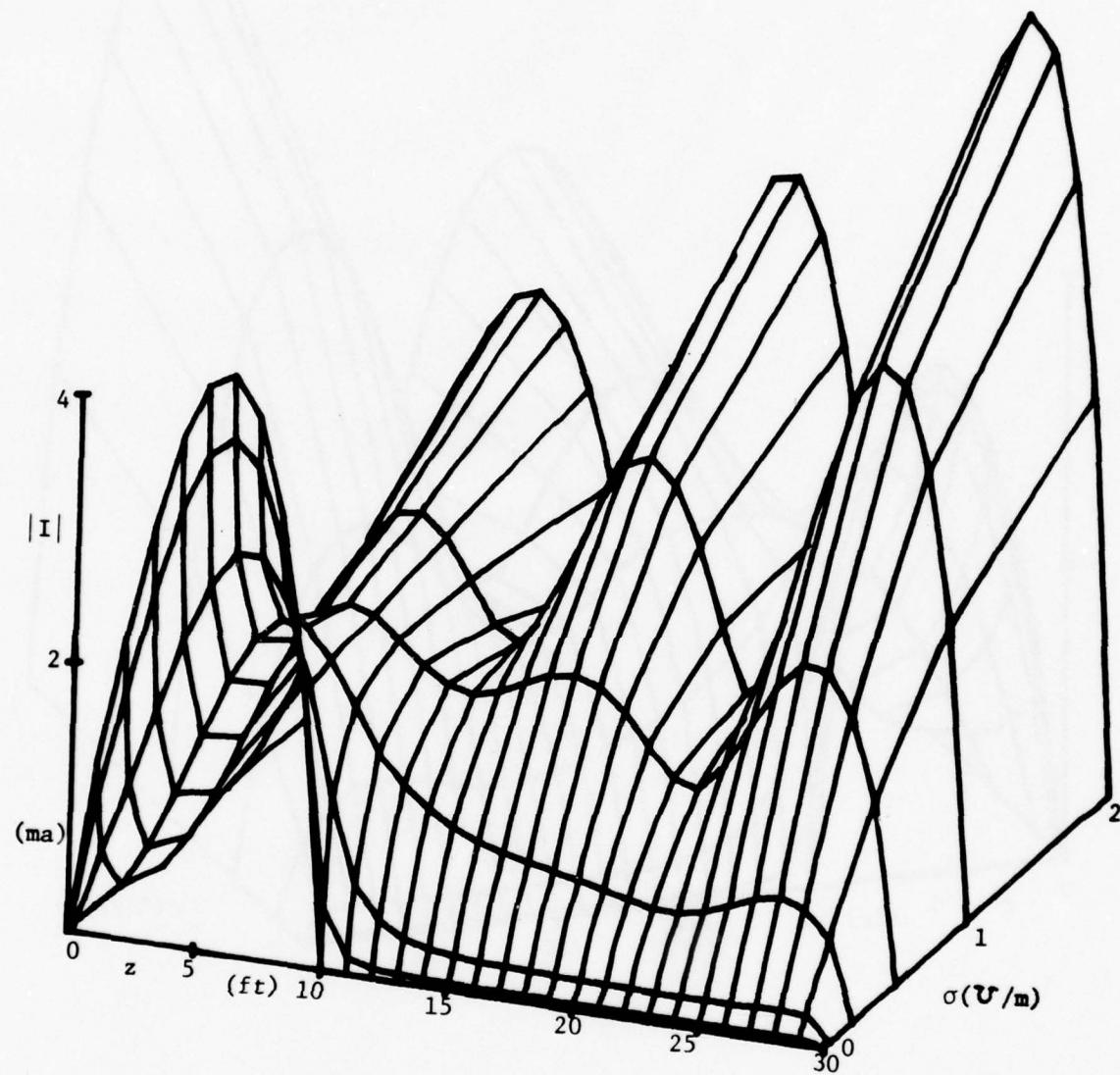


Fig. 39. Contour plot of $|I|$, $\theta_1 = 15^\circ$, $f = 50$ MHz.

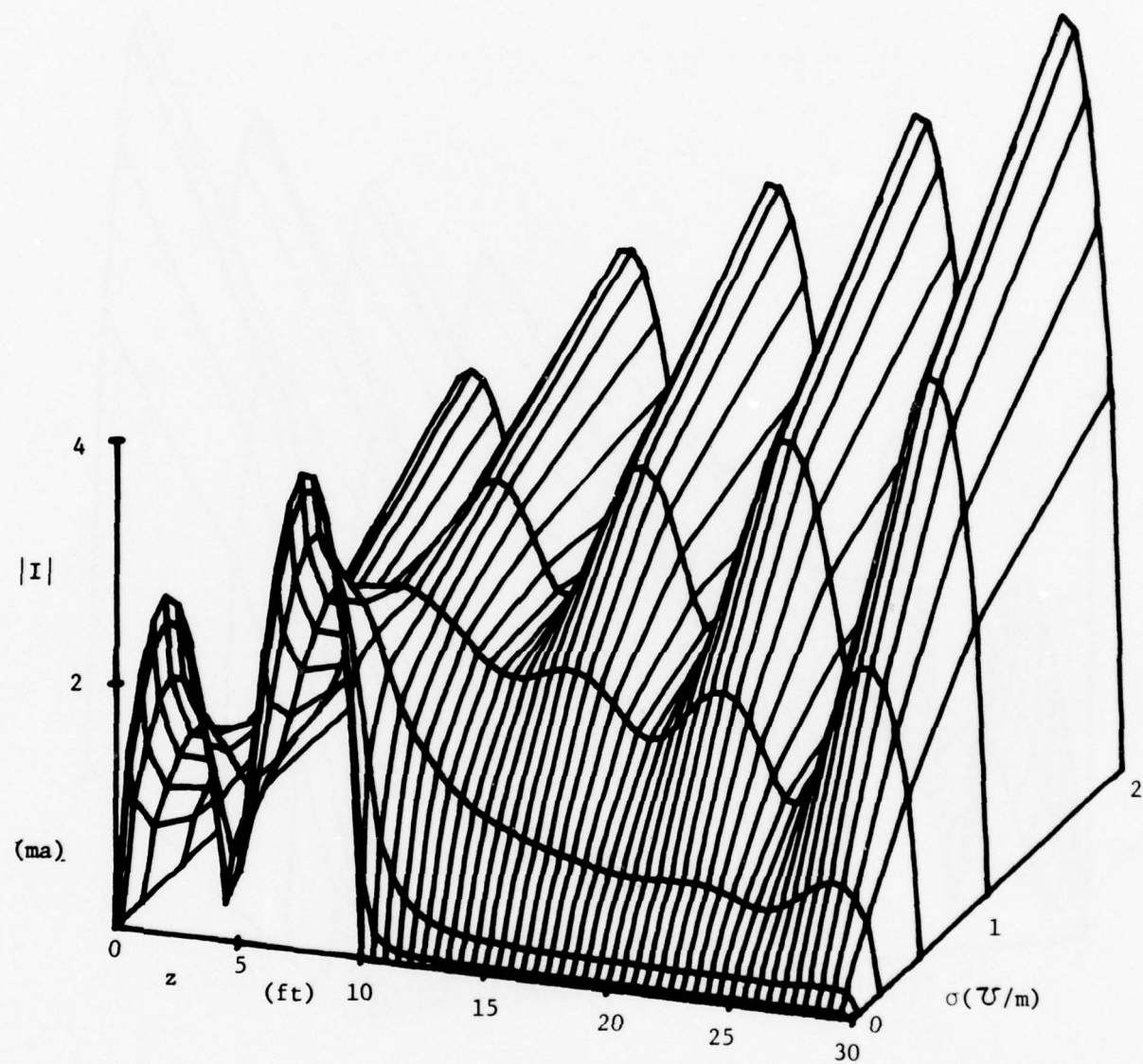


Fig. 40. Contour plot of $|I|$, $\theta_f = 15^\circ$, $f = 80$ MHz.

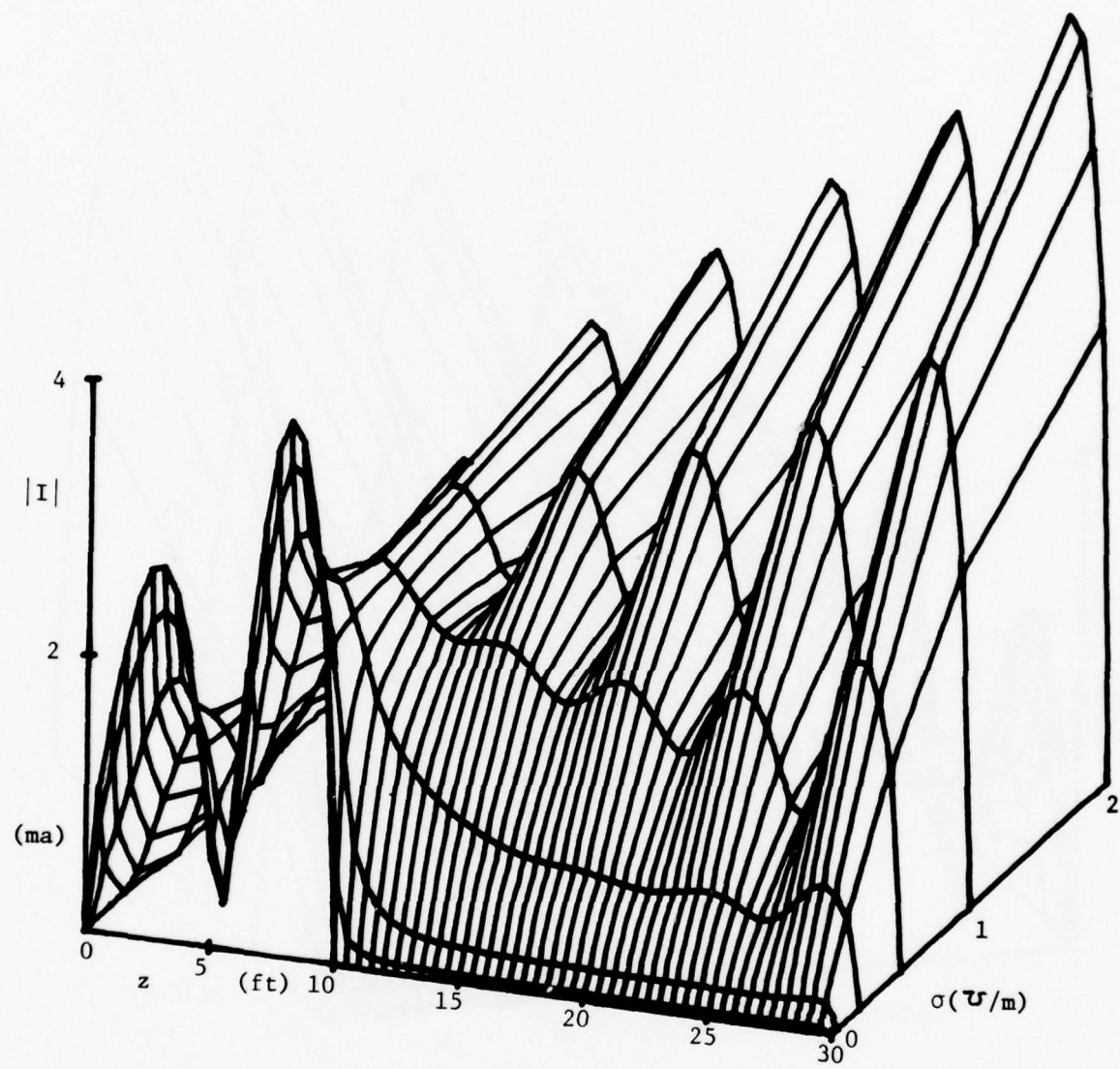


Fig. 41. Contour plot of $|I|$, $\theta_i = 15^\circ$, $f = 100$ MHz.

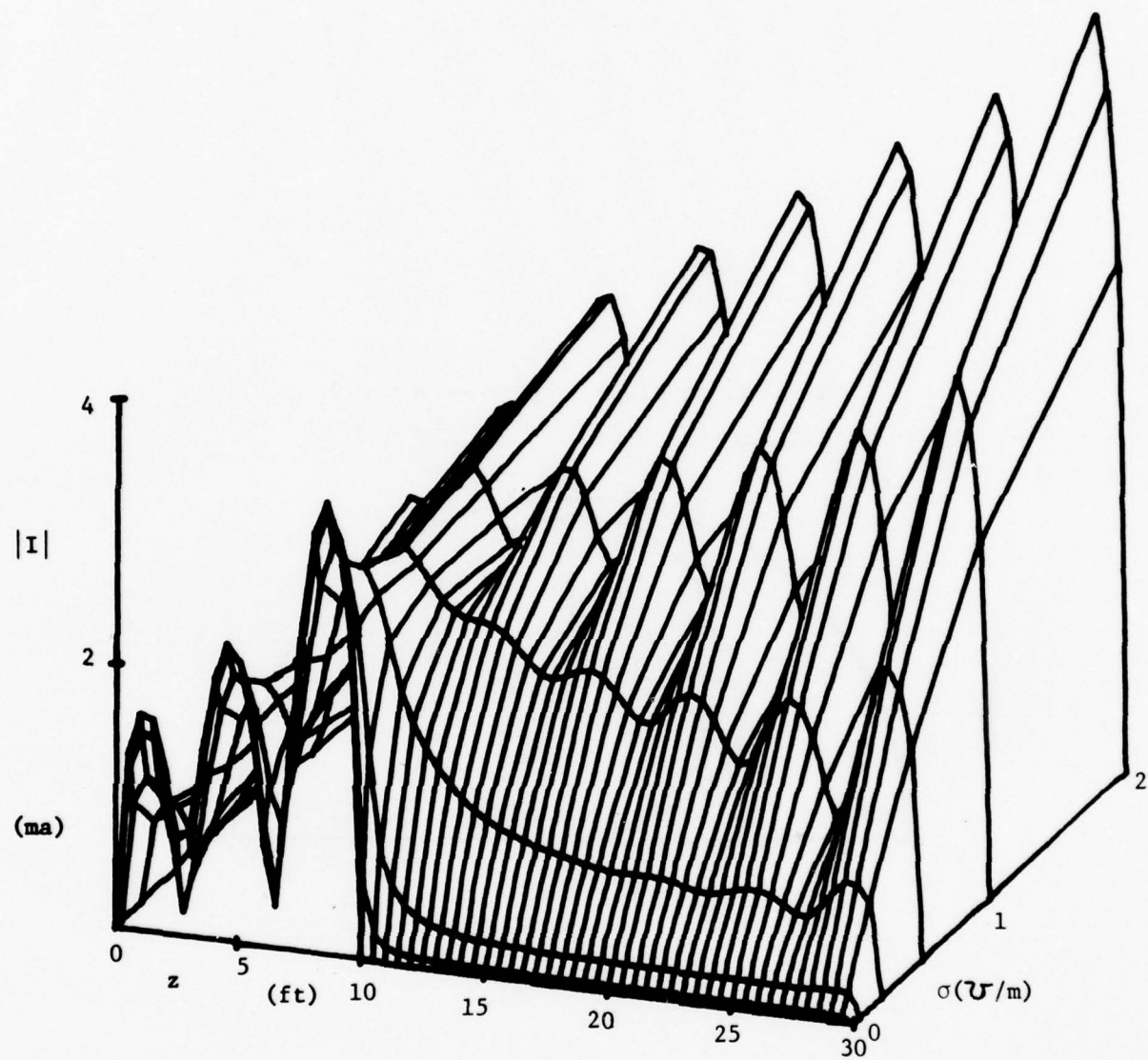


Fig. 42. Contour plot of $|I|$, $\theta_f = 15^\circ$, $f = 120$ MHz.

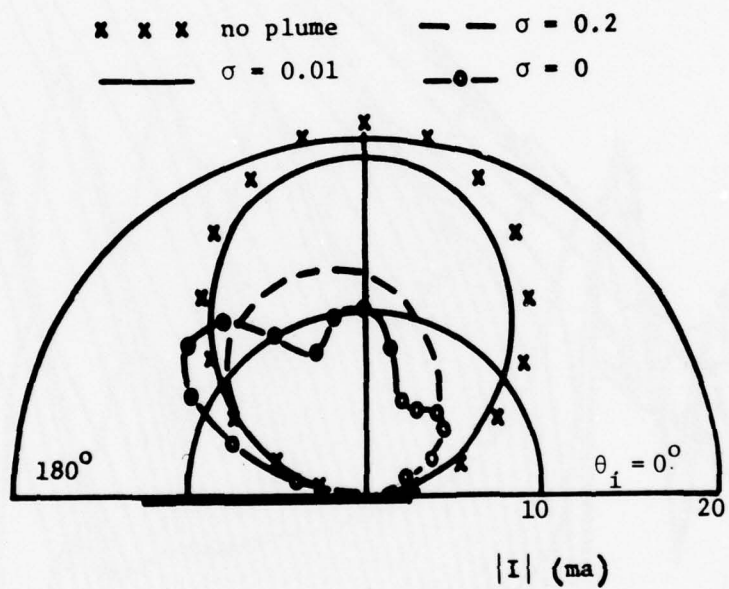


Fig. 43. Current magnitude $|I|$ at middle on a missile ($h = 10'$, $a = 2.5''$) with and without plume ($l = 20'$, $\sigma = 0.01$, 0.2 , and 1 u/m) as a function of incident angle θ_i ($f = 50 \text{ MHz}$).

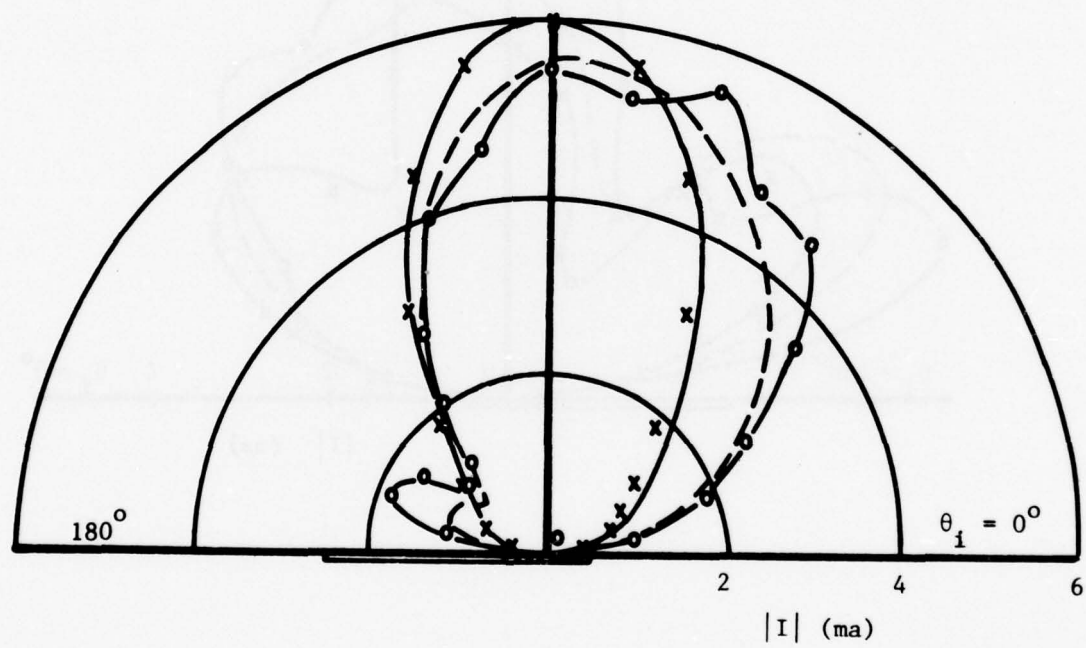


Fig. 44. $|I|$ at middle on the missile ($f = 100$ MHz).

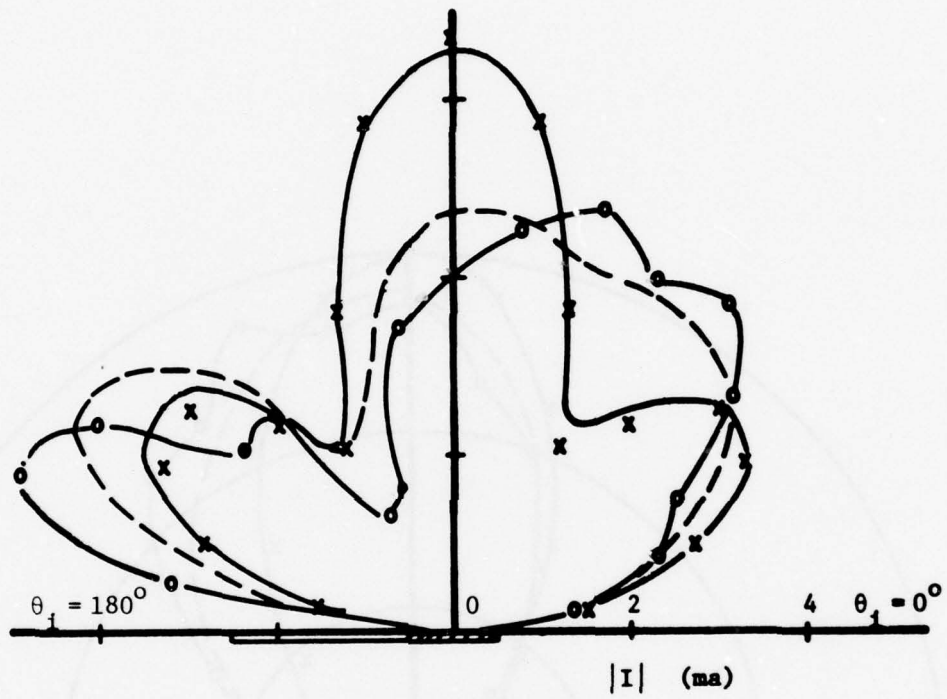


Fig. 45. $|I|$ at middle on the missile ($f = 120$ MHz).

nose of the missile are shown in Figs. 46-48. As can be seen, significant changes in current magnitude occur as the plume conductivity increases. These plots are also useful for assessing the coupling effect through apertures in the missile skin.

In summary, the effect of a homogeneous plume on the missile current distribution has been studied in this section using the thin-wire modeling and analysis. Extensive data show that minimal effects are observed if the plume conductivity σ is less than 0.01 v/m , but if $\sigma > 1 \text{ v/m}$, then significant differences are present as compared to the case of no plume present. If the missile is short with respect to the wavelength (e.g., for a 10' missile at 20 MHz) the plume usually enhances the current magnitude on the missile. However, if the missile is near or above resonance (e.g., for a 10' missile at frequencies larger than 35 MHz), the plume usually suppresses missile current for incident angles $\theta_i \leq 120^\circ$, while for $\theta_i \geq 150^\circ$ enhancement of current occurs again.

In addition to the above results, the thin wire code may also be used to assess the effect of an axially inhomogeneous plume with an axially varying conductivity as shown in Fig. 49. Note, however, that in the calculation of the equivalent impedance, the radius of the plume may differ from that of the missile, but in the analysis we assume the plume to have the same radius as the missile. Figs. 50 and 51 show the current magnitude on the missile with and without the inhomogeneous plume at $f = 100 \text{ MHz}$ for $\theta_i = 90^\circ$ and 165° , respectively. As in the homogeneous plume case, minimal effects are present if the maximum plume conductivity $\sigma_{\max} \leq 0.01 \text{ v/m}$. For higher plume conductivities and for wider plumes, more sophisticated models and analyses are needed as discussed in the following chapter.

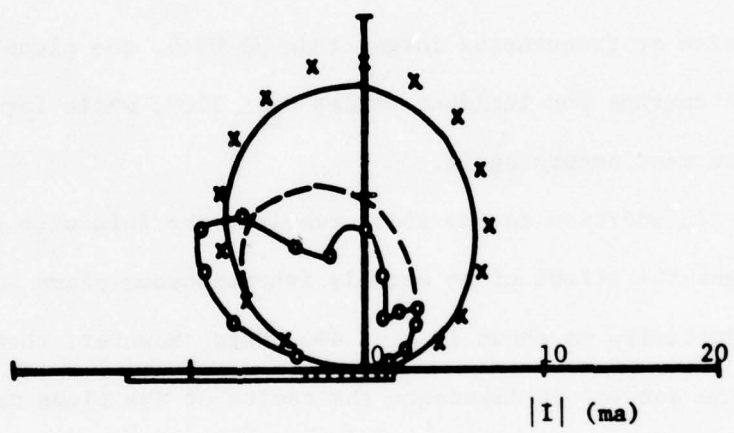


Fig. 46. $|I|$ at 3' from nose of the missile ($f = 50$ MHz).

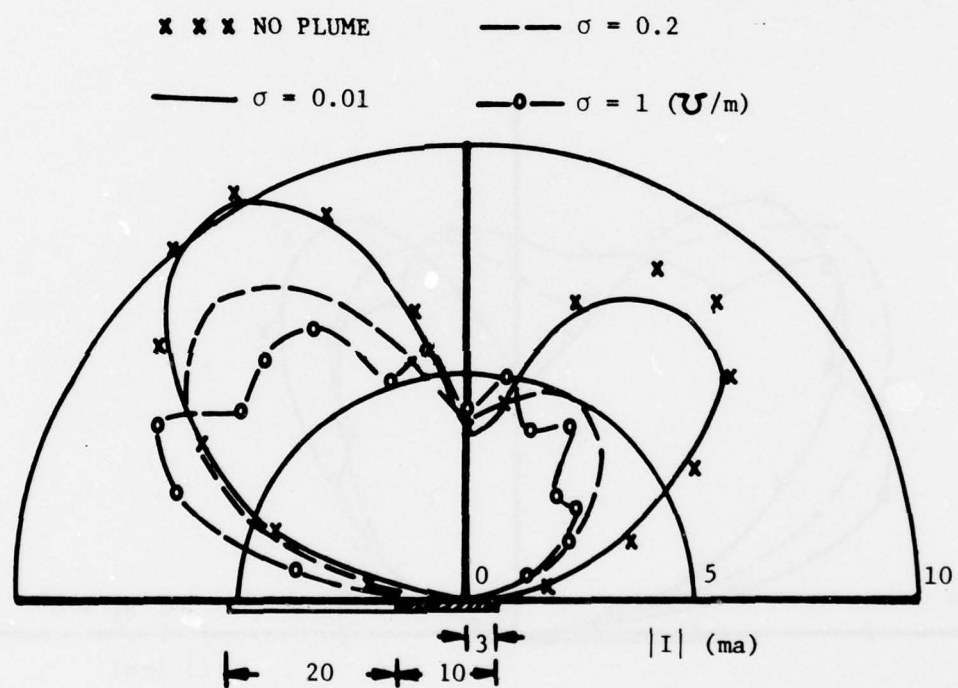


Fig. 47. $|I|$ at 3' from nose of the missile ($f = 100$ MHz).

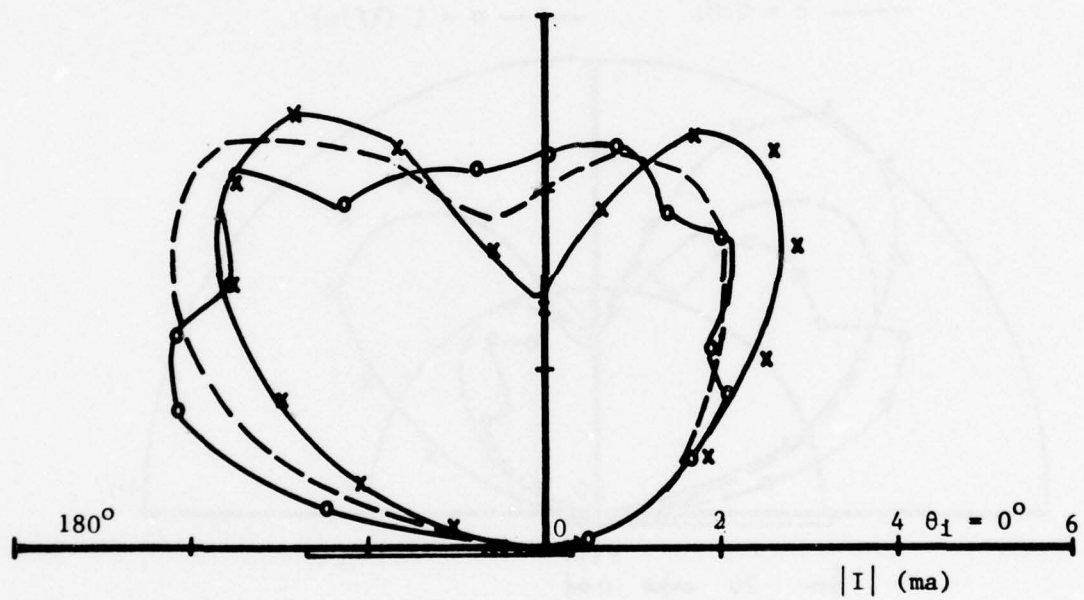


Fig. 48. $|I|$ at 3' from the nose of the missile ($f = 120$ MHz).

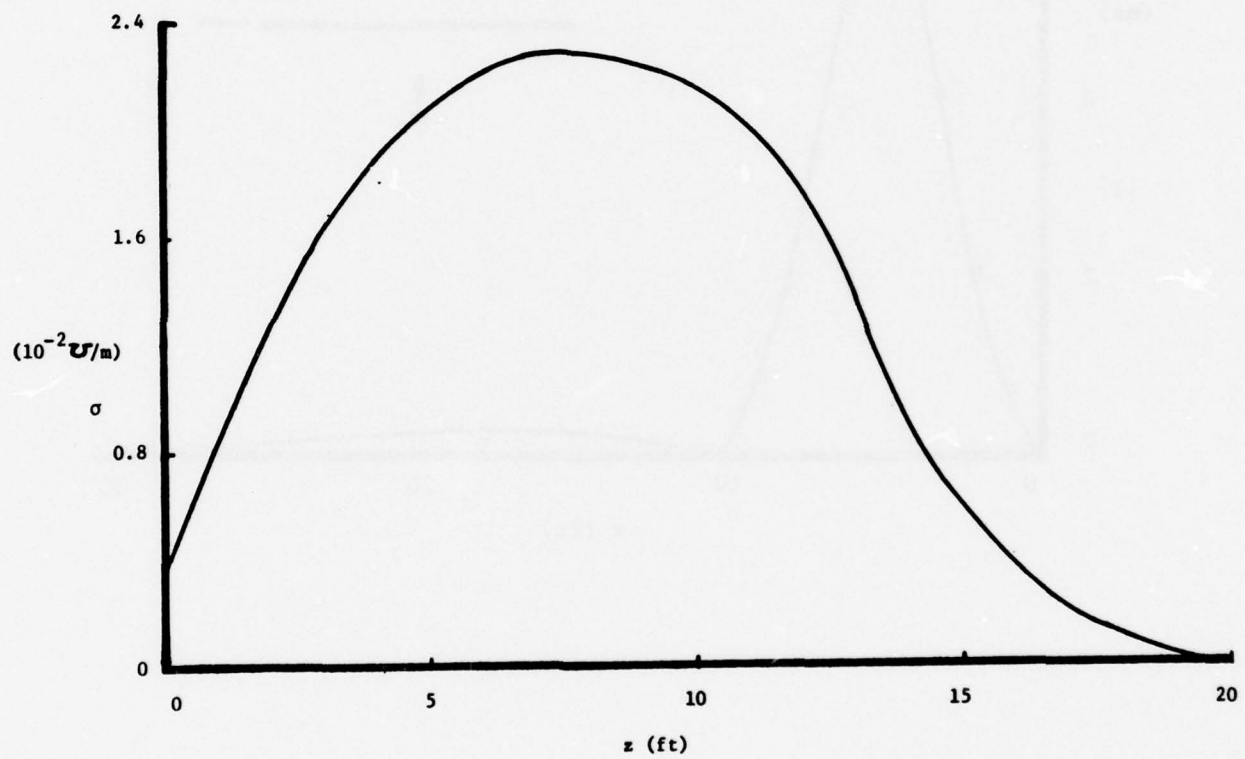


Fig. 49. Inhomogeneous plume conductivity profile along the plume axis.

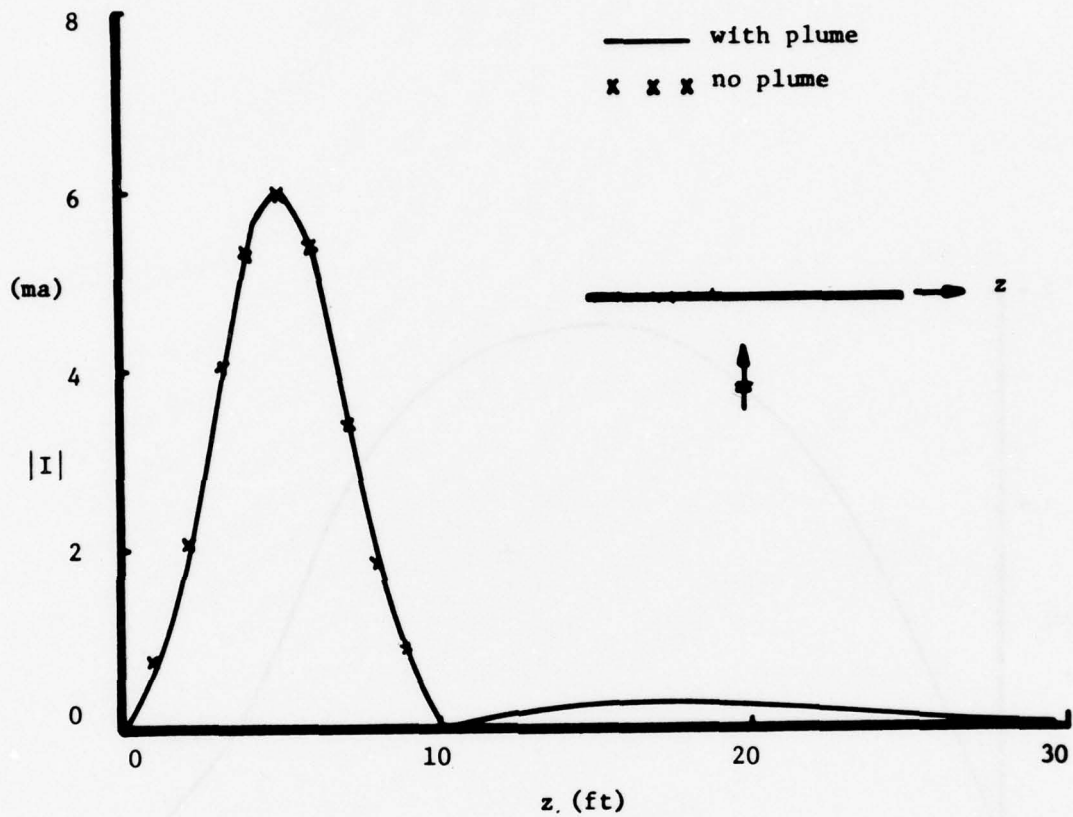


Fig. 50. Current amplitude $|I|$ on a missile ($h = 10'$, $a = 2.5''$) with and without the inhomogeneous plume of Fig. 49 (broadside incidence, $f = 100$ MHz).

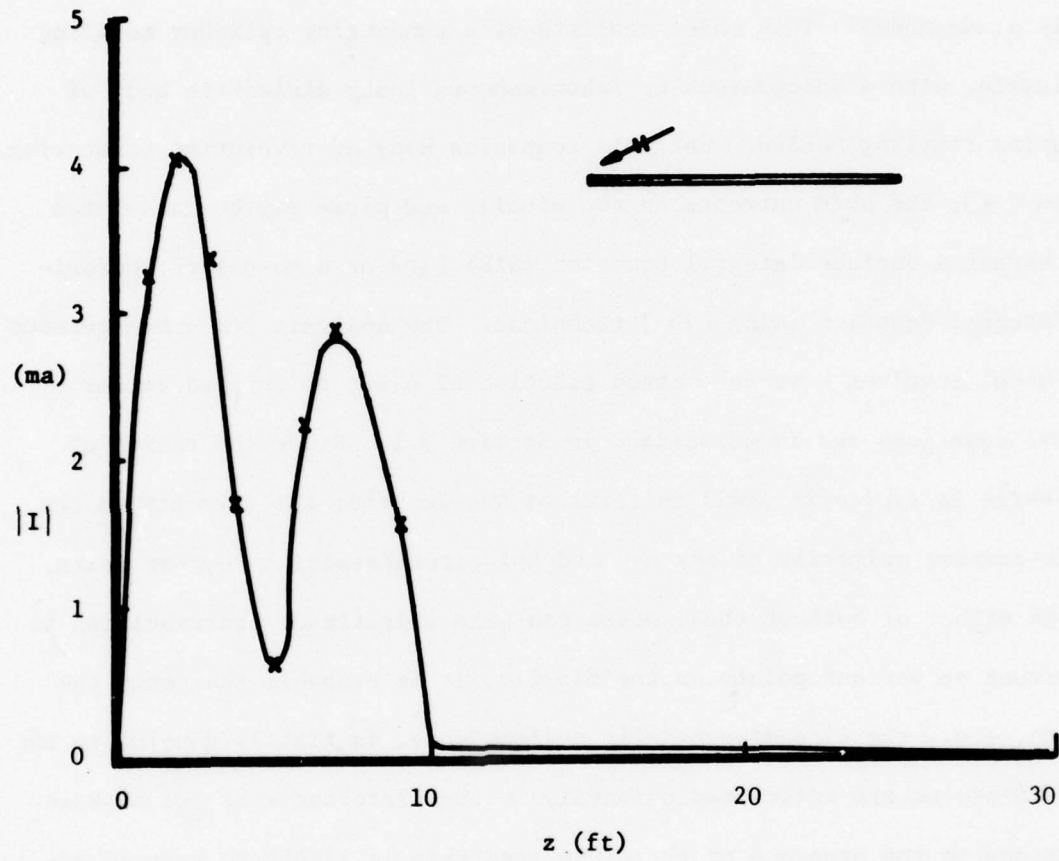


Fig. 51. $|I|$ on a missile with and without the inhomogeneous plume of Fig. 49 ($\theta_i = 165^\circ$, $f = 100$ MHz).

CHAPTER III
BODY OF REVOLUTION MODEL

The plume from a rocket exhaust tends to broaden away from the missile axis, particularly at higher altitudes, so that thin-wire plume models are often inadequate. Hence we consider in this chapter a more sophisticated missile/plume model. This model consists of a conducting cylinder modeling the missile, with a homogeneous or inhomogeneous lossy dielectric body of revolution trailing behind. For this composite body of revolution scattering problem [9], the skin currents on the missile and plume may be calculated using either a Surface Integral Equation (SIE) [10] or a so-called Approximate Integral Equation (AIE) [18] technique. The analysis for a homogeneous plume model involves a moment method solution of a set of coupled vector integral equations and is summarized in Section 3.1. Since the radius of the missile is typically small in terms of wavelengths, the currents on the missile consist primarily of the $n=0$ and $n=1$ circumferential Fourier modes. Although either or both of these modes can make significant contributions to the current at various points on the missile, it is probable that only the $n=0$ mode, i.e., the circumferentially uniform mode, is tightly coupled to the plume. Since we are interested primarily in the disturbance of the missile current due to the presence of the plume, and this is likely to have no effect on the $n=1$ mode, we consider here only the circumferentially uniform mode. In Section 3.2 the scattering of an inhomogeneous plume model is considered using the Approximate Integral Equation (AIE) approach. Numerical results obtained using these methods are presented in Section 3.3. The accuracy and applicability of the AIE method is also discussed.

3.1. Surface Integral Equation (SIE) Method

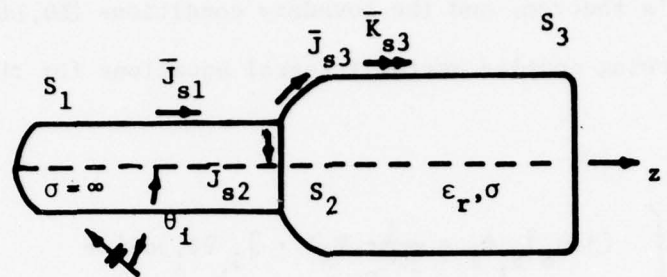
Consider the composite metal-lossy dielectric body of revolution (BOR) model depicted in Fig. 52. The conducting portion represents the missile and the dielectric portion represents the homogeneous plume. From Maxwell's Equations, Green's theorem, and the boundary conditions [10,11] one readily obtains the following coupled vector integral equations for the base-contact BOR(I) model:

$$\bar{E}^i(\bar{r}) = \frac{1}{4\pi} \left\{ \int_{S_1} [j\omega\mu_0 \bar{J}_{S_1} \Phi_1 - \frac{1}{j\omega\epsilon_0} \nabla_{S'} \cdot \bar{J}_{S_1} \nabla \Phi_1] dS' + \int_{S_3} [j\omega\mu_0 \bar{J}_{S_3} \Phi_1 - \frac{1}{j\omega\epsilon_0} \nabla_{S'} \cdot \bar{J}_{S_3} \nabla \Phi_1 - \bar{K}_{S_3} \times \nabla \Phi_1] dS' \right\} , \quad (7)$$

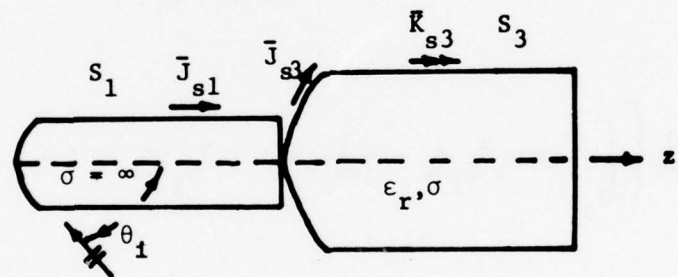
for $\bar{r} \in S_1$,

$$0 = \frac{1}{4\pi} \left\{ \int_{S_2} [j\omega\mu_0 \bar{J}_{S_2} \Phi_2 - \frac{1}{j\omega\epsilon_2} \nabla_{S'} \cdot \bar{J}_{S_2} \nabla \Phi_2] dS' + \int_{S_3} [j\omega\mu_0 \bar{J}_{S_3} \Phi_2 - \frac{1}{j\omega\epsilon_2} \nabla_{S'} \cdot \bar{J}_{S_3} \nabla \Phi_2 - \bar{K}_{S_3} \times \nabla \Phi_2] dS' \right\} , \quad (8)$$

for $\bar{r} \in S_2$,



(a) base-contact B.O.R. (I)



(b) point contact B.O.R. (II)

Figure 52. Composite body of revolution models of missile with homogeneous plume.

$$\begin{aligned}
\bar{E}^1(\bar{r}) = \frac{1}{4\pi} \left\{ & \int_{S_1} [j\omega\mu_0 \bar{J}_{S_1} \Phi_1 - \frac{1}{j\omega\epsilon_0} \nabla_{S'} \cdot \bar{J}_{S_1} \nabla \Phi_1] dS' + \right. \\
& \int_{S_2} [j\omega\mu_0 \bar{J}_{S_2} \Phi_2 - \frac{1}{j\omega\epsilon_2} \nabla_{S'} \cdot \bar{J}_{S_2} \nabla \Phi_2] dS' + \\
& \int_{S_3} [j\omega\mu_0 \bar{J}_{S_3} (\Phi_1 + \Phi_2) - \frac{1}{j\omega} \nabla_{S'} \cdot \bar{J}_{S_3} \nabla \left(\frac{\Phi_1}{\epsilon_0} + \frac{\Phi_2}{\epsilon_2} \right) \\
& \left. - \bar{K}_{S_3} \times \nabla(\Phi_1 + \Phi_2) \right] dS' \} \quad , \tag{9}
\end{aligned}$$

and

$$\begin{aligned}
\bar{H}^1(\bar{r}) = \frac{1}{4\pi} \left\{ & \int_{S_1} \bar{J}_{S_1} \times \nabla \Phi_1 dS' + \int_{S_2} \bar{J}_{S_2} \times \nabla \Phi_2 dS' + \right. \\
& \int_{S_3} [\bar{J}_{S_3} \times \nabla(\Phi_1 + \Phi_2) + j\omega \bar{K}_{S_3} (\epsilon_0 \Phi_1 + \epsilon_2 \Phi_2) \\
& \left. - \frac{1}{j\omega\mu_0} \nabla_{S'} \cdot \bar{K}_{S_3} \nabla(\Phi_1 + \Phi_2)] dS' \} \quad , \\
& \text{for } \bar{r} \in S_3 \tag{10}
\end{aligned}$$

The above integral equations are implicitly valid for tangential components only, and may also be derived via the surface equivalence principle. \bar{J}_{S_1} and \bar{J}_{S_2} are the unknown electric current densities on the air-conductor interface S_1 and the conductor-dielectric interface S_2 , respectively. \bar{J}_{S_3}

and \bar{K}_{S_3} are the unknown electric and magnetic current densities on the air-dielectric interface S_3 . The boundary conditions also require that \bar{K}_{S_3} vanishes and \bar{J}_{S_1} , \bar{J}_{S_2} and \bar{J}_{S_3} are equal at the junction of the air, conductor and dielectric. $\bar{E}^i(\bar{r})$ and $\bar{H}^i(\bar{r})$ are the incident electric and magnetic fields and $\Phi_2 = \exp(-jk_2|\bar{r}-\bar{r}'|)/|\bar{r}-\bar{r}'|$ and $\Phi_1 = \exp(-jk_0|\bar{r}-\bar{r}'|)/|\bar{r}-\bar{r}'|$ are the Green's functions in the lossy dielectric and in free space, respectively. The wavenumbers are $k_2 = \omega\sqrt{\mu_0\epsilon_2}$, $k_0 = \omega\sqrt{\mu_0\epsilon_0}$, and ϵ_2 is the (complex) permittivity of the dielectric. The time dependence is assumed to be $\exp(j\omega t)$.

For the point-contact BOR(II) model, one may readily formulate the following integral equations:

$$\bar{E}^i(\bar{r}) = \frac{1}{4\pi} \left\{ \int_{S_1} [j\omega\mu_0 \bar{J}_{S_1} \Phi_1 - \frac{1}{j\omega\epsilon_0} \nabla_{S'} \cdot \bar{J}_{S_1} \nabla \Phi_1] dS' + \int_{S_3} [j\omega\mu_0 \bar{J}_{S_3} \Phi_1 - \frac{1}{j\omega\epsilon_0} \nabla_{S'} \cdot \bar{J}_{S_3} \nabla \Phi_1 - \bar{K}_{S_3} \times \nabla \Phi_1] dS' \right\}$$

for $\bar{r} \in S_1$, (11)

$$\bar{E}^i(\bar{r}) = \frac{1}{4\pi} \left\{ \int_{S_1} [j\omega\mu_0 \bar{J}_{S_1} \Phi_1 - \frac{1}{j\omega\epsilon_0} \nabla_{S'} \cdot \bar{J}_{S_1} \nabla \Phi_1] dS' + \int_{S_3} [j\omega\mu_0 \bar{J}_{S_3} (\Phi_1 + \Phi_2) - \frac{1}{j\omega} \nabla_{S'} \cdot \bar{J}_{S_3} \nabla (\frac{\Phi_1}{\epsilon_2} + \frac{\Phi_2}{\epsilon_2}) - \bar{K}_{S_3} \times \nabla (\Phi_1 + \Phi_2)] dS' \right\}$$

for $\bar{r} \in S_3$, (12)

$$\begin{aligned}
\bar{H}^1(\bar{r}) = \frac{1}{4\pi} \left\{ \int_{S_1} \bar{J}_{S_1} \times \nabla \phi_1 dS' + \int_{S_3} [\bar{J}_{S_3} \times \nabla(\phi_1 + \phi_2) \right. \\
\left. + j\omega \bar{K}_{S_3} (\epsilon_0 \phi_1 + \epsilon_2 \phi_2) - \frac{1}{j\omega \mu_0} \nabla_{S'} \cdot \bar{K}_{S_3} \nabla(\phi_1 + \phi_2)] dS' \right\}, \\
\text{for } \bar{r} \in S_3 \quad . \quad (13)
\end{aligned}$$

One notes that for this model the conductor-dielectric interface S_2 reduces to a point. Thus \bar{J}_{S_2} vanishes and \bar{J}_{S_1} and \bar{J}_{S_3} both approach zero at the contact point. All other quantities are defined the same as in Eqs. (7) - (10).

In order to evaluate the unknown currents, one first expands the currents in a Fourier series in the circumferential angle ϕ and uses triangle-functions to represent the variation of the current with the coordinate t . The unknown coefficients of the triangular expansion functions are then determined from a set of algebraic equations which are obtained by testing the above equations (7) - (13) with appropriate triangle testing functions and equating the ϕ -independent Fourier components on both sides of the equations. The solution procedure is rather involved but essentially parallels that found in [10, 12], except that half-triangles are used to represent the nonzero currents \bar{J}_{S_1} , \bar{J}_{S_2} , and \bar{J}_{S_3} at the air-conductor-dielectric interface in the BOR(I) model. The above SIE method has been successfully applied to the composite body represented by the missile with a homogeneous plume model and the numerical results are shown in Section 3.3. In principle, the SIE method can also be applied to the composite body consisting of a missile

with a multi-layered inhomogeneous plume by using an invariant imbedding technique [13,14]. This approach is currently under investigation.

3.2. Approximate Integral Equation (AIE) Method

It is a very difficult and complicated matter to accurately model a missile with an attached plume, whose composition varies both axially and radially. However, an approximate so-called AIE method is employed here to obtain a simple first order solution to this problem. The approach here is to derive an approximate boundary condition relating the tangential fields at the outer surface of the plume and to model the effect of the plume by an impedance type boundary condition on the fields at the plume surface. Specifically, the inhomogeneous plume is first divided into N segments along its axis. To estimate the equivalent surface impedance at each segment, one then calculates the appropriate ratio of surface electric and magnetic fields. To obtain these fields, we locally approximate the radially inhomogeneous segment by a multilayered infinite circular cylinder, which is then solved via an iteration procedure developed by Bussey and Richmond [15]. Once the surface impedance is determined, the unknown electric and magnetic current densities on the outermost surface of the plume are thus related to each other through this surface impedance or so-called Leontovich boundary condition [16,17],

$$\bar{K}_S \times \hat{n} = Z_S \bar{J}_S \quad (14)$$

where Z_S is the calculated surface impedance of the inhomogeneous plume segment, and \hat{n} is the unit normal vector to the plume surface.

The use of the Leontovich or surface impedance approximation relies on

the following assumptions: (a) the ratio of surface electric and magnetic fields is not a strong function of the angle of incidence, (b) there is not a strong interaction between adjacent subsections and (c) the plume surface may be approximated locally as a cylinder. Conditions (a) and (b) should be satisfied for moderate and high conductivities near the plume surface. Condition (c) should hold everywhere except possibly in the missile-plume junction region.

Since the impedance condition (14) relates the surface fields or equivalent currents, the number of unknown quantities is reduced and one is able to derive an AIE for only one of the unknown plume surface currents. Similar to the derivation of Eqs. (7 - 10), with condition (14), one may easily arrive at the following AIE:

$$\bar{E}^i = \frac{z_s \bar{J}_s}{2} + \int_S [j\omega\mu \bar{J}_s \Phi_1 - \frac{\nabla_s' \cdot \bar{J}_s}{j\omega\epsilon_0} \nabla\Phi_1 + z_s (\hat{n}' \times \bar{J}_s) \times \nabla\Phi_1] dS' . \quad (15)$$

The above equation is implicitly valid for tangential components only. Note that z_s is zero on the conducting rocket and varies with position along the outer surface of the plume. The integral equation may be solved using the same numerical procedures indicated in the previous section. Here again, only the zeroth Fourier component of the unknown current \bar{J}_s is needed on the missile structure.

The AIE method may also be applied to homogeneous plume models where the surface impedance is calculated according to Eq. (2). Numerical results for homogeneous plume models may thus be obtained using either the SIE or the AIE method, and some results using both methods are given in the next section for comparison. The applicability and accuracy of AIE method are

also discussed.

3.3. Numerical Results

The SIE solution for the total axial current on a homogeneous dielectric circular cylinder (length $h = .737\lambda$, radius $a = .025\lambda$, $\epsilon_r = 50$, conductivity $\sigma = 20.37 \text{ S/m}$) is plotted in Fig. 53 for the case of a broadside incident plane wave ($f = 9.45\text{GHz}$). The good agreement among the various numerical solutions validates the calculation of the zeroth order Fourier component using the SIE method. In Figs. 54 and 55 the current magnitudes on various missile-plume models are plotted for broadside and 30° incident plane wave illuminations ($f = 50 \text{ MHz}$), respectively. For the base-contact BOR(I) model, the SIE solutions are in good agreement with the thin-wire code solutions. The SIE solution for the point-contact BOR(II) model, however, yields significantly different results from the thin-wire model for the broadside incident case. The difference is obviously due to the fact that in this model current is not allowed to flow from the missile into the plume region because the contact area between the missile and plume is zero. In the 30° incident case, the current in the junction region happens to be small anyway, so that requiring it to vanish at the interface in the BOR(II) model does not significantly change the overall current magnitude. In Figs. 56 and 57 we show the current magnitude on various missile-plume models with differing plume shapes for broadside and 30° incident plane waves ($f = 50 \text{ MHz}$), respectively. In each case the plume is homogeneous and the conductivity is 0.2 S/m . As in the case of the thin-wire, at broadside incidence, the plume suppresses the missile current amplitudes, whereas near grazing incidence, e.g., $\theta_i \leq 30^\circ$, the current is enhanced. Some influence due to the

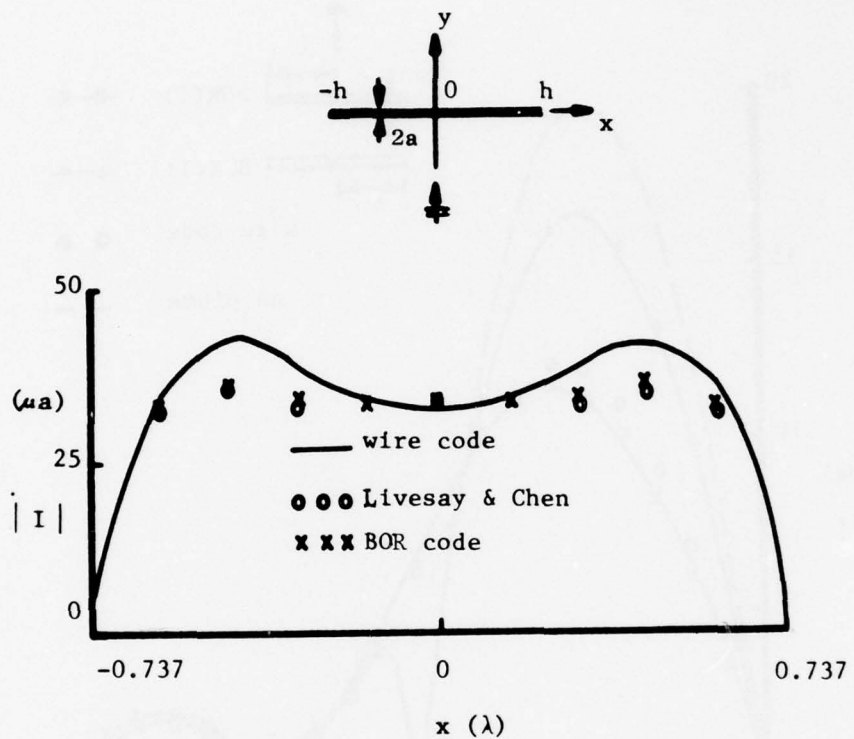


Figure 53. Current magnitude on a homogeneous dielectric cylinder
 $(\epsilon_r = 50, \sigma = 20.37 \text{ U/m}, h = 0.737\lambda, a = 0.025\lambda, f = 9.45 \text{ GHz})$.

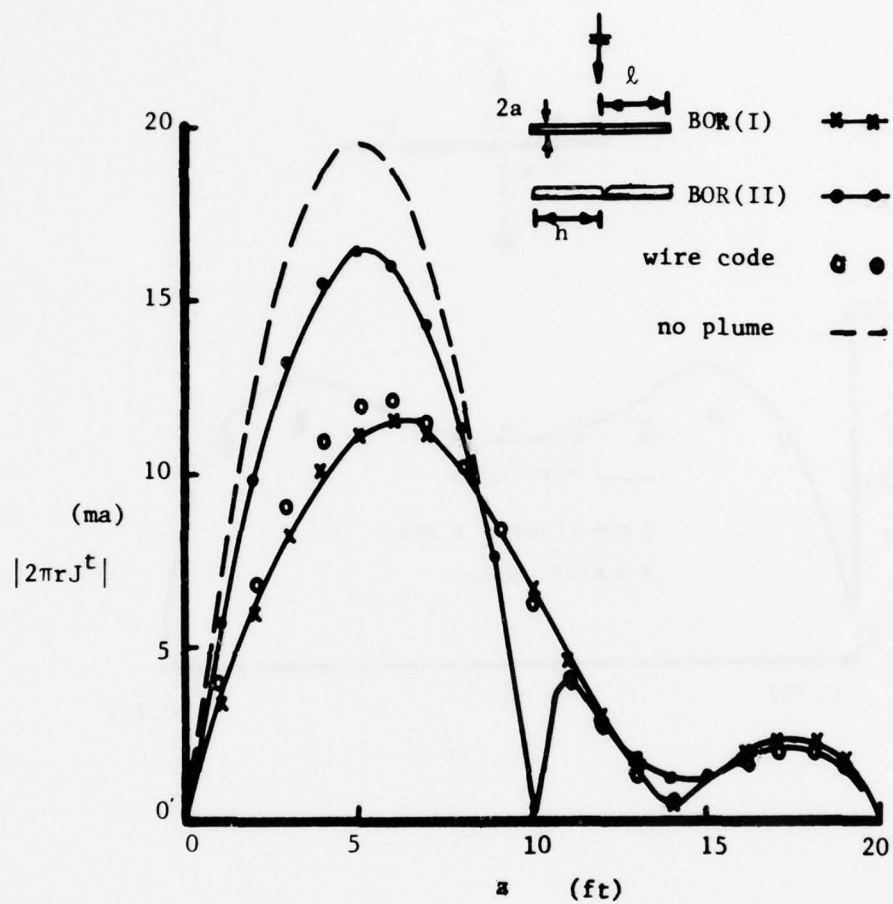


Figure 54. Current magnitude on missile (length $h = 10'$, radius $a = 2.5''$) with and without homogeneous plume (length $l = 10'$, radius $a = 2.5''$, $\sigma = 0.2 \text{ } \text{U/m}$), broadside incidence ($f = 50 \text{ MHz}$).

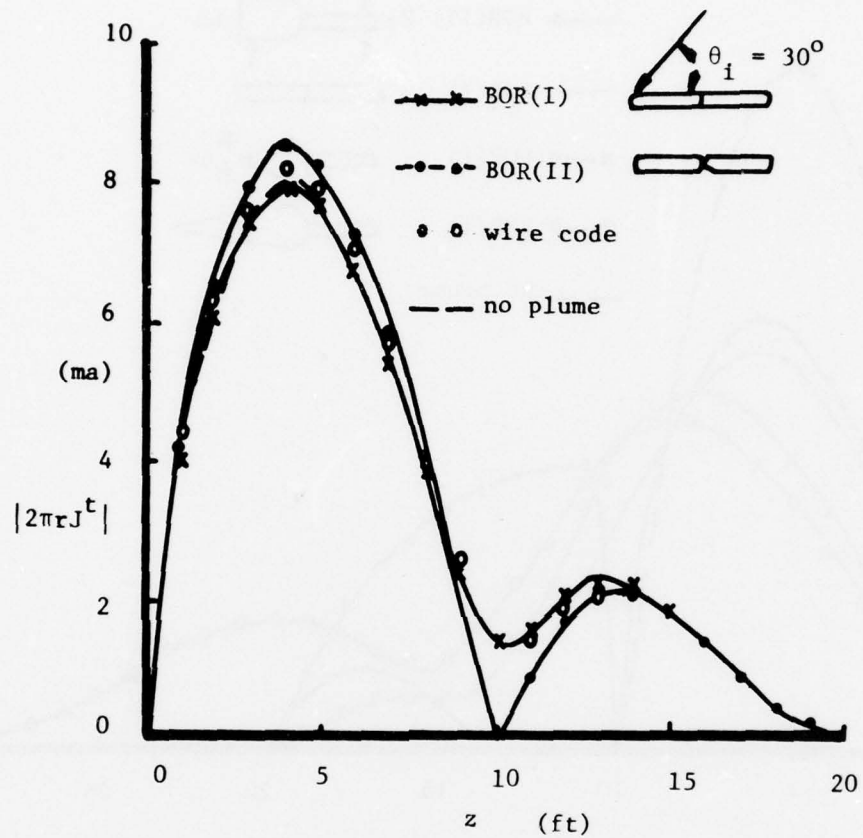


Figure 55. Current magnitudes on the same missile as Figure 54 but for angle of incidence $\theta_i = 30^\circ$.

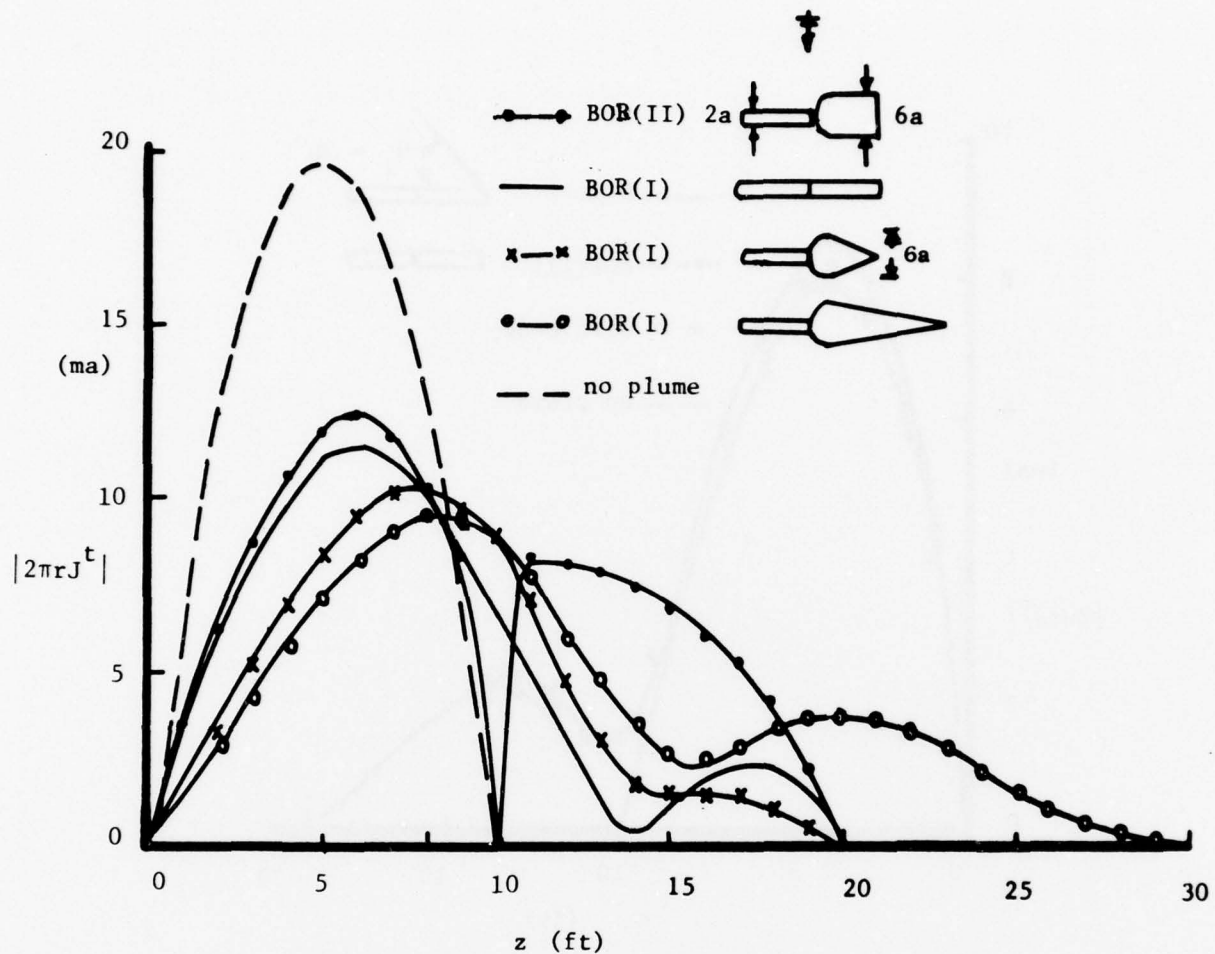


Figure 56. Current magnitudes on missile ($h = 10'$, $a = 2.5''$) with plumes of various shapes ($b = 3a$, $l = 10'$ and $20'$, $\sigma = 0.2 \text{ S/m}$) broadside incidence, $f = 50 \text{ MHz}$.

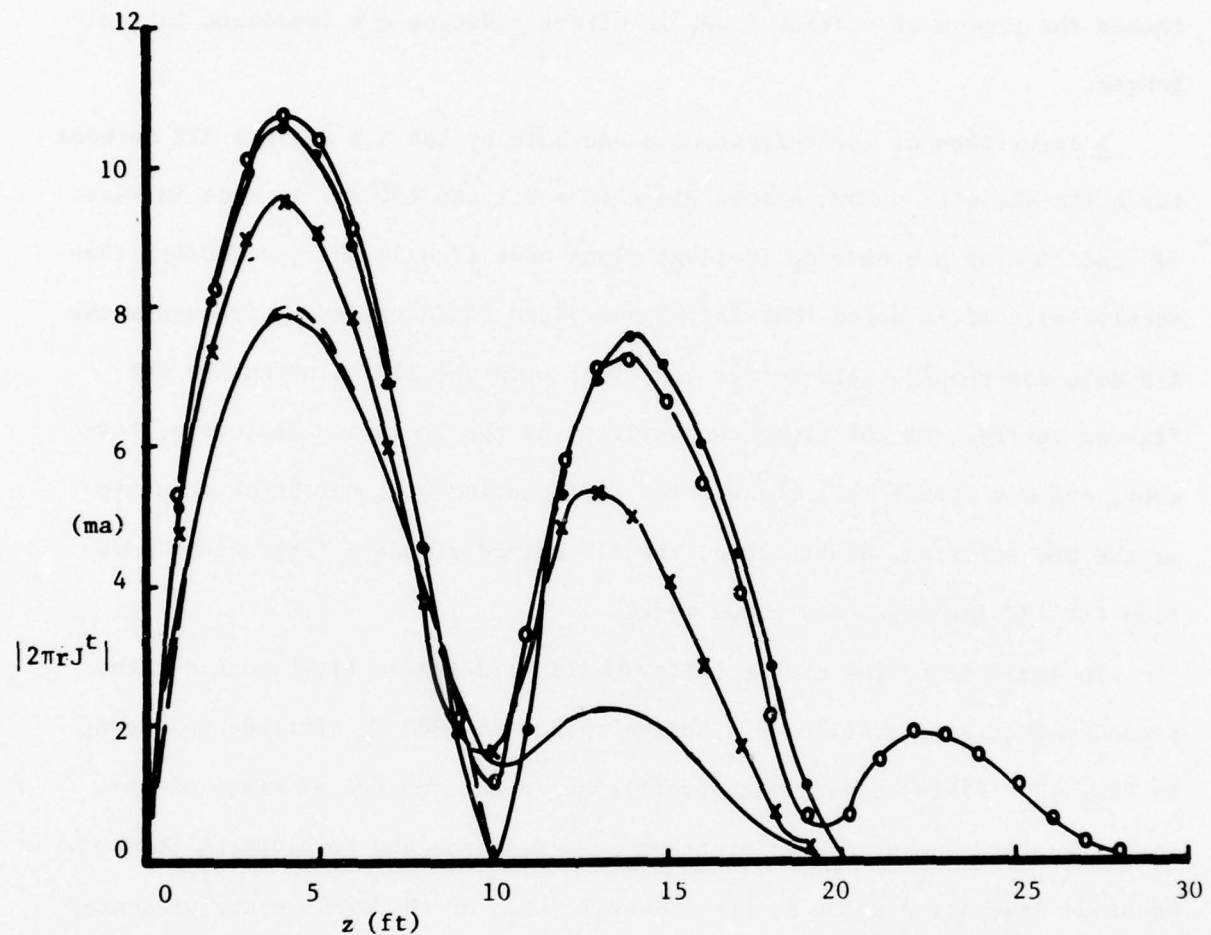


Figure 57. Current magnitudes on the same missile plume configurations as Figure 56 but for angle of incidence $\theta_i = 30^\circ$.

plume shape and length can also be seen. In general, for a fixed conductivity, the larger the plume radius, the more nearly it behaves like a perfect conductor. This is because increasing the plume cross section increases the region of current flow, in effect reducing the impedance per unit length.

A comparison of the current obtained both by the SIE and the AIE methods for a missile with a homogeneous plume ($\sigma = 0.1$ and $1 \text{ mhos}/\text{m}$) is made in Figs. 58 and 59 for a broadside incident plane wave ($f = 50 \text{ MHz}$ and 100 MHz , respectively). It is noted that for higher plume conductivity or frequency the AIE solution should yield better agreement with the SIE solution, as the figures verify. As the plume conductivity or the frequency decreases, however, one may expect that the simpler AIE solution will not be as accurate as the SIE solution. Nonetheless, the AIE method yields a first order solution for the inhomogeneous plume model.

To demonstrate the applicability of AIE solution we first consider the plume conductivity profile of a Redeye rocket at 5000 ft. altitude as shown in Fig. 60. (This conductivity profile has been computed by means of the so-called LAPP computer code at the Missile Research and Development Command, Redstone Arsenal, Alabama [5].) Several views of the profile are presented in order to observe the detailed structure. Fig. 61 shows the maximum radius used in our model of the plume at each point. At points on the surface in Fig. 61, an equivalent surface impedance was computed and used in the AIE. The resulting AIE current solutions for this inhomogeneous plume model are plotted in Figs. 62 and 63 for the cases of broadside and 30° incident plane waves ($f = 100 \text{ MHz}$), respectively. Also plotted are the AIE solutions for a homogeneous plume model with plume conductivity $\sigma = 0.1 \text{ mhos}/\text{m}$.

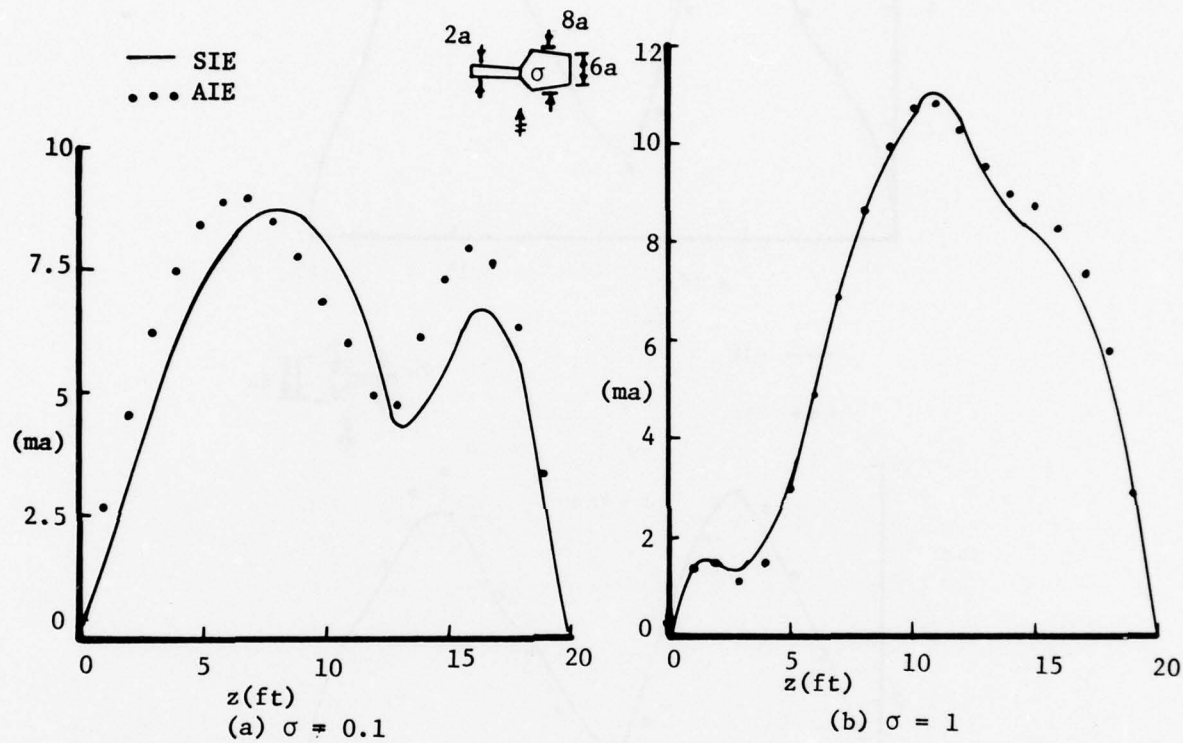


Figure 58. Current magnitudes on missile ($h = \ell = 10'$, $a = 2.5''$) with homogeneous plume via the SIE and AIE approaches for (a) $\sigma = 0.1 \text{ V/m}$, (b) $\sigma = 1 \text{ V/m}$, $f = 50 \text{ MHz}$, broadside incidence.

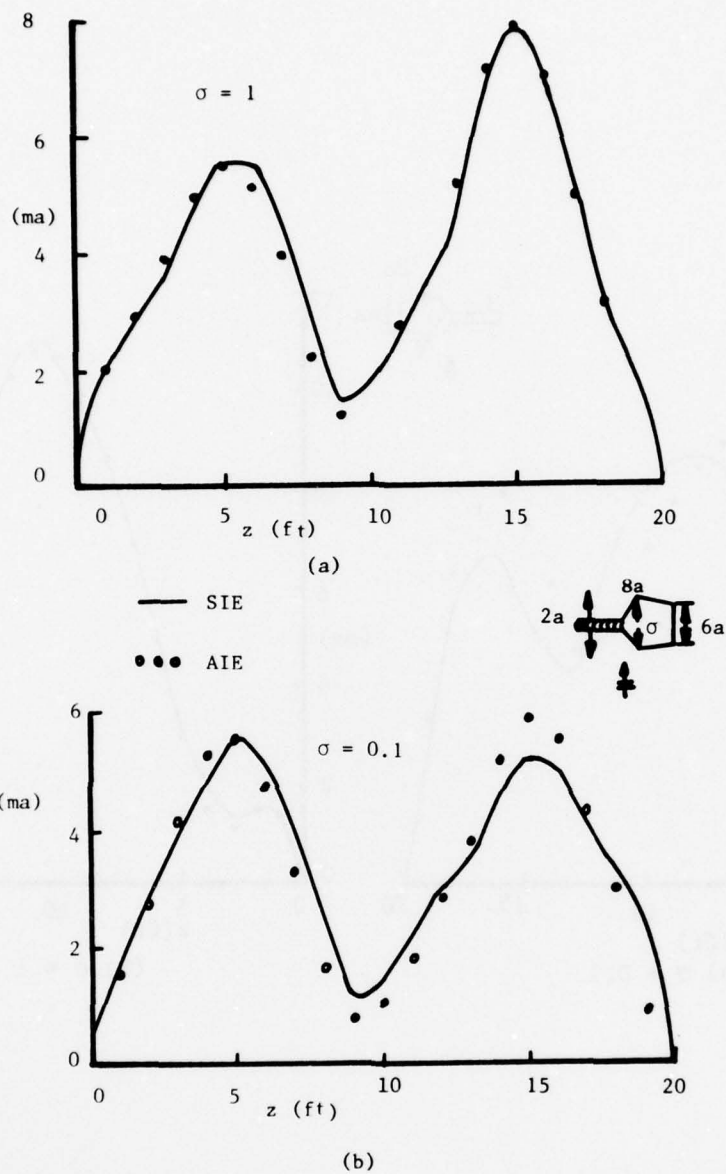


Figure 59. Current magnitude on the same missile as Figure 58 but at a frequency $f = 100$ MHz.

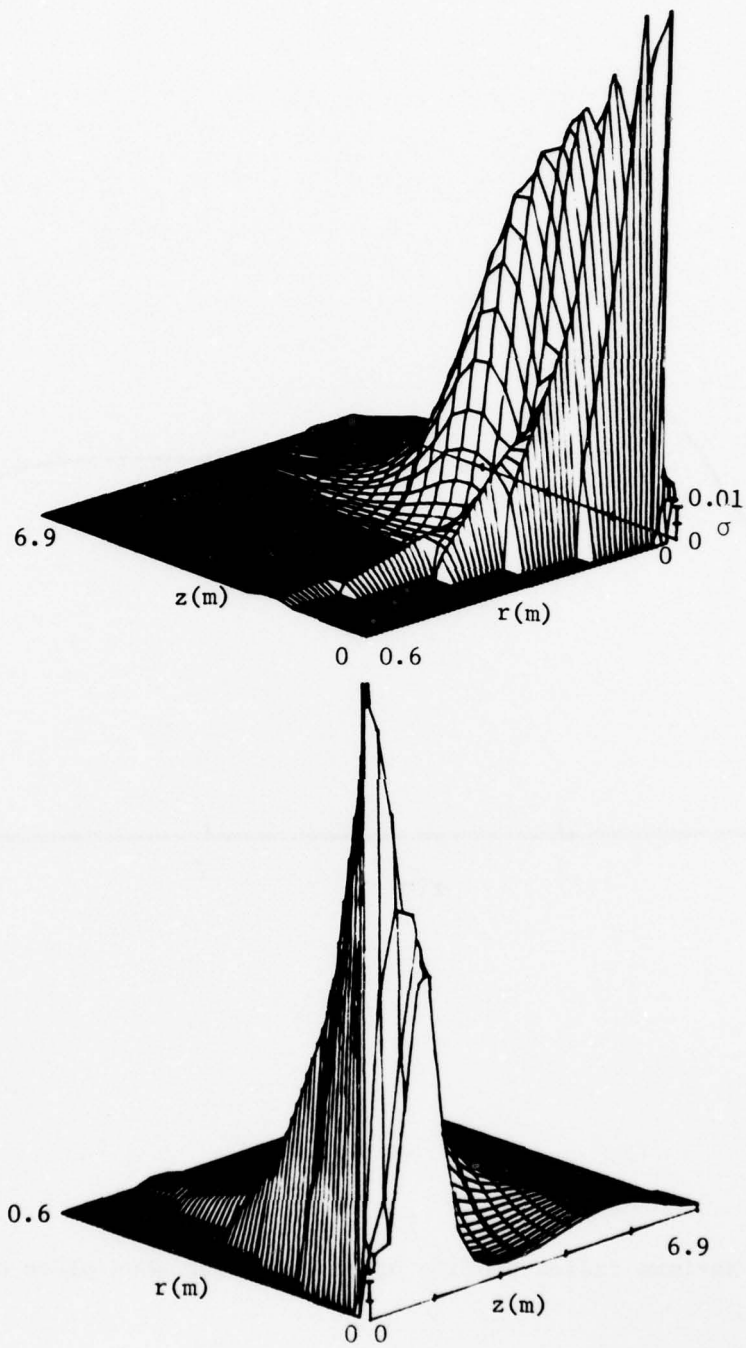


Figure 60. Three-dimensional view of inhomogeneous plume conductivity profiles computed for a Redeye missile at 5000 ft. altitude.

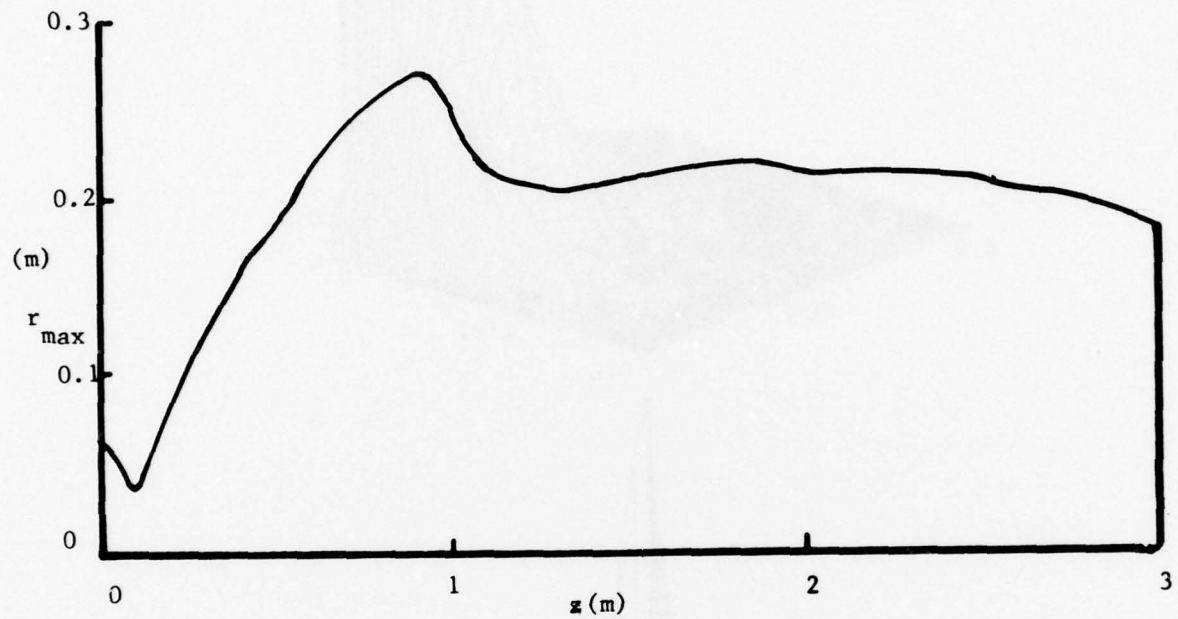


Figure 61. Maximum radius profile of the inhomogeneous plume of Figure 60.

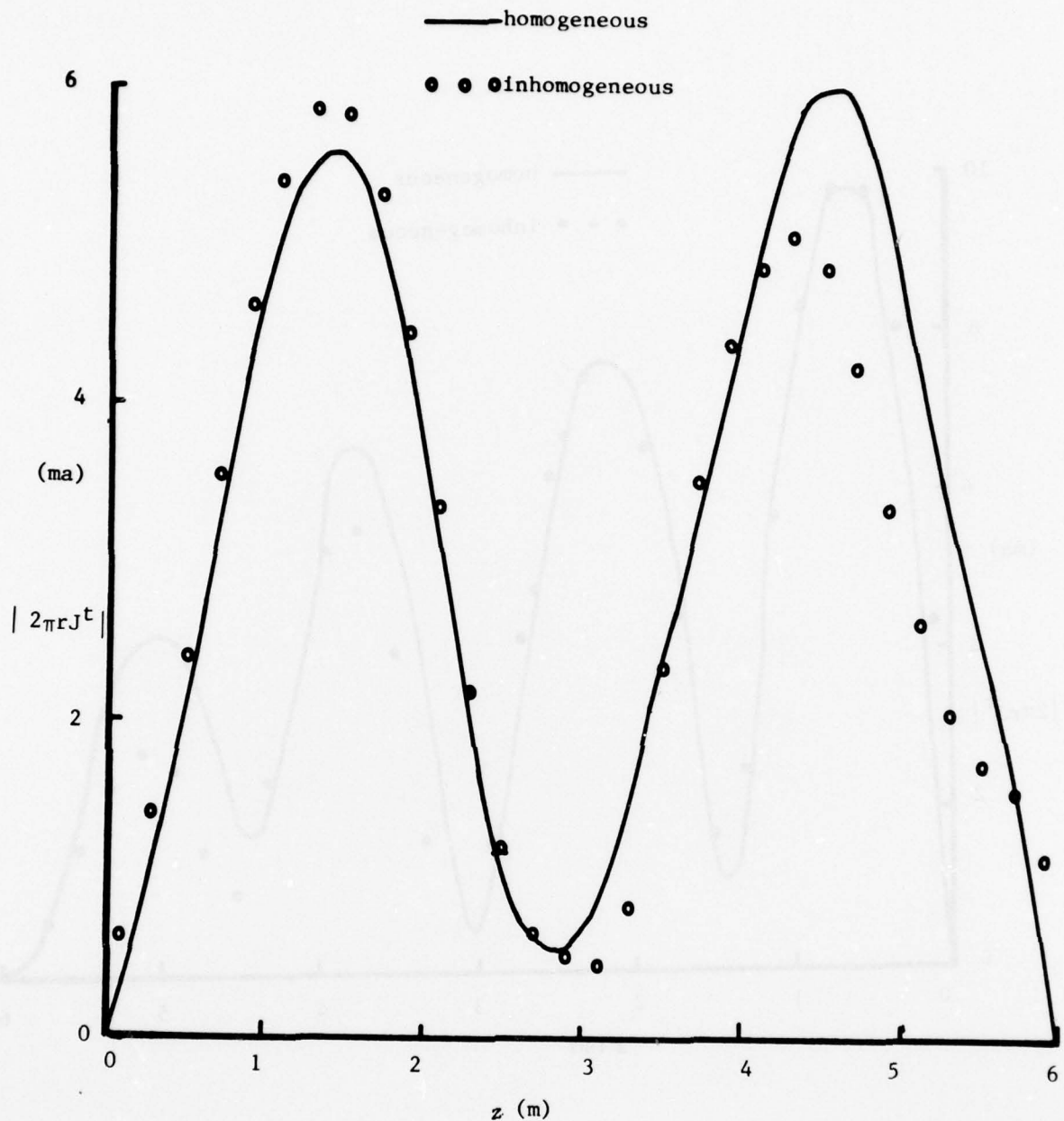


Figure 62. Current magnitude on a Chaparral missile ($h=3\text{m}$, $a=6.35\text{cm}$) with homogeneous plume compared to the Redeye plume model of Figures 60 and 61, $f=100\text{ MHz}$, broadside incidence.

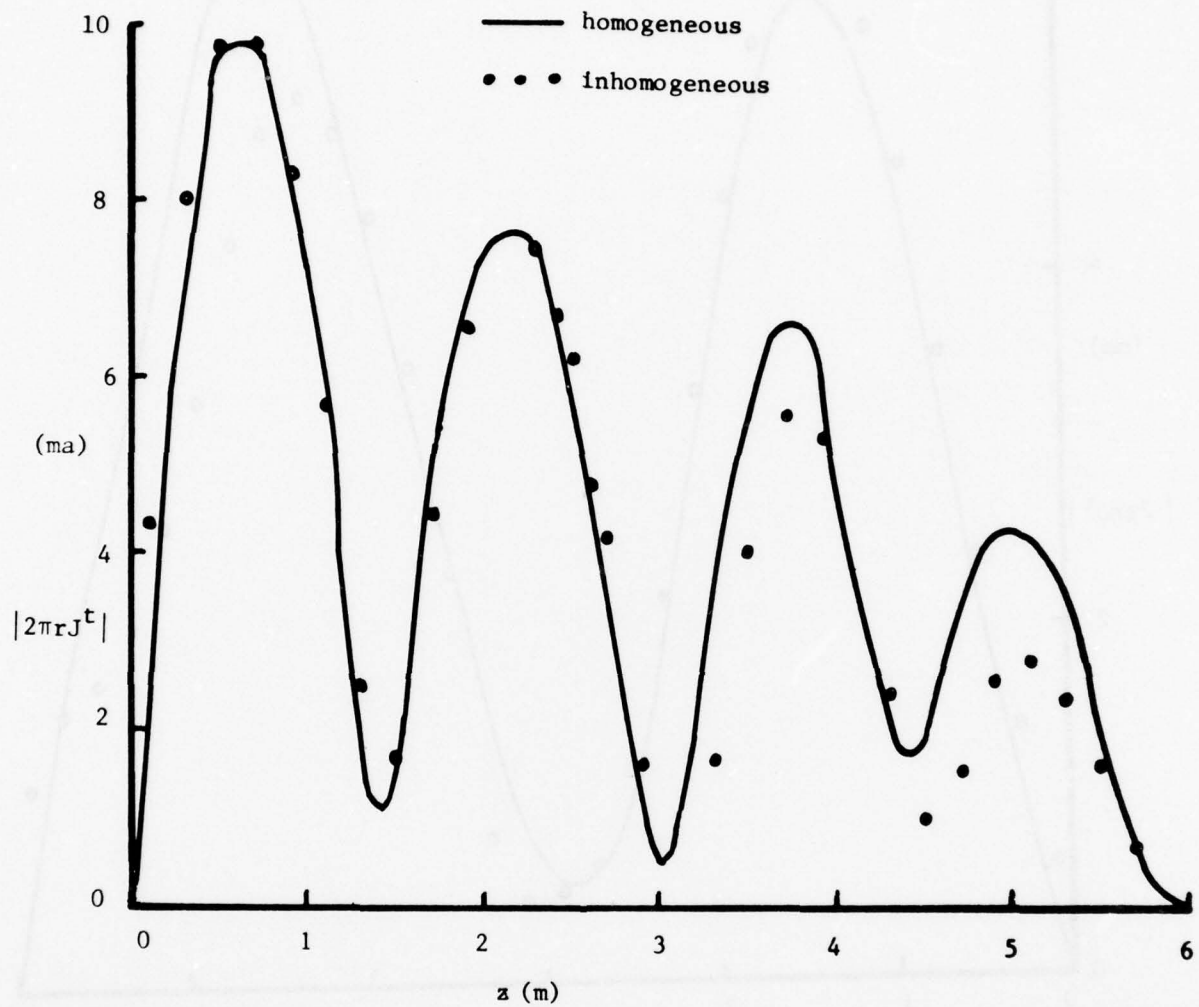


Figure 63. Current magnitude on the same configurations as Figure 62 but with angle of incidence $\theta_i = 30^\circ$.

Since this conductivity is considerably higher than the average conductivity of the inhomogeneous model, one would expect the currents on the plume in the homogeneous model to be slightly higher than those of the inhomogeneous case, as is confirmed by Figs. 62 and 63. Note that the currents on the conductor portion are almost equal, however. For this example, then, the homogeneous model might be adequately substituted for the actual inhomogeneous plume. Indeed, for most of the data we have considered here the results do not seem to depend strongly on the actual model employed.

Consider next the inhomogeneous plume corresponding to a Chaparral missile ($h = 3\text{m}$, $a = 6.35\text{cm}$) at a 5000 ft. altitude, with the conductivity profile shown in Fig. 64. The corresponding maximum conductivity profile is plotted in Fig. 65 along the plume axis. One notes that the plume conductivity of the long plume model is rather low near the nozzle (i.e. $z < 0.684\text{ m}$). It is agreed that computed plume conductivities generated by the LAPP code in the nozzle region are rather inaccurate due to an inability to adequately model the complicated plume dynamics near the nozzle. In order to assess the effect of the inaccurate modeling in the nozzle region, we have adopted an alternative plume model in which the low conductivity section near the rocket nozzle has been removed (see Fig. 65). This model is termed the "short plume model." Figs. 66 and 67 show the current distribution on these two models illuminated by a plane wave at 50 MHz with incident angle θ_i equal to 90° and 30° , respectively. As can be seen, the two inhomogeneous plume models give rather different results. The long plume model with the low conductivity section near the rocket nozzle (at 3m.) tends to reduce the current amplitude near the missile tail, while the short plume permits large currents to flow on to the plume section, in this case

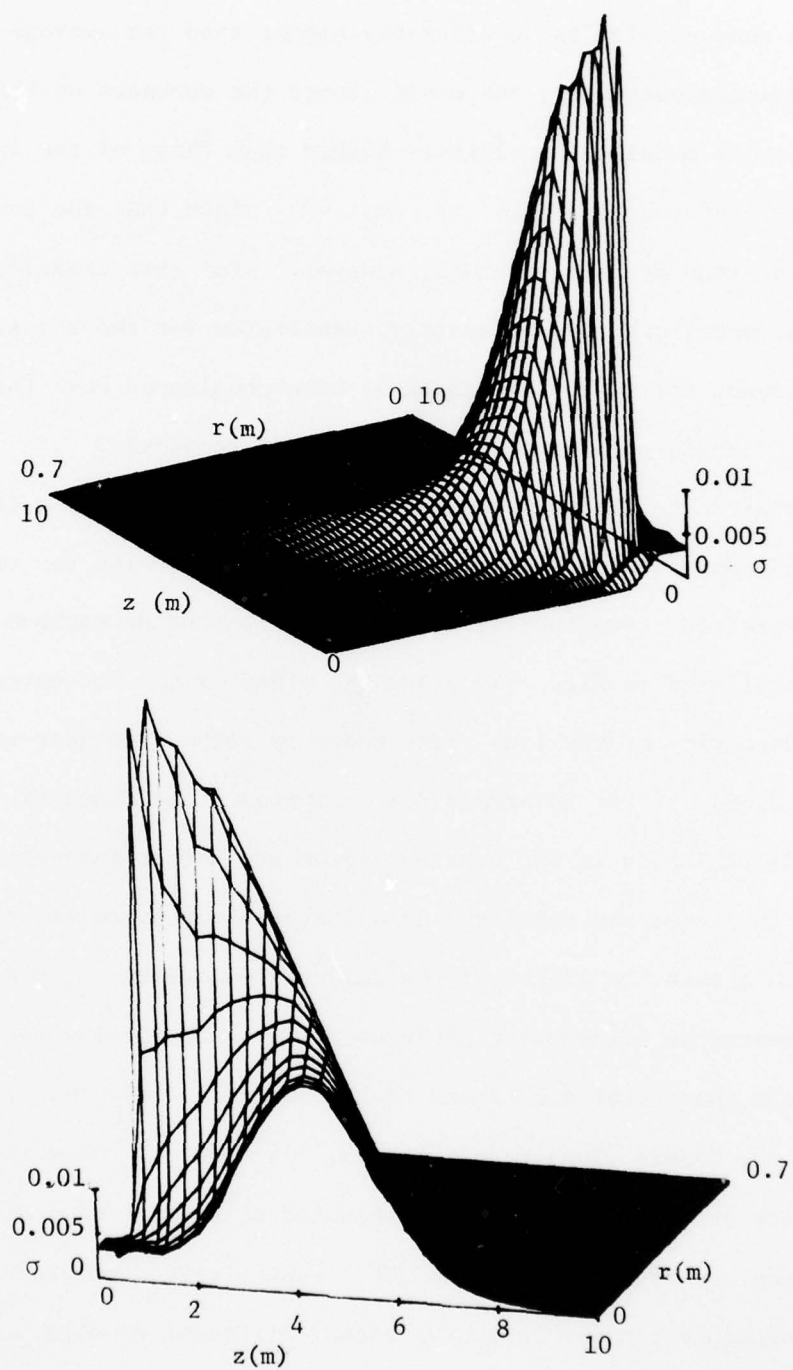


Figure 64. Three-dimensional views of inhomogeneous plume conductivity profiles computed for a Chaparral missile at 5000 ft. altitude.

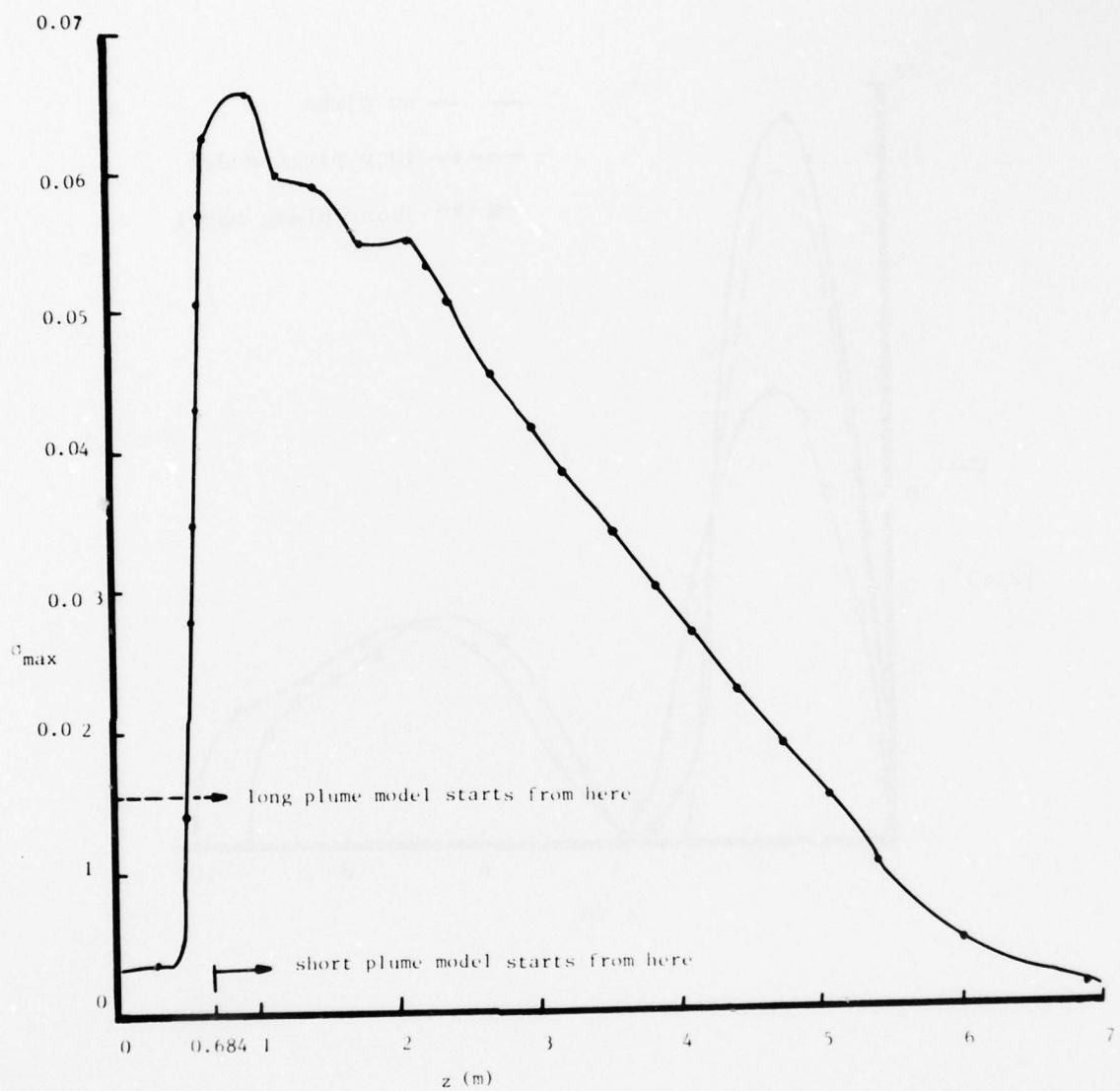


Figure 65. Maximum conductivity profile of the inhomogeneous plume of Figure 64.

AD-A064 976

GEORGIA TECH RESEARCH INST ATLANTA
EFFECTS OF VARIOUS EXHAUST PLUME MODELS ON MISSILE SKIN CURRENT--ETC(U)
JAN 79 T K WU, D R WILTON, L L TSAI

F30602-75-C-0118

RADC-TR-78-261

F/G 20/3

NL

UNCLASSIFIED

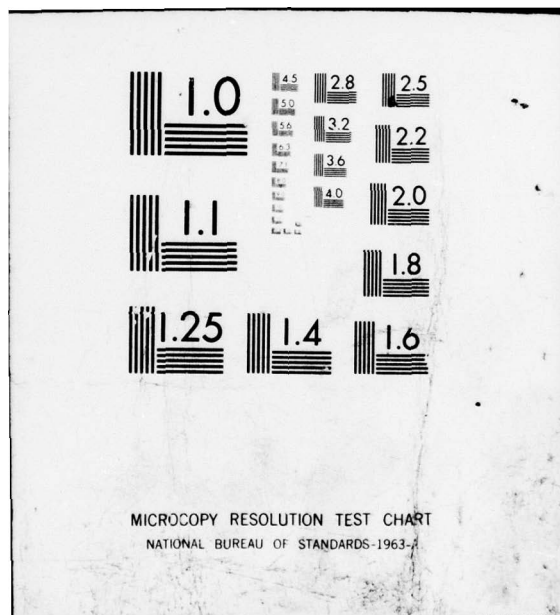
2 OF 2

AD
A064 976

REF ID: A64976



END
DATE
FILMED
4-79
DDC



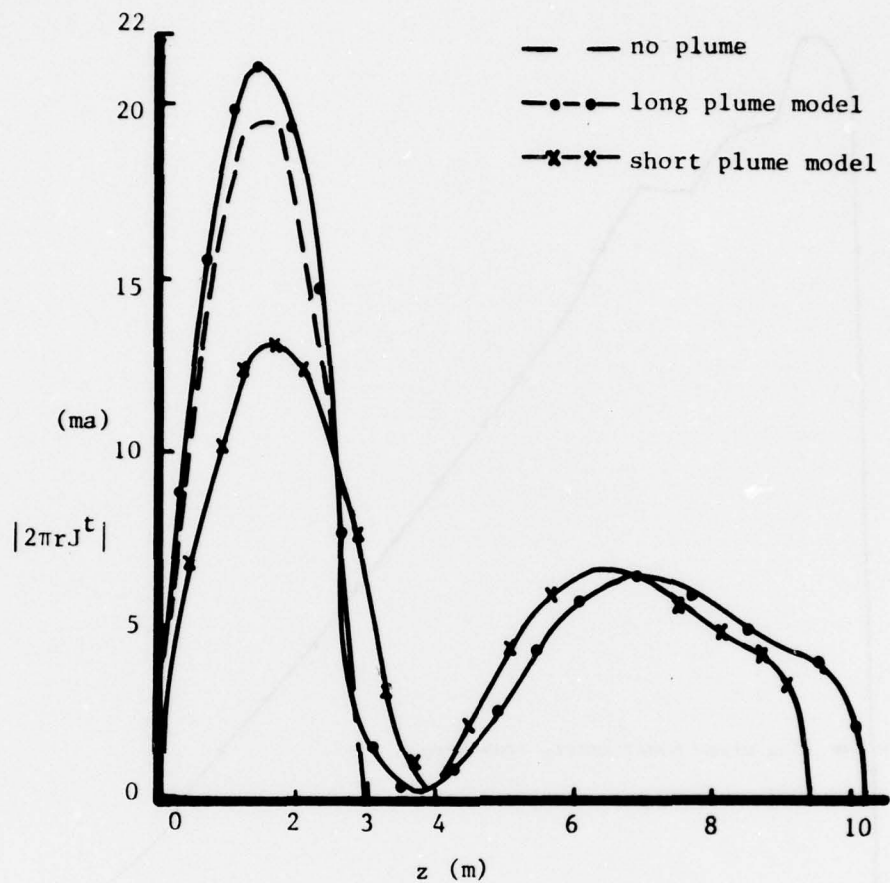


Figure 66. Current magnitude on a Chaparral missile ($h = 3\text{m}$, $a = 6.35\text{ cm}$) with and without the two inhomogeneous plume models, $\theta_i = 90^\circ$, $f = 50\text{ MHz}$.

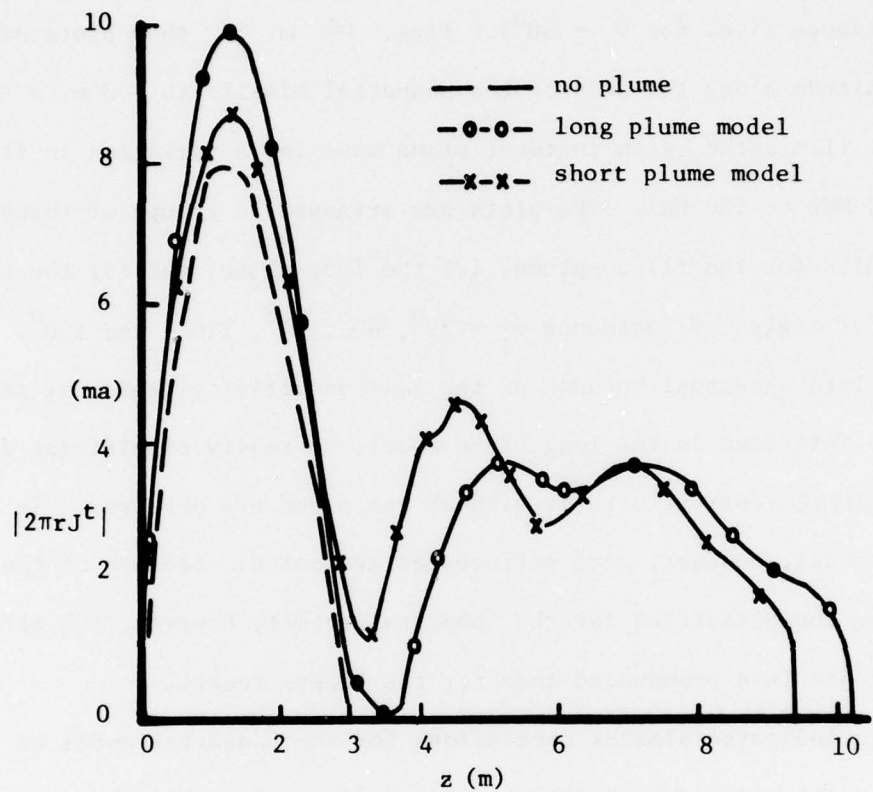


Figure 67. Current magnitude on a Chaparral missile with and without the two inhomogeneous plume models, $\theta_i = 30^\circ$, $f = 50$ MHz.

reducing the peak current on the missile. As has been found for the homogeneous plume models at this frequency, both inhomogeneous plume models show a larger current peak than the no-plume case when the plane wave is at grazing incidence (i.e. for $\theta_i \leq 30^\circ$). Figs. 68 to 82 show plots of the current magnitude along the axis of the Chaparral missile ($h = 3$ m, $l = 7.2$ m, $a = 6.35$ cm) illuminated by an incident plane wave for a variation in frequency of 30 MHz to 150 MHz. The plots are arranged in groups of three showing results for the (1) no-plume, (2) the long plume, and (3) the short plume case for angles of incidence $\theta_i = 30^\circ, 60^\circ, 90^\circ, 120^\circ$, and 150° . Again, the plots show that because of the low-conductivity region at the plume-nozzle interface in the long plume model, no really significant differences in missile current with or without the plume are observed. In the short plume model, however, some differences are noted. Because of the much smaller plume conductivities for the Chaparral rocket, however, the effects of the plume are less pronounced than for the Redeye rocket.

The data indicates similar conclusions for the Chaparral model as for the Redeye model studied by Smith et. al [4], namely, that the missile current is increased by the presence of the plume at lower frequencies because of the increased effective length of the missile/plume scattering configuration. The resonance frequencies are slightly shifted by the plume and some damping takes place due to the plume losses. Note in the figures, however, that possibly some resonance peaks have been missed because of the relatively large interval between the frequencies in the data. Intermediate frequency data points were not computed because of the high cost of the computations.

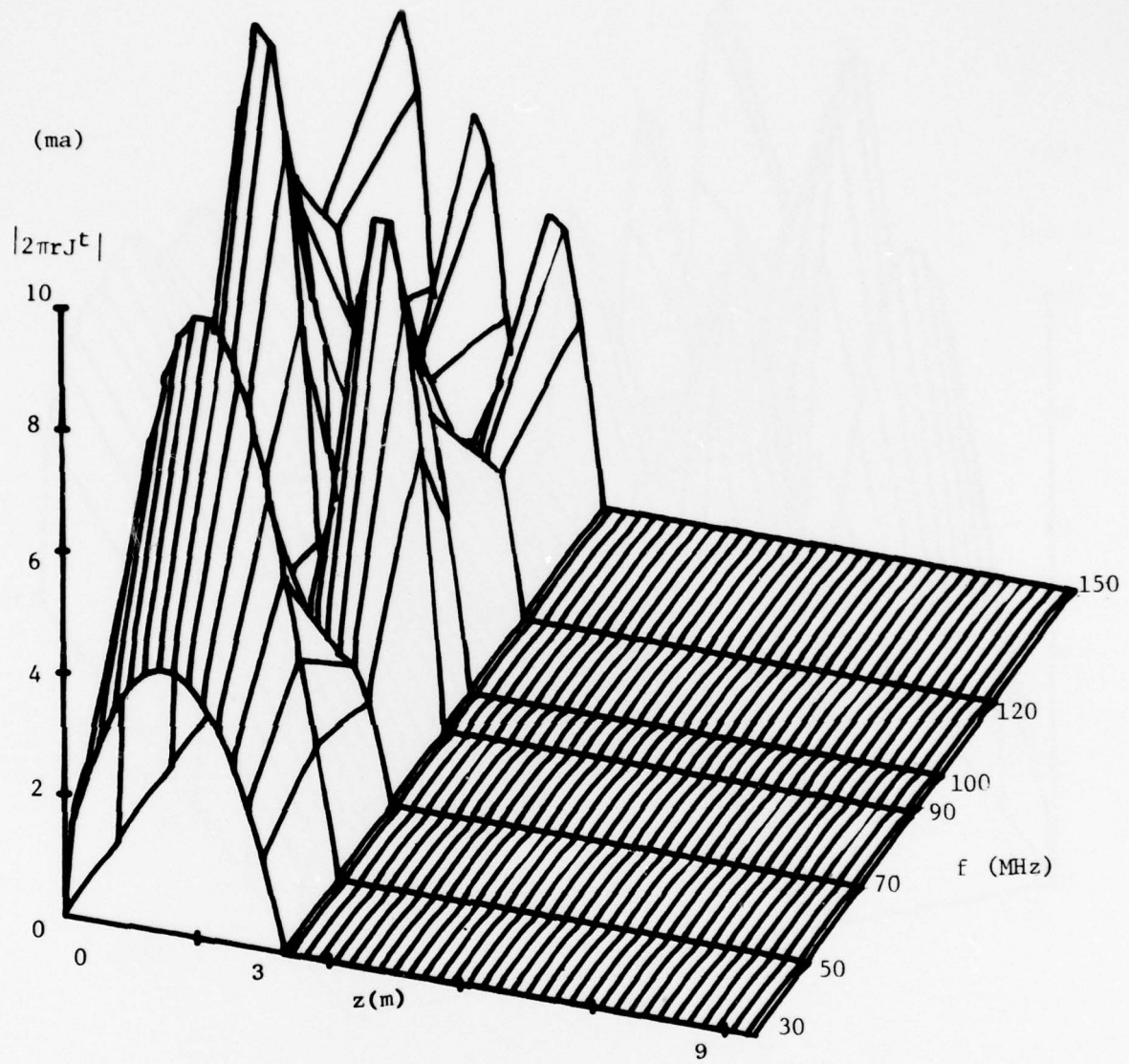


Figure 68. Current on a Chaparral missile ($h = 3$ m, $l = 7.2$ m, $a = 6.35$ cm) as a function of frequency, no plume, $\theta_i = 30^\circ$.

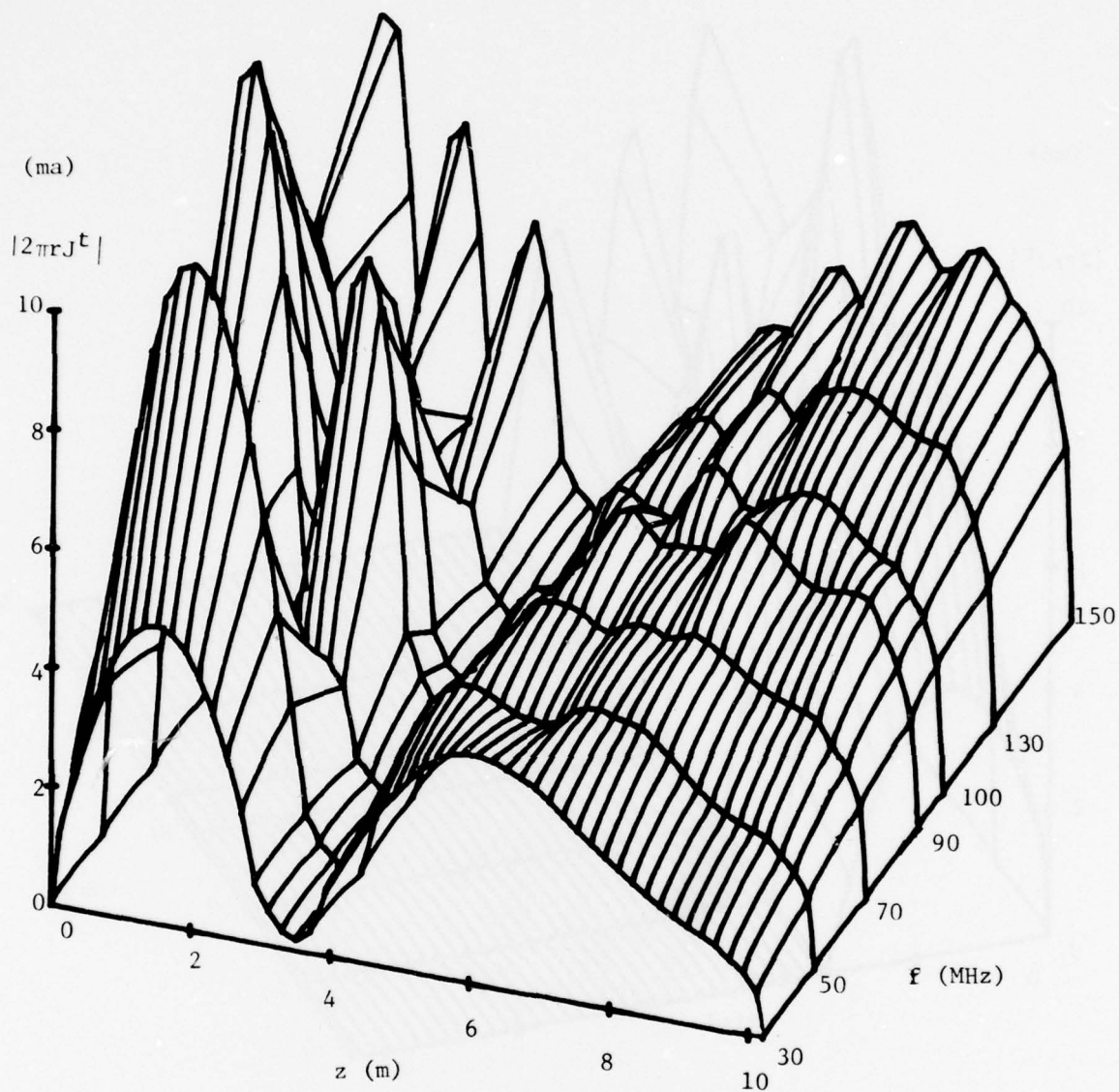


Figure 69. Current magnitude on a Chaparral missile ($h = 3$ m, $\ell = 7.2$ m, $a = 6.35$ cm), as a function of frequency, long plume model, $\theta_i = 30^\circ$.

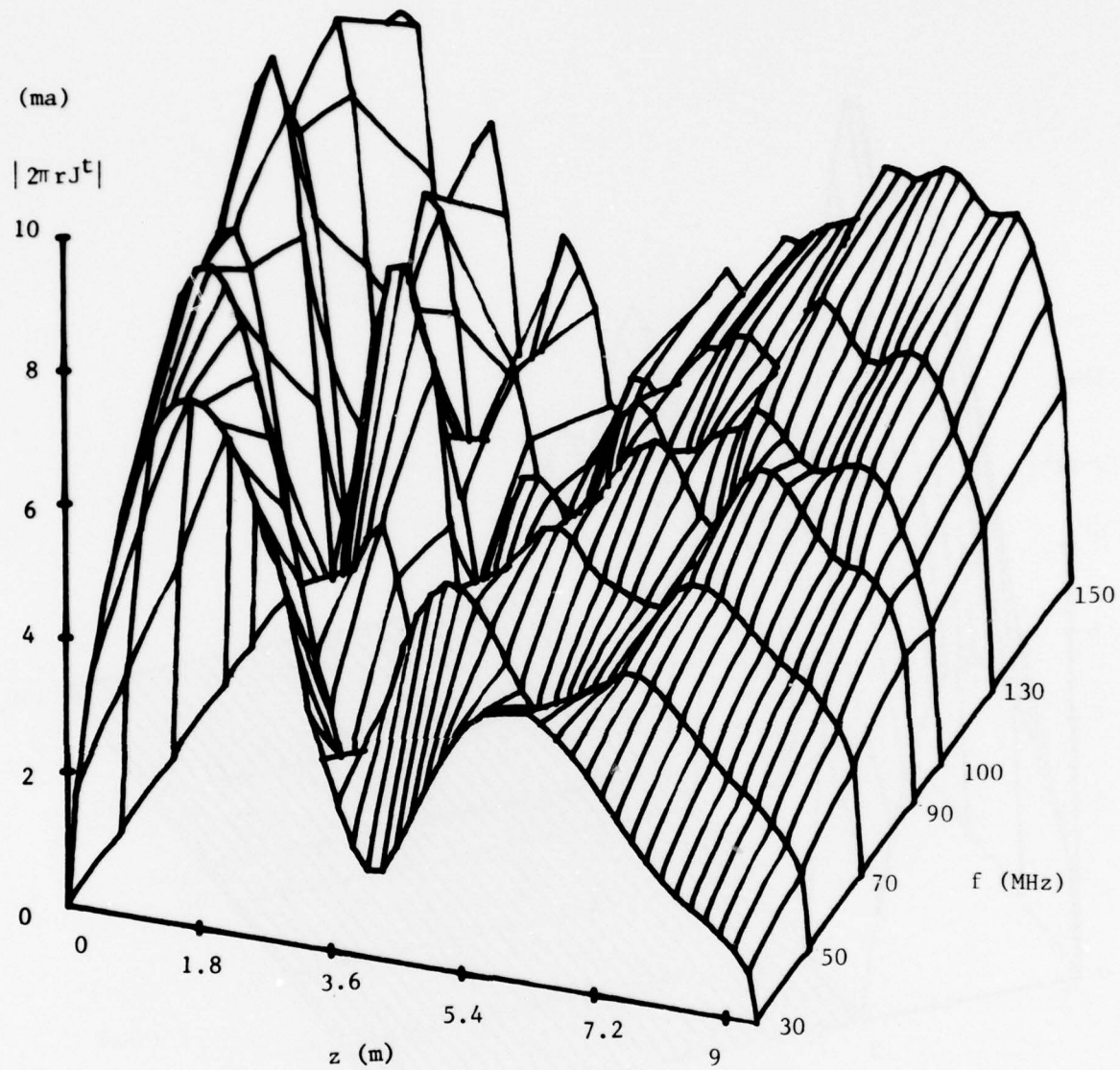


Figure 70. Current on a Chaparral missile, ($h = 3$ m, $l = 6.4$ m, $a = 6.35$ cm) as a function of frequency, short plume model, $\theta_i = 30^\circ$.

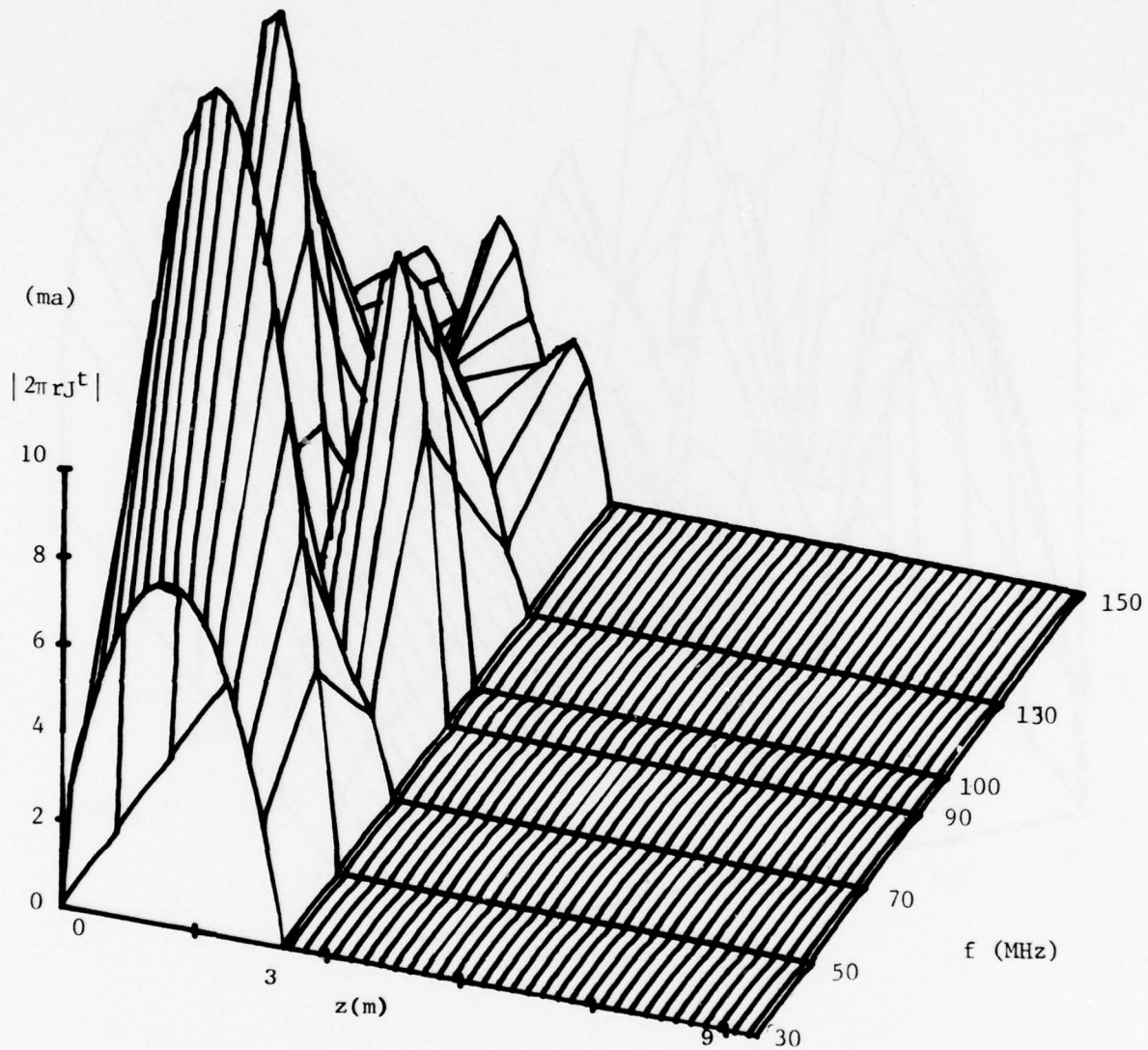


Figure 71. Current on a Chaparral missile as a function of frequency,
no plume, $\theta_i = 60^\circ$.

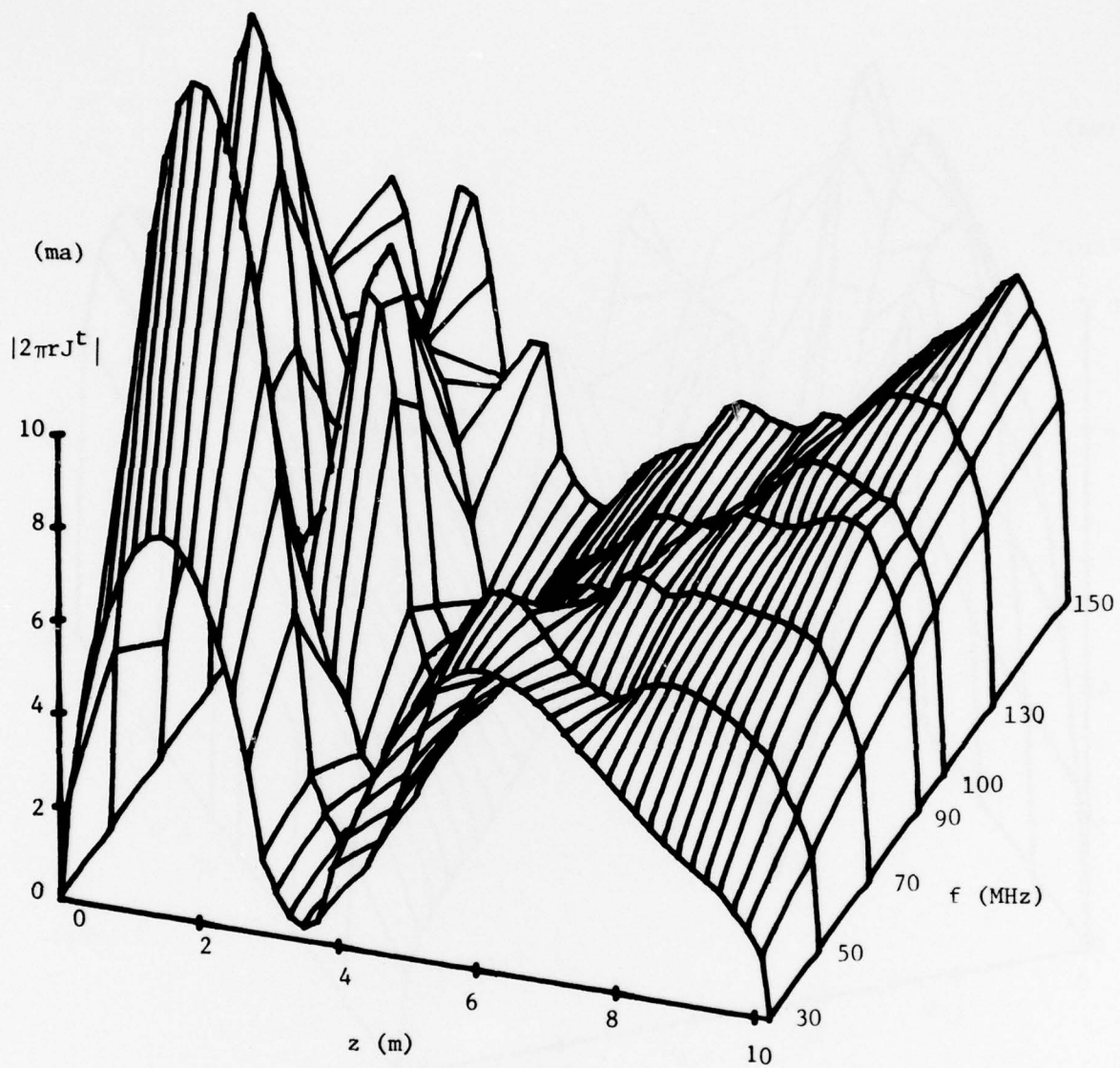


Figure 72. Current on a Chaparral missile as a function of frequency, long plume model, $\theta_i = 60^\circ$.

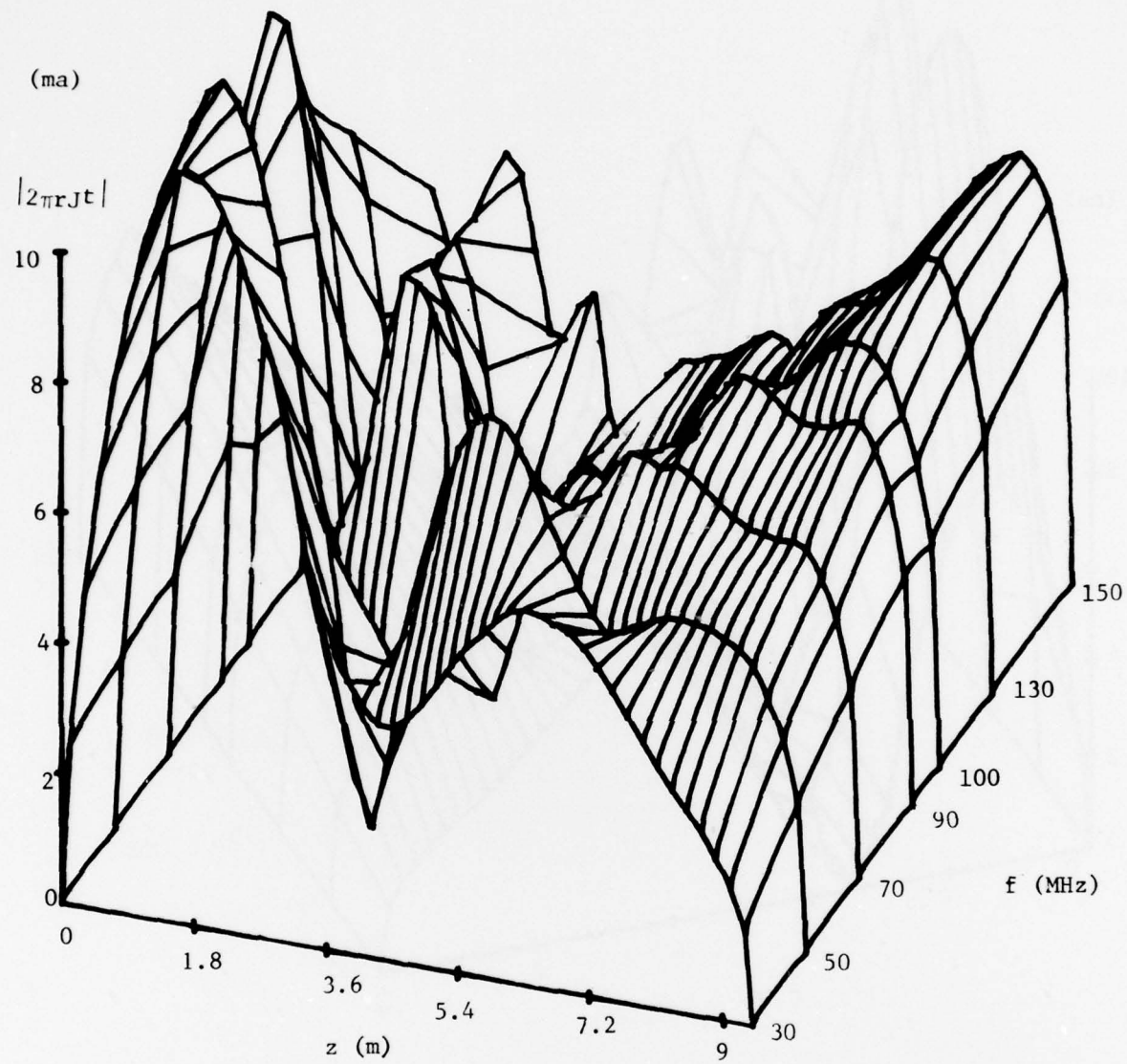


Figure 73 . Current on a Chaparral missile as a function of frequency,
short plume model, $\theta_i = 60^\circ$.

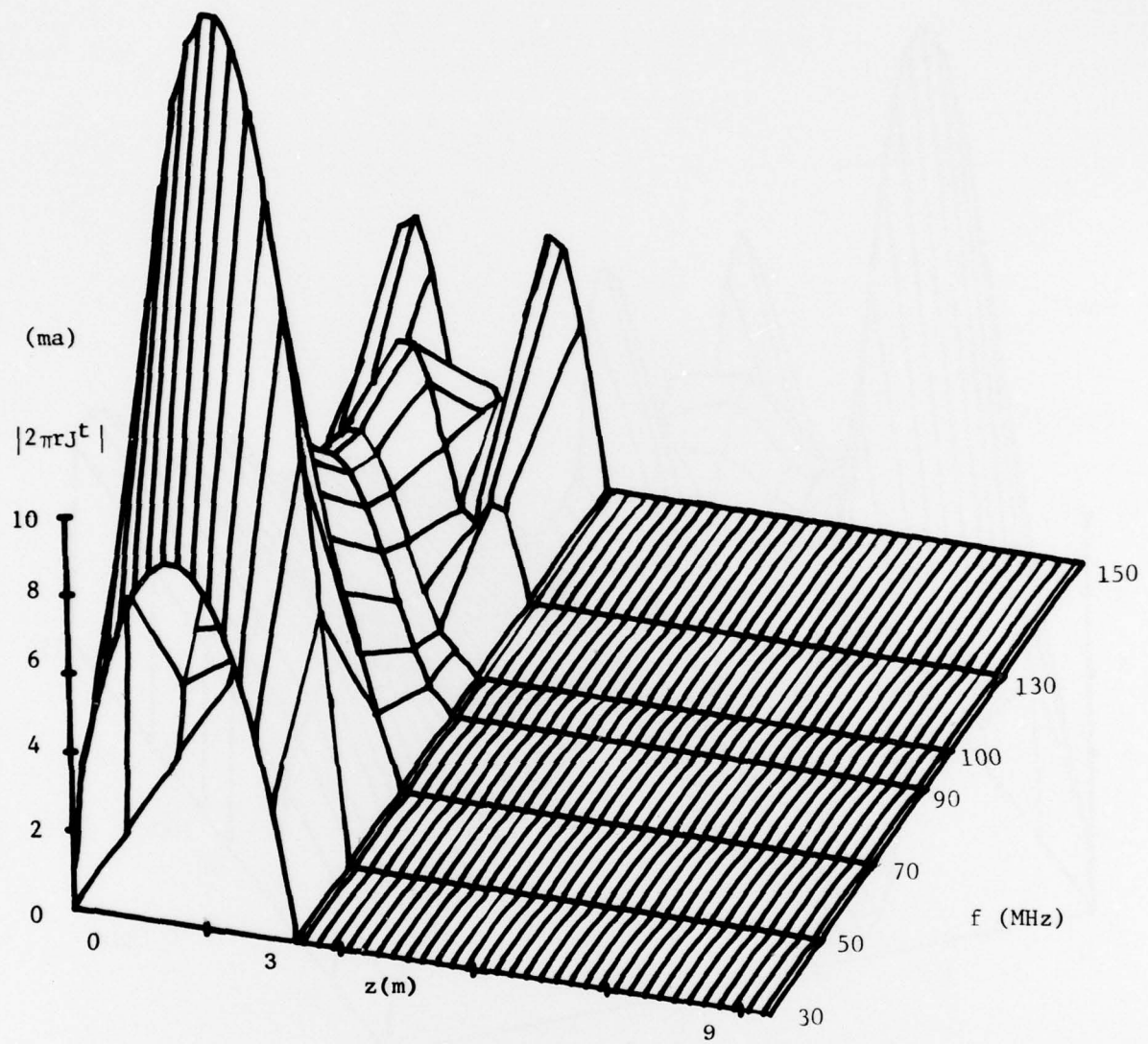


Figure 74. Current on a Chaparral missile as a function of frequency,
no plume, $\theta_i = 90^\circ$.

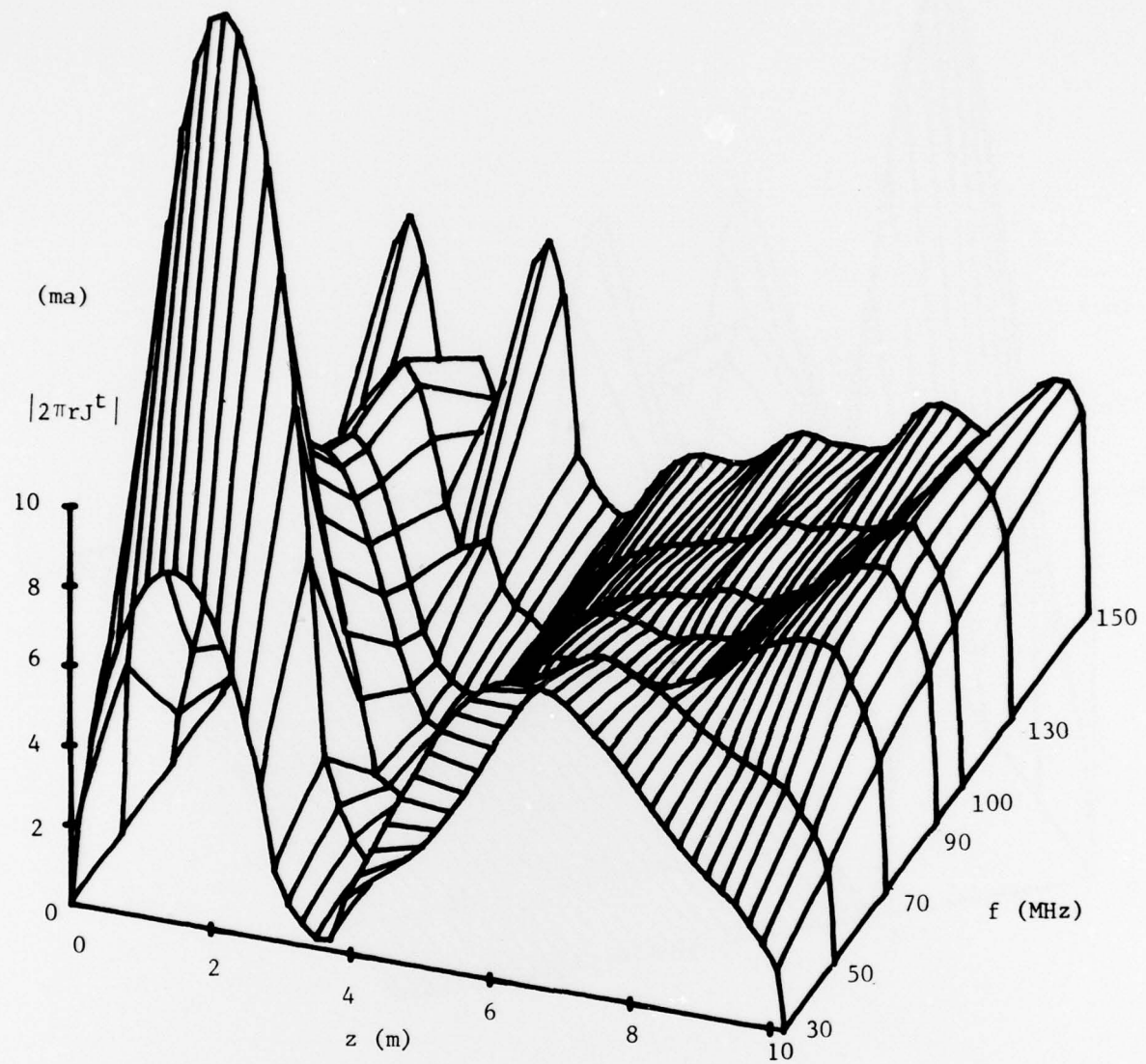


Figure 75. Current on a Chaparral missile as a function of frequency, long plume model, $\theta_i = 90^\circ$.

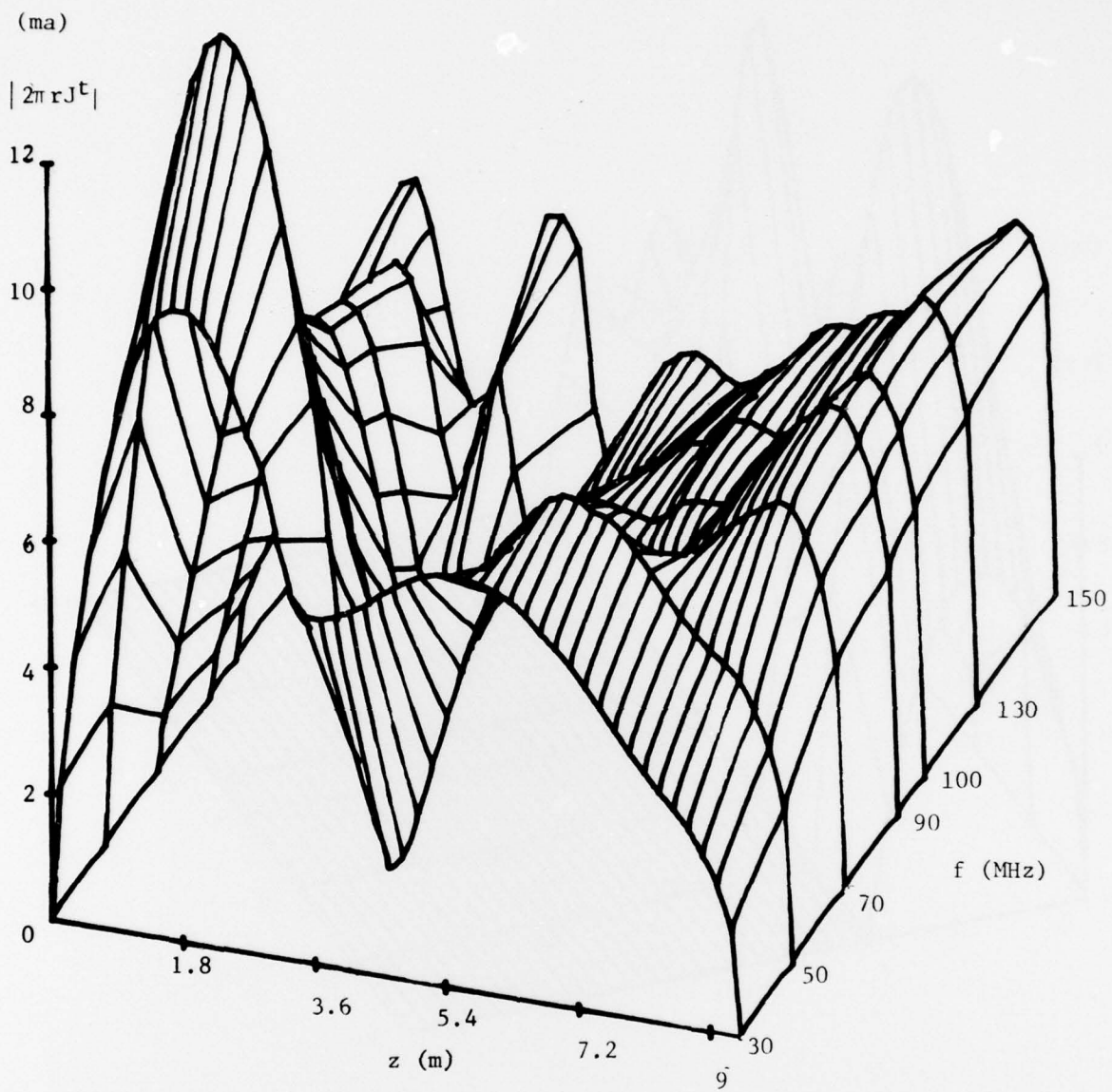


Figure 76. Current on a Chaparral missile as a function of frequency, short plume model, $\theta_i = 90^\circ$.

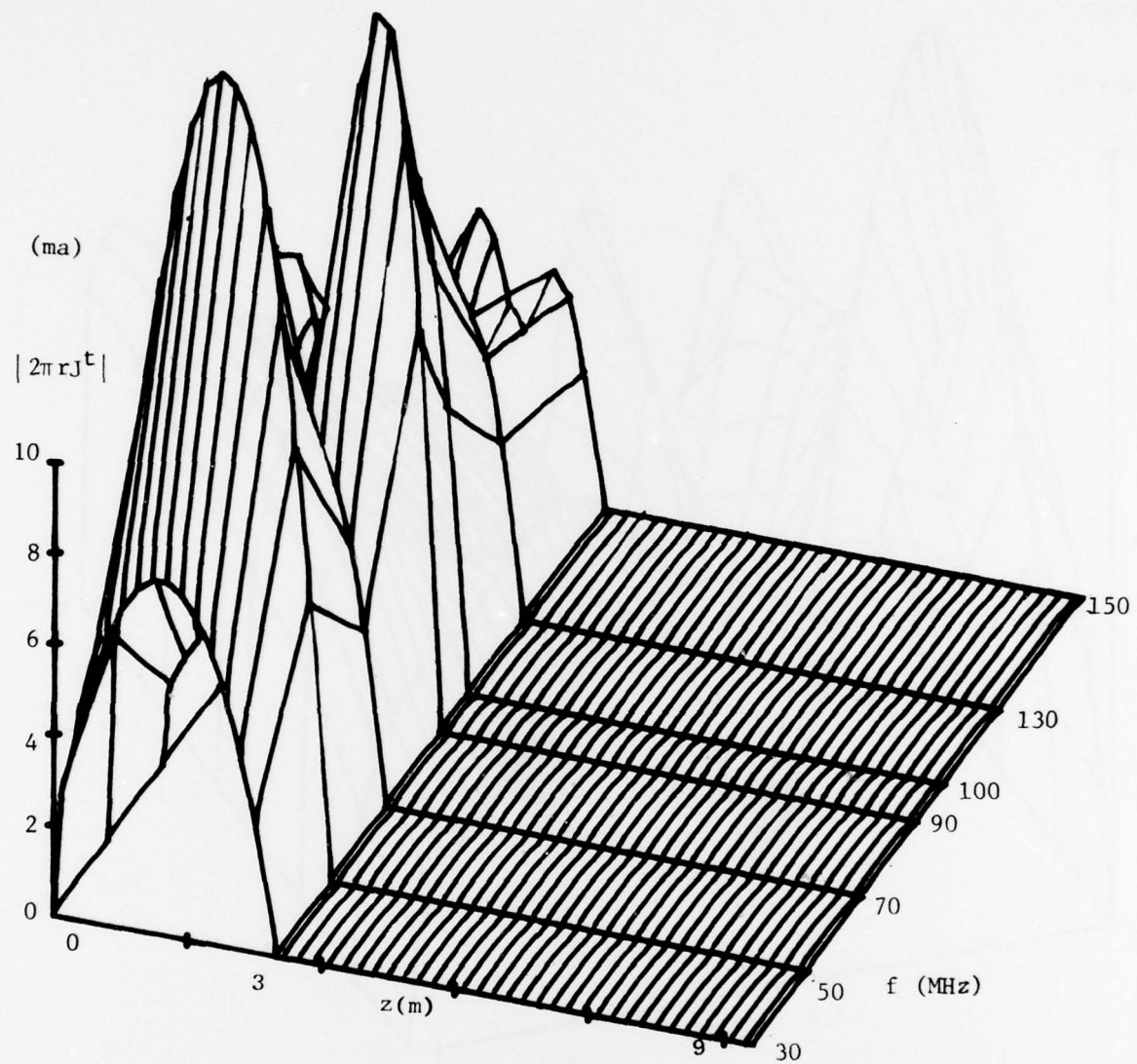


Figure 77 . Current on a Chaparral missile as a function of frequency,
no plume, $\theta_i = 120^\circ$.

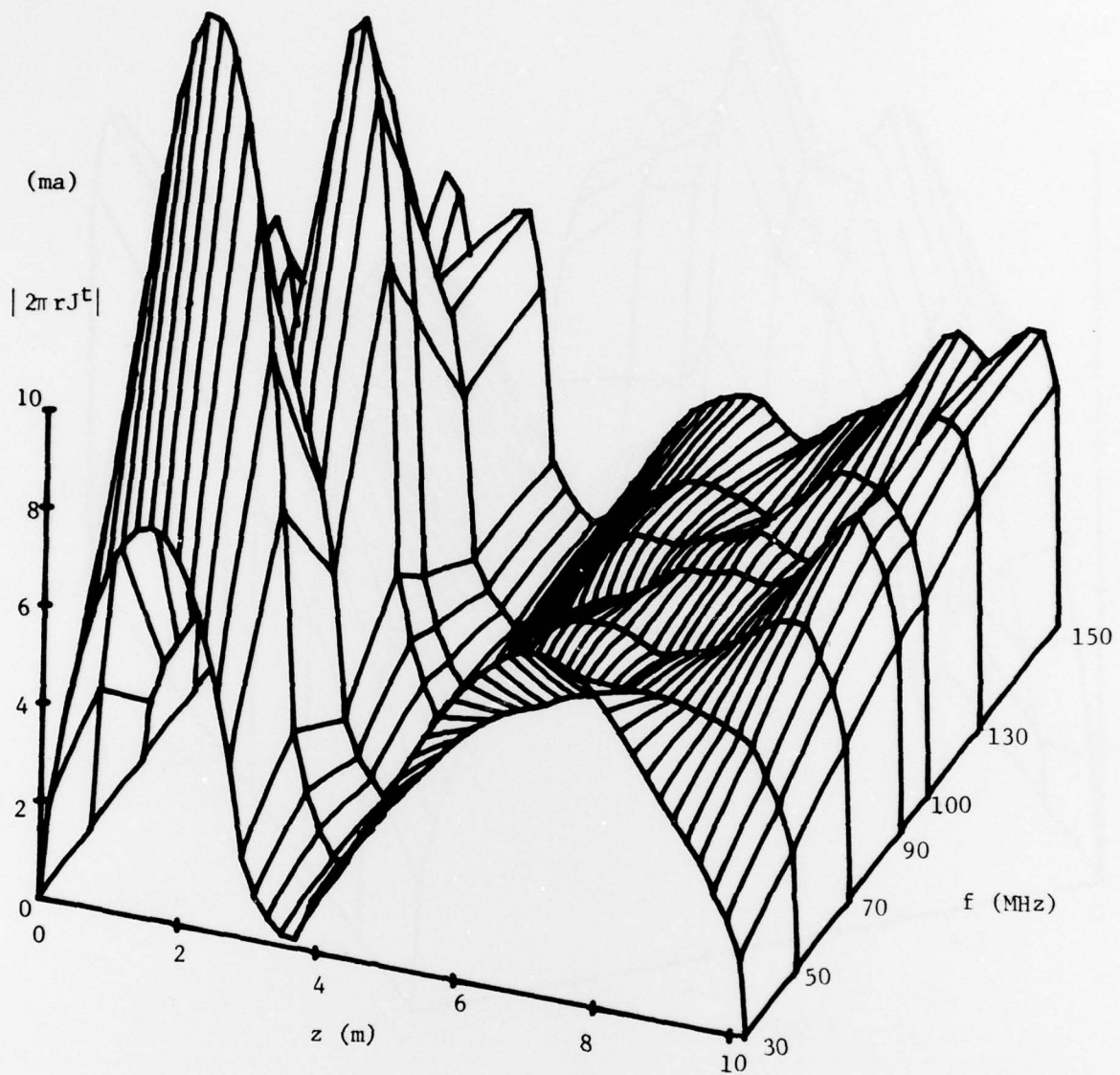


Figure 78. Current on a Chaparral missile as a function of frequency, long plume model, $\theta_i = 120^\circ$.

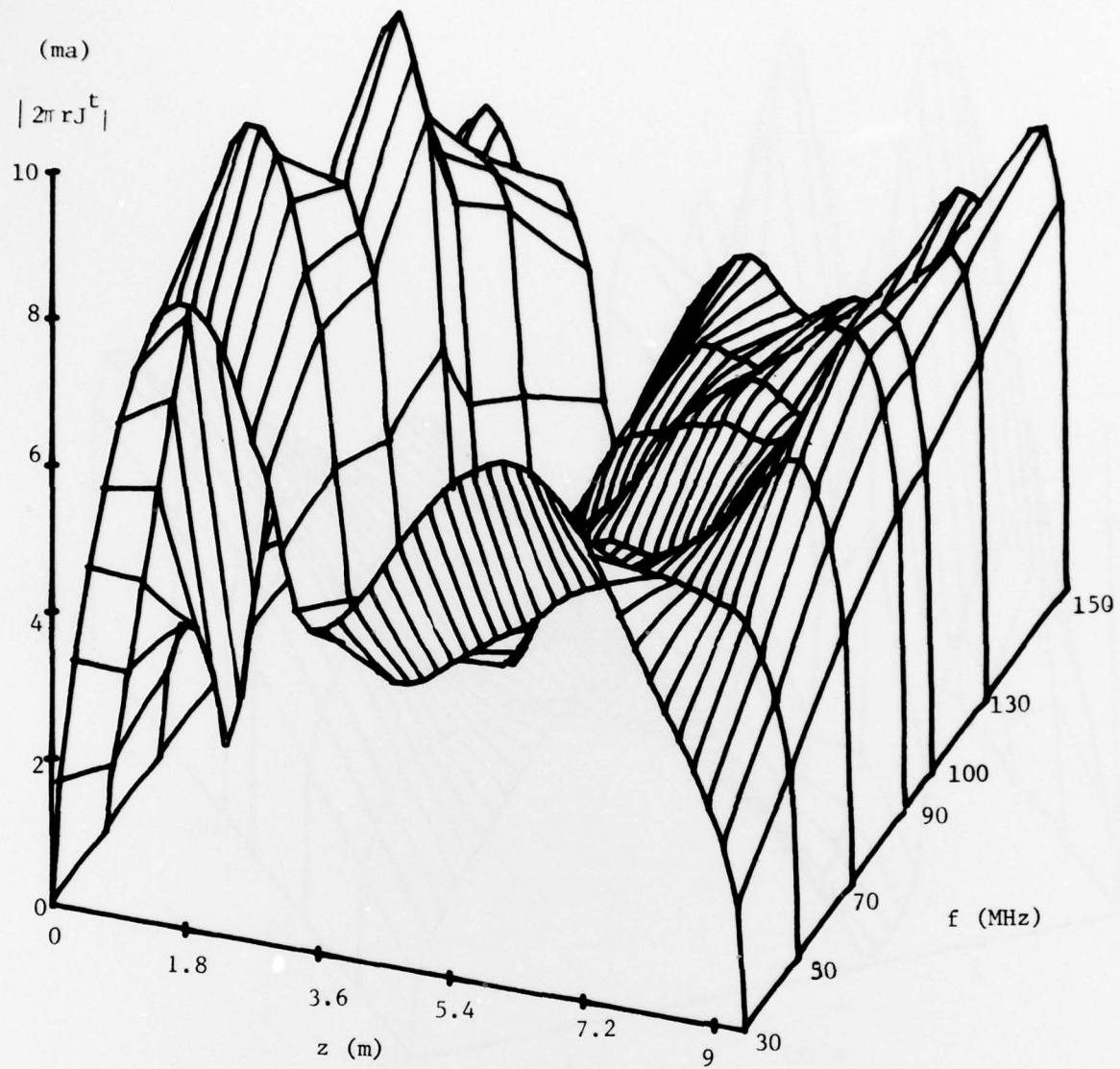


Figure 79. Current on a Chaparral missile as a function of frequency, short plume model, $\theta_i = 120^\circ$.

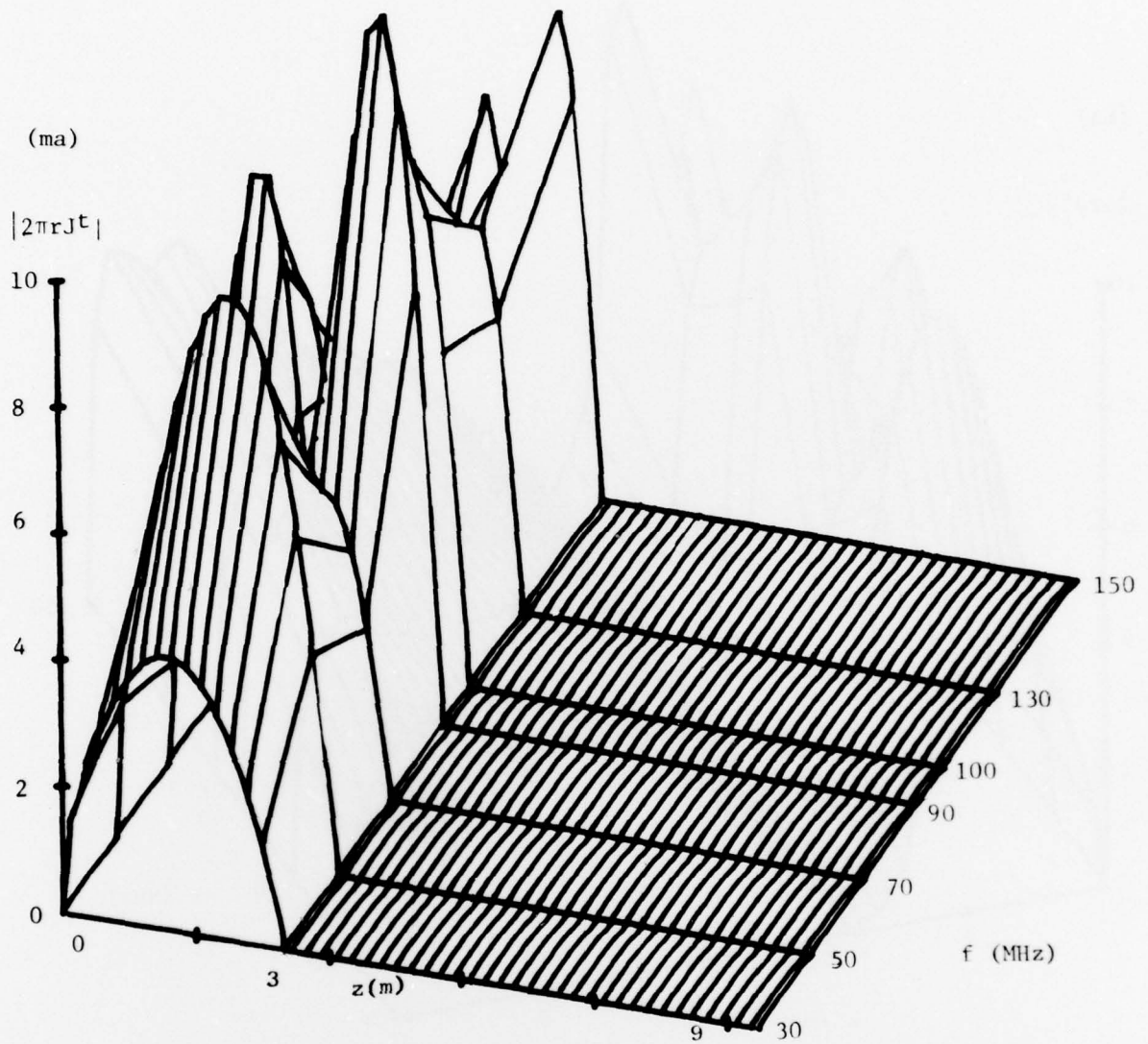


Figure 80 . Current on a Chaparral missile as a function of frequency,
no plume, $\theta_i = 150^\circ$.

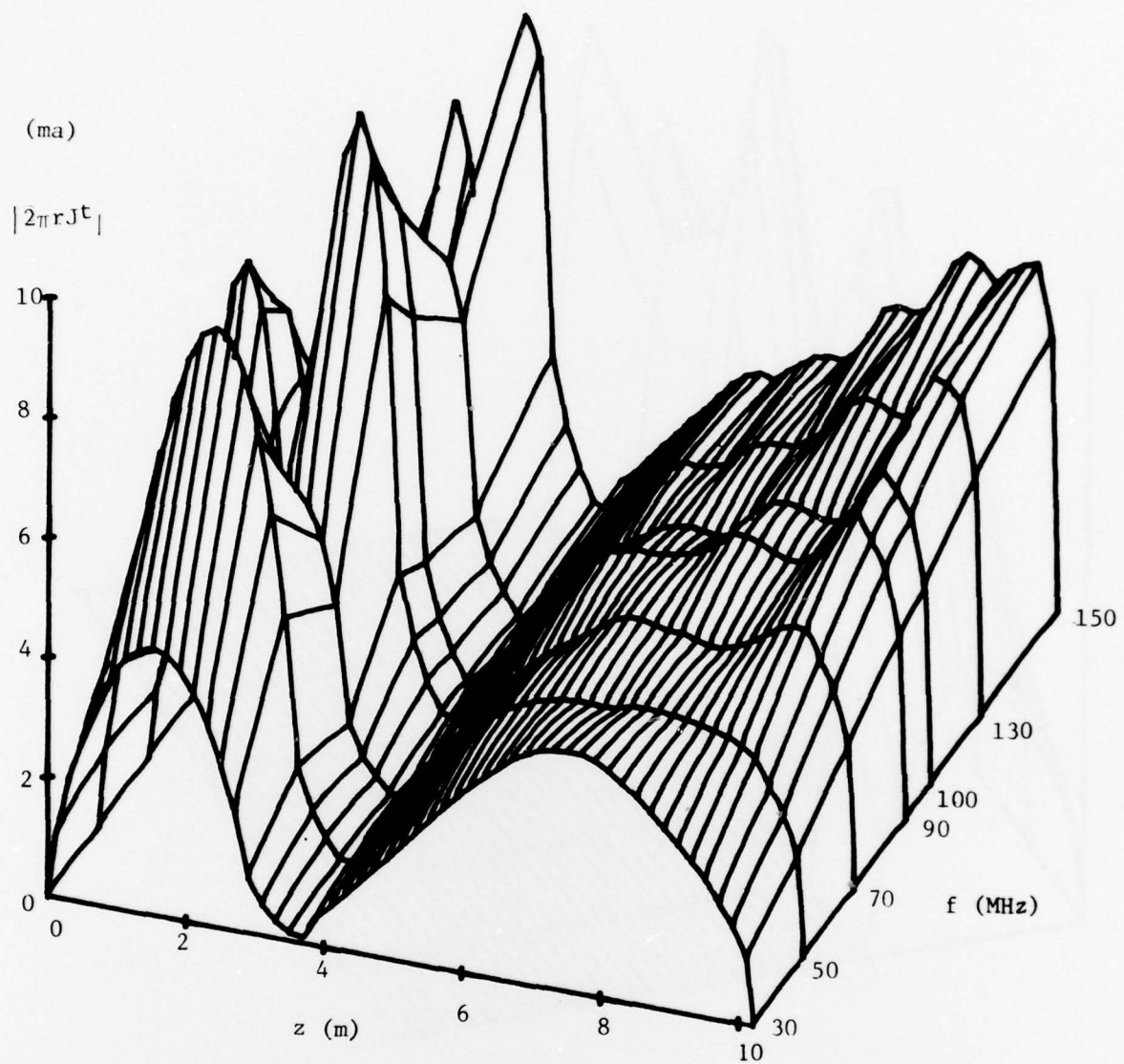


Figure 81. Current on a Chaparral missile as a function of frequency, long plume model, $\theta_i = 150^\circ$.

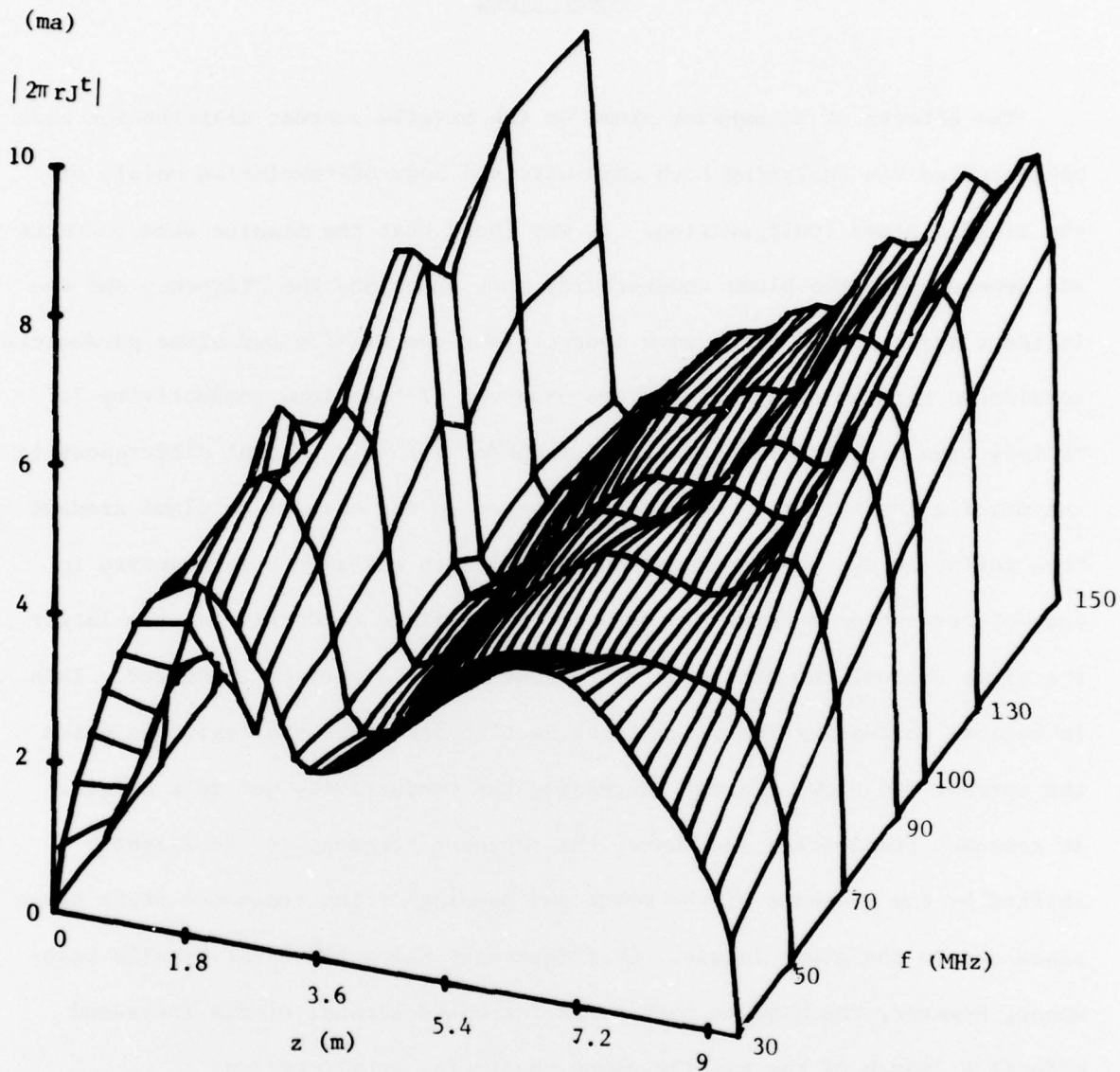


Figure 82 . Current on a Chaparral missile as a function of frequency, short plume model, $\theta_i = 150^\circ$.

CHAPTER IV

CONCLUSIONS

The effects of an exhaust plume on the missile current distribution have been studied via analyzing both thin-wire and body-of-revolution models of the missile-plume configuration. It was found that the missile skin currents are dependent on the plume conductivity and shape and the frequency and the incident angle of the plane wave source. For the missile and plume parameters considered here, minimal effects are observed if the plume conductivity ' σ ' is less than 0.01 mhos/m, but if $\sigma > 1$ mho/m, then significant differences in the missile current are produced as compared to the case of no plume present. Some influence due to the plume shape and length has also been observed in body-of-revolution models. In general, for a fixed conductivity, the larger the plume radius, the more nearly it behaves like a perfect conductor. This is because increasing the plume cross section increases the region in which the current can flow, thereby increasing the conductivity per unit length. At resonant frequencies and above, the resonant frequencies are slightly shifted by the presence of the plume and damping of the resonance peaks takes place due to the plume losses. At frequencies below the first missile resonance, however, the missile current is increased because of the increased effective length of the missile/plume scattering configuration.

Two realistic exhaust plumes, with conductivity varying both axially and radially in the plume region, are used to analyze the Redeye and Chaparral missile plumes using the body-of-revolution model and the Approximate Integral Equation (AIE) method. The major limitation of that analysis is that the plume conductivity should be high enough so the impedance condition (14)

is applicable to the plume surface. An accurate solution not relying on the impedance condition approximation is currently under investigation.

ACKNOWLEDGMENT

Early in the course of this study, Dr. Leonard L. Tsai, who had directed the initial technical activity reported here, died after several months of illness. Dr. Tsai's influence was very great in establishing the initial direction of this study and, indeed, his proposed plan of study, resulting in this report, has been essentially followed in detail. Following his tragic loss, a number of individuals contributed technical and administrative support to ensure the continuity of the work he had begun.. These include G. Brown of Resource Engineering and Planning, Huntsville, Ala., J. Edwards of Rome Air Development Center, Griffiss AFB, N.Y., J. Nordgard of the Georgia Institute of Technology, Atlanta, Georgia, and H. Schuman and V. Eveleigh of Syracuse University, Syracuse, N.Y.

The authors also acknowledge the support of B. Walker and B. Jenkins of the Missile Research and Development Command, Redstone Arsenal, Ala., in providing plume conductivity data for the Chaparral missile.

REFERENCES

1. C. D. Taylor, Electromagnetic Scattering by Thin Inhomogeneous Circular Cylinders, "AFWL EMP Interaction Notes, No. 17, June, 1971; also published in Radio Science, Vol. 2, No. 7, pp. 729-738, July, 1967.
2. C. W. Harrison, Jr., and E. A. Aronson, "On the Response of a Missile With Exhaust Trail of Tapered Conductivity to a Plane Wave Electromagnetic Field," IEEE Trans. on EMC, Vol. 11, pp. 40-49, May, 1969.
3. L. L. Tsai, T. K. Wu, R. D. Darone and G. Brown, "Some Aspects of Valid EMC Testing of Missiles," 1977 EMC Symp. & Exhibition, June, 1977 Montreux; also published in IEEE Trans. on EMC, Vol. 20, No. 2, pp. 306-313, May, 1978.
4. G. S. Smith, J. D. Norgard, and J. Edwards, "Alteration of the Surface Current on a Missile by the Presence of an Exhaust Plume," IEEE Trans. on EMC, Vol. 19, No. 4, pp. 383-394, Nov., 1977.
5. R. R. Mikatarian, C. J. Kan, and H. S. Pergament, "A Fast Computer Program for Non-equilibrium Rocket Plume Predictions," Air Force Rocket Propulsion Lab., Edwards AFB, Tech, Rep. AFRPL-TR-72-94, Aug. 1972, AD-751-984.
6. C. M. Butler and D. R. Wilton, "Analysis of Various Numerical Techniques Applied to Thin-Wire Scatterers," IEEE Trans. on AP, Vol. 23, No. 4, pp. 534-539., July, 1978.
7. C. M. Butler, K. R. Umashankar and D. R. Wilton, "Analysis of the Air Force Weapons Laboratory's Horizontally Polarized Dipole Electromagnetic Pulse Simulator," Electrical Engr. Report, Univ. of Mississippi, Grant AFOSR 75-2825, Aug. 1976.
8. C. M. Butler, K. R. Umashankar and C. E. Smith, "Theoretical Analysis of the Wire Biconical Antenna," Electrical Engr. Report, Univ. of Miss.; Contract No. DAEAl8-74-C-0173; Jan. 1975.
9. T. K. Wu, L. L. Tsai and D. R. Wilton, "Scattering By Composite Metal-Dielectric Bodies of Revolution," paper presented at the Meeting of 1977 USNC/URSI, Stanford Univ., June, 1977.
10. T. K. Wu and L. L. Tsai, "Scattering from Arbitrarily-Shaped Lossy Dielectric Bodies of Revolution," Radio Science, Vol. 12, No. 5, pp. 709-718, Oct. 1977, see also Wu's Dissertation, Electromagnetic Scattering from Arbitrarily-Shaped Bodies, Univ. of Miss., May, 1976.
11. A. J. Poggio and E. K. Miller, "Integral Equation Solution of Three-Dimensional Scattering Problems," Computer Tech. for Electromagnetics, R. Mittra, Ed., Pergamon Press, Oxford, pp. 159-261, 1973.

12. J. R. Mautz and R. F. Harrington, "Radiation and Scattering from Bodies of Revolution," Appl. Sci. Res., Vol. 20, pp. 405-535, June, 1969.
13. R. J. Pogorzelski, "Scattering from Inhomogeneous and/or Composite Bodies of Arbitrary Shape," Paper presented at the 1976 AP-S International Symposium, Amherst, Mass.
14. R. J. Pogorzelski and T. K. Wu, "Computations of Scattering from Inhomogeneous Penetrable Elliptic Cylinders by means of Invariant Imbedding," paper presented at the 1977 International URSI Symposium on Electromagnetic Wave Theory, Stanford Univ.
15. H. E. Bussey and J. H. Richmond, "Scattering by a Lossy Dielectric Circular Cylindrical Multilayer, Numerical Values," IEEE Trans. on AP, Vol. 23, No. 5, pp. 723-725, Sept. 1975.
16. M. A. Leontovich, Diffraction, Refraction, and Reflection of Radio Waves, edited by V. A. Fock, N. Logan, and P. Blacksmith, Appendix.
17. T. B. A. Senior, "Impedance Boundary Conditions for Imperfectly Conducting Surfaces," Appl. Sci. Res., B-8, pp. 418-438, 1960.
18. T. K. Wu and C. M. Butler, "Numerical Green's Function for Dielectric Bodies of Revolution and Its Applications," National Radio Science Meeting, Jan. 1978, Univ. of Colorado, Boulder.
19. K. M. Chen, D. E. Livesay and B. S. Guru, "Induced Current in and Scattered Field from a Finite Cylinder with Arbitrary Conductivity and Permittivity," IEEE Trans. on AP, Vol. 24, No. 3, pp. 330-336, May, 1976.